58 B

University of Cape Town

Physics Department

POLARIZATION IN NEUTRON-PROTON ELASTIC SCATTERING AT 21.6 MEV

B.R.S. SIMPSON

A thesis submitted to the

University of Cape Town

for the degree of

Doctor of Philosophy

October 1986

ABSTRACT

The polarization in n-p scattering has been measured at 21.6 MeV using polarized neutrons from the $T(d,\vec{n})^4He$ reaction. The measuring instrument was an anthracene scintillation polarimeter. A critical assessment of this polarimeter was made, and extensive refinements to the polarimeter were introduced so as to minimise perceived sources of systematic error. These included improvements both in instrumental design and data reduction techniques.

The present n-p polarization results are compared with earlier measurements made at similar energies. The Δ^P_{LS} and Δ^D_{LS} phase parameters derived from the data are: $0.880^\circ \pm 0.023^\circ$ and $0.12^\circ \pm 0.01^\circ$ respectively. The data are compared with the phase shift analyses of Arndt et al and of Bohannon et al . A comparison is also made with the n-p polarization predictions at 21.6 MeV given by the Paris potential, which are found to be in good agreement with the data.

The use of the polarimeter as an analyzer was investigated by measuring the polarization of neutrons from the $T(d,\vec{n})^4He$ reaction at reaction angle 25° and E_d=5.6 MeV. The value obtained, P=0.110 ± 0.015, indicates a depolarization resonance, confirming the suggestion of Mutchler et al. that the ^5He resonance at 20 MeV may introduce a strong perturbation in the $T(d,\vec{n})$ polarization at E_d=5.6 MeV.

ACKNOWLEDGEMENTS

The author wishes to express his appreciation to

His supervisor, Prof. F.D. Brooks, for his guidance and assistance throughout the project;

Dr. C.M. Bartle for acting as supervisor during 1978;

Dr. W.R. McMurray and the staff of the Van de Graaff accelerator of the National Accelerator Centre for their co-operation;

Dr. H.G. Miller of NRIMS,CSIR for theoretical calculations;

Dr. J. Whittaker, Dr. D.T.L. Jones, F.D.Smit, D.M. Whittal and M.S. Allie for their assistance during the running of the experiments;

Mr. P.A. Back, Mr. L. Fowle, Mr. L. van Heerden and the rest of the physics workshop staff for constructing the necessary apparatus;

Mr. P. Groenewald for drawing the diagrams;

Mrs. C. Barends for entering a large portion of the text via the word processor;

His parents and sister for support and encouragement;

The South African Council for Scientific and Industrial Research for financial assistance;

The University of Cape Town for the award of a Joseph Stone Bursary.

CONTENTS

LIST OF TABLES

LIST OF FIGURES

6.5 Analyzing power for n-He elastic scattering at angles usually used in a helium neutron polarimeter.

6.6 Neutron polarization values for the $T(d,\vec{n})^4He$ reaction at reaction angles $\xi=90^o$ and $\xi=120^o$.

CHAPTER 1

INTRODUCTION

1.1 N-N force

The two-nucleon system is the oldest and most thoroughly investigated strongly interacting system. The study of this system is directed largely at understanding the N-N force in the sense that this is treated as a basic force; it is basic to the nucleus.

The aim of these studies is the understanding of the laws governing the forces between nucleons as completely as possible, and to achieve this it is necessary to measure the N-N interaction in detail for comparison with theory. The interaction serves as a basis for a fundamental understanding of nuclear structure and hence is the key to a vast area of physics. The N-N system can also be used as a proving ground for general theories of elementary particles (e.g. tests of group theoretical schemes; tests of general conservation laws).

The conventional way of studying the nuclear force is via scattering amplitudes, phase shifts, and phenomenological forces. These should, in principle, be derivable from the more recent theories, such as the quark-gluon-bag picture, through quantum chromodynamics .

A review of the conventional attempts at understanding the nucleon-nucleon interaction is given in the following sections. This is followed by a very brief summary of quantum chromodynamics and its use in aiding the study of the nuclear force. Thereafter the experimental aspects contributing towards an understanding of

the nuclear force are described with particular reference to the role of phase shift parameters, and the importance of spin dependent experiments such as polarization measurements.

1.2 Nucleon-nucleon potentials

In general the potential V between the two nucleons, denoted 1 and 2, has the functional dependence $V(r,\sigma_1,\sigma_2,L)$, where r is the interparticle distance, σ_1 and σ_2 are the Pauli spin operators, and L is the orbital angular momentum operator. The dependence of V on σ_1, σ_2 and L exhibits the maximum complexity allowed within the restriction implied by rotational, reflection and time-reversal invariance. The interaction differs in each spin-parity state, and exhibits significant non-locality or velocity dependence as well as a tensor component and spin-orbit coupling. Certain features of the NN interaction are qualitatively understood, notably the existence of

i) long-range attraction;

ii) short-range repulsion;

iii) a tensor force of moderate range; and

iv) a spin-orbit force of shorter range.

A quantitative understanding of the N-N interaction is more complex. As a result of this complexity, one approach to the N-N interaction has been to take advantage of the progress in experimental work, and to abandon the difficult task of searching for a satisfactory theoretical model. Instead, more or less arbitrary empirical parametrisations of phase shifts (Livermore group(MA69), Yale group(SE68), Arndt et al. (AR83)) or potentials (Yale(YA62), Hamada and Johnston(HA62), Reid(RE68), Sprung and de Tourreil)(SP73)) have been proposed to fit the two nucleon data.

Recent potential models such as the Paris potential (LA75) are more theoretically based with far fewer adjustable parameters. Once the free parameters are determined by such fits, these potentials are, in turn, used in nuclear structure calculations, sometimes with success.

Efforts to compute the potential from a combination of field theory and dispersion theoretic techniques are based on the following assumption (NO77) - that the problem is to calculate that function which, when used in some non-relativistic Schroedinger-like equation, will reproduce the two-nucleon on-shell scattering observables. Although there is no theoretical guarantee that the potential so defined is appropriate to use for systems with more than two nucleons, this method of attack is showing promise. A brief summary of this approach follows.

From a purely theoretical point of view, the most significant advance was the meson theory of nuclear forces proposed by Yukawa (YA35) in 1935. The main result of this theory, namely the one-pion-exchange (OPE) contribution to the NN interaction, survives intact today. However, when one performs a detailed analysis of the wealth of nucleon-nucleon data, it is soon apparent that the OPE contribution gives a good description of the interaction only at very large distances ($r > 2$ fm) and it has to be supplemented by further contributions. Three approaches have been developed, namely:

i) <u>The field theory viewpoint</u>

Specific fundamental Lagrangian models are adopted, and the OPE contribution can be regarded, in a perturbation theory, as a 2nd order process of a fundamental pion nucleon coupling. In

this scheme, it is natural to consider also the next-order processes, in particular the 4th order terms i.e. the exchange of uncorrelated pions (see figs. 1.1 and 1.2). A weakness of this approach is that the validity of using perturbation theory in strong interaction processes is questionable. Also, the meson-meson interaction exists independently of perturbation theory and should be accounted for properly in any realistic theoretical model.

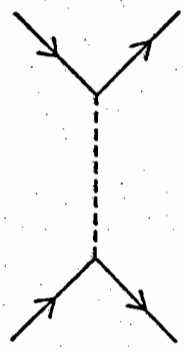

Fig. 1.1 The one-pion-exchange contribution to the nucleon-nucleon interaction.

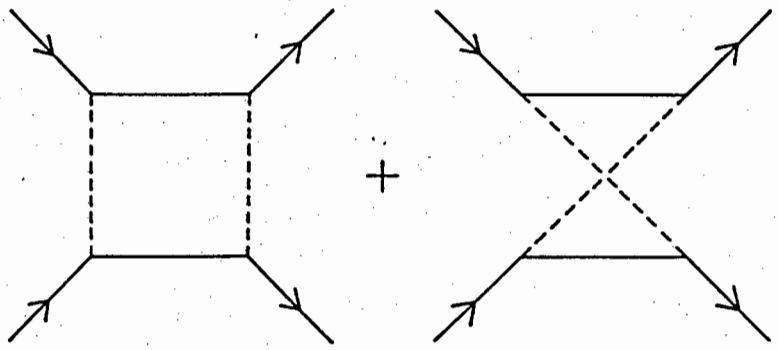

Fig. 1.2 The "4th-order contribution" to the nucleon-nucleon interaction.

ii) One boson exchange models

With the discovery of the ρ and ω resonances, the OPE was generalized to models (OBE) which consider the exchange of non-strange mesonic resonances as being responsible for the medium and short range forces. These models are very appealing because of their simplicity, but they also suffer from imperfections. To fit the data in these models one always needs the exchange of a fictitious scalar particle, with a low mass of 400-500 MeV, to

provide some intermediate range attractive forces that are not accounted for by the exchange of observed resonances. The existence of such a particle is not supported by any experimental evidence. These models also suffer from the defect of treating the massive composite systems which decay very rapidly, as stable particles (zero width approximation).

iii) The hybrid approach

In more recent years (1973 onwards) a meson theory of nuclear forces has been developed that combines the best features of the field theoretical and the OBE calculations. This approach of Lacombe et al (LA75) has produced a semiphenomenological model referred to as the Paris potential. This potential is now perhaps the most extensively used nucleon-nucleon potential available today.

1.3 The Paris N-N potential (This summary is based on an article by R. Vinh Mau (VI77) and subsequent relevant publications)

The approach is based on two prerequisite demands:

i) Only nucleons and pions can be treated as particles and the rapidly decaying nucleonic and mesonic resonances must be regarded as composite systems. This requires that nucleon-nucleon forces should be studied in conjunction with the known properties of mesons, their interactions with themselves and with nucleons; and

ii) Perturbation theory must be avoided.

A nucleon-nucleon interaction has been derived from πN and $\pi\pi$ interactions, which includes the OPE, correlated and uncorrelated two-pion-exchange ($2\pi E$), and ω-exchange contributions.The

interaction, in configuration space, is written as a series of terms:

$$V \simeq \frac{g^2 e^{-\mu r}}{r} + \int_{4\mu^2}^{\infty} \rho_{2\pi}(w,t') \frac{e^{-\sqrt{t'}r}}{r} dt' + \int_{9\mu^2}^{\infty} \rho_{3\pi}(w,t') \frac{e^{-\sqrt{t'}r}}{r} dt' + \text{etc...}$$

where μ = the pion mass;
g = pion nucleon coupling constant; and
w and t are related to the nucleon four-momenta.

The successive terms correspond to the OPE contribution, the $2\pi E$ contribution, etc. The whole dynamics of the problem is contained in the spectral function $\rho_{2\pi}$, $\rho_{3\pi}$, etc.

The OPE contribution gives a good account of the peripheral nucleon-nucleon phase shifts and, therefore, of the long range part of the interaction. The underlying belief is that most of the medium range forces are correctly given by the $2\pi E$ when the latter is properly determined.

Ericson and Miller (ER83) have resolved the long-standing discrepancy of the charge-dependent NN scattering lengths ,i.e. the problem of understanding the difference between p-p (or n-n) and n-p singlet scattering at threshold, as a natural, though non-trivial, consequence of OPE, $2\pi E$ and ($\gamma\pi$) exchange. No anomalous interactions need be invoked. Their result should therefore be viewed as non-trivial quantitative evidence for the importance of $2\pi E$ at intermediate range.

With a view to achieving an accurate calculation of the $2\pi E$ contribution, the required two-pion spectral function is related, via a set of equations, to the pion-nucleon and pion-pion interactions. The pion-nucleon scattering is very accurately known by various phase shift analyses, and the S and P wave pion-pion interaction has also been extensively studied. By using the

former analysis as input, all the nucleonic resonances are automatically included since they are contained in πN phase shifts. The ω meson is a narrow 3π resonance, and its exchange is considered, to a good approximation, as a single particle exchange. The dominant forces provided by the ω meson exchange contribution are repulsive.

These theoretical descriptions give a good account of the long and medium range (LR+MR) N-N forces as demonstrated for example by the facts that: i) the low energy (up to 330 MeV) peripheral (J > 2) NN phase shifts calculated (VI72) from the theory are in good agreement with the experimentally-determined phase shifts; and ii) an equivalent potential derived from this (π+2π+ω) exchange interaction compares very well with successful phenomenological potentials such as Yale and Hamada-Johnston down to internucleon distances r ≃ 0.8 fm. (CO73). More recently (LA80) another part of the 3π exchange represented by the term A_1 has also been included, giving four adjustable parameters in all. To summarise then, the long and medium range parts of the interaction are taken from π,2π,ω and A_1 exchange. Coupling constants of the ω and A_1 are fitted, and the 2π exchange is calculated as explained above.

The description of the short range (SR) part of the interaction is related to exchange of the three pion and higher mass systems, and/or to effects of subhadronic constituents such as quarks, gluons, etc. Since no satisfactory theoretical model for the SR forces has yet been found, the provisional viewpoint has been to adopt a phenomenological description with the accurately determined long and medium range (LR+MR) interaction

providing strong constraints on this SR part. The complete potential is then written as

$$V(r,E) = V_{theor}(r,E)\, f(r) + V_{Phen}(r,E)\, [\, 1-f(r)\,]$$

where E is the c.m. energy and where

$$f(r) = (pr)^{\alpha} / \{\, 1 + (pr)^{\alpha}\, \}$$

is a function designed to cut off V_{theor} rather sharply at $r \approx$ 0.8 fm. Both V_{theor} and V_{Phen} contain central(C),spin orbit(SO), spin-spin(SS), tensor(T) and quadratic spin orbit(SO2) components. It was found that the central component of the theoretical potential has a weak but significant energy dependence and that this energy dependence is , in a very good approximation, linear. Hence

$$V_{theor}(r,E) = U_{theor}(r) + E\, W_{theor}(r)$$

where $W_{theor}(r)$ is zero for the SS,T,SO and SO2 components. The short range part is also assumed to be energy dependent, and for simplicity $V_{Phen}(r,E)$ is taken as constant with respect to r and therefore is only a function of the energy. The composite nature of the nucleon suggests that the short-range forces are not infinitely repulsive, and hence the condition is imposed that V_{Phen} be finite at r = 0 (soft core).

A first fit of the Livermore energy-independent phase-shift analysis[MAW] (MA69) revealed that $V_{Phen}(E)$ is a linear function of E for the C component and almost constant for the other components. Therefore $V_{Phen}(E)$ is taken to be of the form C + C'E for the central component and constant for the other terms, so that the complete potential V(r,E) is written as

$$V(r,E) = U(r) + E\, W(r)$$

with

$$U(r) = U_{theor}(r)f(r) + C[1 - f(r)] \quad \text{and}$$

$$W(r) = W_{theor}(r)f(r) + C'[1 - f(r)] ,$$

C′ being zero for the SS,T,SO and SO2 components. V(r,E) now contains six free parameters for each isospin state, T = 0 or T = 1, namely C_C, C_{SS}, C_T, C_{SO}, C_{SO2} and C'_C.

The determination of these core parameters was found (LA80) via a two step procedure, first the best fit of the MAW phase shifts was searched for and then the results were tuned up by fitting the data themselves. The data used consisted of 913 p-p scattering data points between 3 and 330 MeV and 2239 n-p scattering data points between 13 and 350 MeV. The χ^2 per degrees of freedom are as good as, if not better than, the ones given by the best phenomenological potentials which contain many more free parameters.

This model in which a definite separation between the theoretical and phenomenological parts is made, was designed for providing a clear physical insight into the problem. It has also been parameterized (LA80) in a simple analytical form for practical use in various many-body calculations.

1.4 QCD and phenomenological models (based on IS83 and BR83)

Over the last decade, the proposal (GE64 and ZW64) that the proton, neutron, pion and all other strongly interacting particles - the hadrons - consist of quarks, has become firmly established. Quantum chromodynamics [QCD] (FR73 and NA66) is a generalization of quantum electrodynamics - the theory of photons and electrons that underlies atomic physics. Instead of the electron, QCD has

the quark; instead of the photon it has the gluon. The "generalization" that extends QED to QCD is that while electrons come in only one (electric) charge "state", quarks come in three ("colour") charge states. Another crucial extension is that whereas the photon is uncharged, the gluon itself must carry colour charge so that colour can be conserved in gluon emission or absorption transitions. QCD is still in its infancy, with rather few rigorous results having been derived from it so far.

At distances between 10^{-16} and 10^{-15} metres, the interquark force begins to deviate from Coulombic(1/r) behaviour and becomes a linear potential, corresponding to a constant force. This transition leads to the confinement of quarks and explains why free quarks are not seen in nature. In the confinement region the coupling between quarks and gluons becomes very strong, and little is understood because perturbative methods fail. However, progress is being made along many lines of attack. These include a technique pioneered in the Soviet Union (ZA80), numerical work on field theories known as "lattice gauge theory" (WI74) and simplified quantum field theory models that can approximate QCD.

Some models for confinement are not based on the concept of a potential. Foremost among these is the "bag model" (JO75) based on field theory in a cavity that confines quark and gluon fields.

A recent extension to the bag model, called the chiral bag model (BR79,MI81,BR86) , proposes that the nucleon's central core of quarks is surrounded by a cloud of mesons. The pion cloud exerts a pressure on the internal confinement region, and together they constitute the total physical extent of the nucleon.

This picture, when applied to interactions in nuclei, leads naturally to Yukawa's meson-exchange description [OPE]. The

exchange forces, which are the source of the forces between nucleons, involve the exchange of virtual bosons; namely a π , ρ or ω meson (one boson exchange models).

An important feature of the nucleon-nucleon interaction is the strong repulsion resulting from ω exchanges. In calculations of the bag-model type, the ω-exchange potential will begin to cut off when the bags begin to merge. However, the coupling constant is so large that even a small remaining part of the ω-exchange potential will play a more important role than perturbative gluon exchange in the interior of the bag. It is the great strength of the short-range nuclear interactions that makes them essential in nuclear physics as compared with interactions from gluon exchange.

This repulsion between bags may be the reason why effects from quark substructure may be hard to see in low-energy nuclear physics. It seems, therefore, that the interaction of two nucleons is well described by the boson exchange model, regularized at short distances to take account of the quark core. Along these lines a hybrid quark-baryon model for nuclear forces has recently been proposed (WA84), which simultaneously incorporates the quark- and gluon- exchange mechanism at short distance and the meson-exchange mechanism at long and intermediate distances. This model has been shown to explain the observed NN phase shifts fairly well, almost comparable with the phenomenological treatments of Reid (RE68) and Hamada-Johnston (HA62). Once the highly nonperturbative aspects of QCD are understood, knowledge of the structure of the nucleon will provide constraints on how and what boson exchanges intervene.

1.5 Experimental Work

N-N phase-shift analyses are essential because they provide a way of summarizing experimental results in a more or less model independent form. As such they form a convenient meeting ground for experiments and theory. An outline of the partial wave description and the procedures used for determining the phase shifts is presented in appendix 1.1.

New experiments on the N-N interaction at low energies ($E < 100$ MeV) continue to be of considerable interest. This is because the knowledge of the low-energy phase shifts depends on the correctness of the extrapolation methods used in energy-dependent phase shift analyses in which certain theoretical assumptions are used to anticipate the behaviour at low energies from the analysis of data at higher energies. In general then, amongst other things, experiments on low-energy nucleon-nucleon scattering provide a test of these theoretical assumptions.

1.6 Polarization

The number of phase shifts which are required to accurately describe NN scattering increases rapidly with energy, and a knowledge of only the differential and total scattering cross-sections for unpolarized nucleons is insufficient to determine these phases. Fortunately a great deal of information can be obtained by scattering polarized beams, that is beams in which the spins of the nucleons are not randomly oriented, but have some preferred direction. As a result high precision polarization measurements are desirable because they make an important contribution to the reduction of phase-parameter uncertainties.

For spin-1/2 particles there are two spin states which may be conveniently referred to as "up" and "down". If the number of particles in the beam with spins along and opposite to the preferred direction are N↑ and N↓ , then the polarization of the beam is defined as $P = (N\uparrow - N\downarrow)/(N\uparrow + N\downarrow)$.

At the time of the 1980 polarization conference (Santa Fe) only a few precision experiments on NN scattering at low energy were reported, and it was suggested that measurements of this kind, with polarized beams, should be continued.

The analyzing power in n-p elastic scattering is determined by scattering a polarized neutron beam from a hydrogen target. Then the left-right asymmetry $\varepsilon = (N_L - N_R)/(N_L + N_R)$ where N_L and N_R are the number of neutrons scattered to the left and right of the incident beam direction respectively. The asymmetry is related to the polarization by the formula $\varepsilon = A_y(\theta).P_{inc}$ where P_{inc} is the polarization of the incident neutron beam, and $A_y(\theta)$ is the analyzing power for the scattering angle θ. It can be shown that the analyzing power is equal to the neutron-proton polarization $P_{np}(\theta)$.

Experiments on n-p scattering are inherently less accurate than for p-p scattering although considerable progress has been made in recent years. The n-p scattering occurs in both T=0 and T=1 isospin states. If the charge independence hypothesis holds, the T=1 amplitudes as measured in p-p and n-p scattering should be identical in all but electromagnetic effects. This assumption is needed for the analysis of n-p scattering data. The isospin-one n-p phases for $l \geq 1$ are obtained from p-p experiments, and the

n-p data in effect are used to find primarily the isospin-zero phase shifts which do not enter in the p-p system. The low energy data fixes the following phase parameters (see Appendix 1.1) : $^3S_1$, $^1P_1$, $^3D_{1,2,3}$ and ε_1 which couples the J = 1 states $^3S_1$ and $^3D_1$.

1.7 n-p polarization data at $10 < E_n < 30$ MeV

The more recent n-p polarization data in this energy range are summarised in table 1.1. A brief discussion of this work is now given.

Tornow et al. (TO80) have reported accurate analyzing power measurements for n-p scattering between 13.5 and 16.9 MeV. They showed that their data, especially at 16.9 MeV, differ from results of the YALE-IV (SE68), Livermore-X (MA69) and Arndt et al. (AR77) phase-shift analyses. Subsequently the predictions of the Paris potential on the polarization and on the phase shifts at 16.9 MeV were presented by Cote et al. (CO80). The polarization measurements of Brock et al. (BR78) at 14.2 MeV were also included in the comparison. The agreement between the Paris prediction and the experimental data for P(θ) is excellent at 14.2 MeV, and fairly good at 16.9 MeV (see fig.1.3). More recent, but less precise, measurements at 17 MeV from Karlsruhe (WI84) are in good agreement with the precise data of Tornow et al. Cote et al. suggest that these high-precision n-p data should be used to learn more about the T=0 force, in particular the $^1P_1$, ε_1, and triplet D phases in a locally energy-dependent phase-shift analysis using exact formulae with high partial waves constrained by OPE. Brock et al. (BR81) suggest that the 14 MeV to 17 MeV n-p analyzing power needs to be found, over as wide an angular range as

Table 1.1 Summary of the more recent P_{np} data for $10<E_n<30$ MeV.

Name & reference	Type[a)]	E_n (MeV)	angular range (deg. c.m.)
Tornow et al. (TO80)	E	13.5 - 16.0	90
Tornow et al. (TO80)	E	16.9	50 - 145
Brock et al. (BR80)	E	14.1	50 - 157
Jones and Brooks (JO74)	E	16.4 & 21.6	50 - 170
Morris et al. (MO74)	E	16.9 & 21.1	40 - 140
Wilczynski et al. (WI84)	E	17.0 - 27.5	33 - 151
Barker et al. (BA83)	E	25	120 - 150
Bohannon et al. (BO76)	P	25.0	
Cote et al. (CO80)	T	14.2 & 16.9	

a) E = experimental measurement; P = phase shift analysis;
T = theoretical calculation based on potential model.

possible, to an accuracy of at least 0.002. This is needed to check the result of their analysis which suggests experimental evidence for an isospin splitting of the triplet P-wave phase-shifts but in the opposite sense to that used in the phase shift analyses of Bohannon et al. (BO76) and of Arndt et al. (AR77).

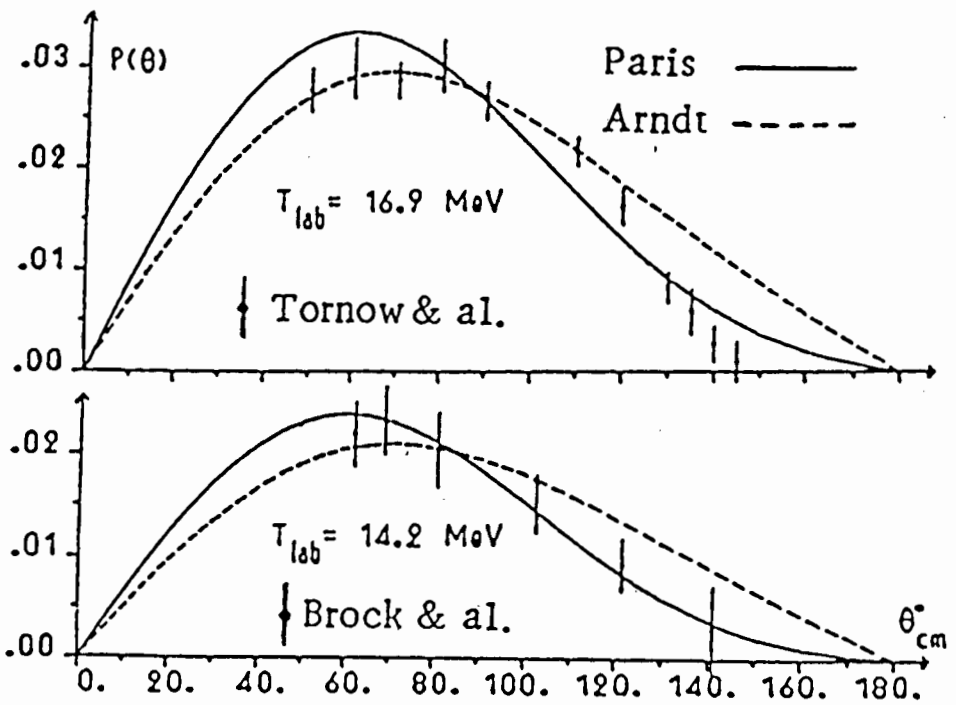

Fig. 1.3 n-p polarization measurements at 14.2 MeV and 16.9 MeV. The dashed line shows the 1977 Arndt phase shift analysis (AR77). Figure from CO80.

The n-p polarization measurements of Jones and Brooks at 21.6 MeV (JO74) and Morris et al. at 21.1 MeV (MO74) were presented as motivation by Bohannon et al. (BO76) for their re-evaluation of the entire n-p and p-p data set between 20 and 30 MeV. This was reported in 1976. The phase parameter values were compared with those from the previous phase shift analysis by McGregor, Arndt and Wright [MAW-X] (MA69). The inclusion of the new data

noticeably changed the central values of the isospin-zero phase shifts and reduced their uncertainties. More specifically: (a) the $^1P_1$, $^3S_1$, ε_1 and $^3D_1$ central values changed by more than 2 new standard deviations; (b) the phase parameter standard deviation for the $^3S_1$ dropped to 60% of its former value, while that for $^1P_1$ decreased to 70% of its former value; and (c) the evaluation fixed ε_1 at $+1.03^\circ \pm 0.57^\circ$, whereas previously the value was negative in contradiction to expectations from the deuteron data (from the sign of the quadrupole moment) and from models.

In particular the Bohannon analysis illustrates the usefulness of accurate polarization data in the determination of the D-wave spin-orbit phase-shift combination, which gives information on the various ^3D phases,

ie. $$\Delta^D_{LS} = (-1/60)(9\ ^3D_1 + 5\ ^3D_2 - 14\ ^3D_3) \ .$$

It has been pointed out (by Morris et al. and by Haeberli (HA77)) that there is an unexplained normalization discrepancy between the published data of M074 and J074. Bohannon et al. have suggested that the discrepancy between the data sets could be fairly well resolved by, for example, measurements of n-p $P(70^\circ)$ and $P(120^\circ)$ to an accuracy of ± 0.001.

Since the time of the Bohannon et al. phase shift analysis, Brock et al. (BR81) indicated that the J074 polarization values required adjustment to account for updated incident beam polarization values. This suggested that the M074 data should also be checked. On doing so, an inconsistency was noted. Although it was stated that $P_{inc}=0.35$ was used, on checking their P_{np} values $P_{inc}=0.50$ appears to have been used instead. Both J074 and M074 polarization values have therefore been adjusted as follows. In both cases the published asymmetries have been used, and the

appropriate updated incident beam polarization values used to re-calculate the analyzing power values (details are given in appendix 1.2). The Jones and Brooks values are now smaller than previously and the Morris et al. values have been increased by a large amount. The published values and the adjusted values are shown in fig. 1.4. It can be seen that there remains a discrepancy between the two experiments. More recent data at 22 MeV from Karlsruhe (WI84) are in closer agreement with the corrected values of Jones and Brooks.

These two sets of data (JO74 and MO74) made an important contribution to the Bohannon 25 MeV phase shift analysis, and unfortunately the adjustments to the data mean that some of the phase parameter values are probably in error, necessitating another re-evaluation of the data set.

The Bohannon analysis also shows a Coulomb splitting Δ^3P_{LS} between n-p and p-p scattering consistent with zero. If the splitting is as large as expected from various models (it is estimated as being about 0.08° near 25 MeV) it should be possible to detect it if analyzing power measurements are found to an accuracy of at least 0.002.

Another aspect of interest is whether or not the n-p polarization data at these energies favour zero-crossing solutions, which demand the inclusion of F-waves in the phase shift analyses and current phenomenological potentials. One n-p polarization measurement at 25 MeV (BA83) indicated that zero-crossing seemed to occur at $\theta_{CM} \cong 150^\circ$. However a subsequent and very recent large-angle measurement at 25 MeV (SR86) completely rules out this possibility. This large-angle measurement is considered more reliable because instead of detecting low energy

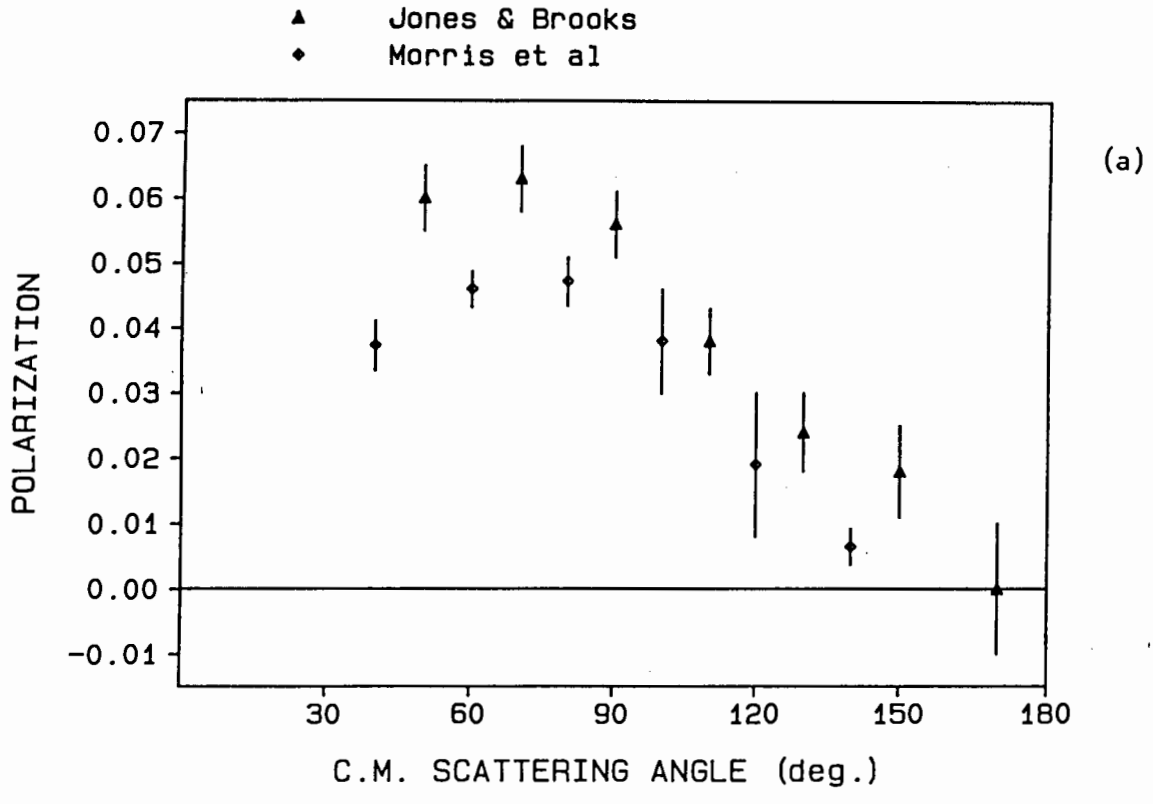

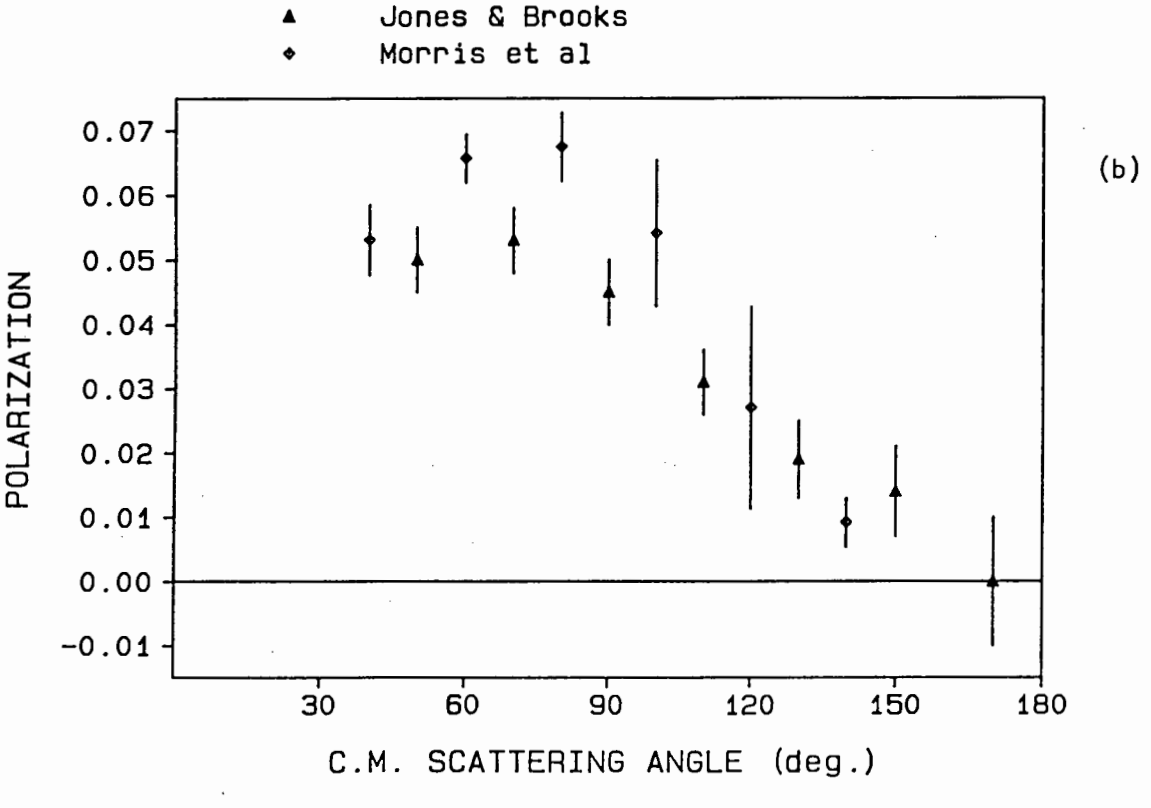

Fig. 1.4 Polarization data (refs JO74 and MO74) for E_n=21.6 MeV :
(a) original values; and
(b) adjusted values (see appendix 1.2).

neutrons using a conventional polarimeter (see fig. 1.5), use was made of a counter telescope for the recoil protons.

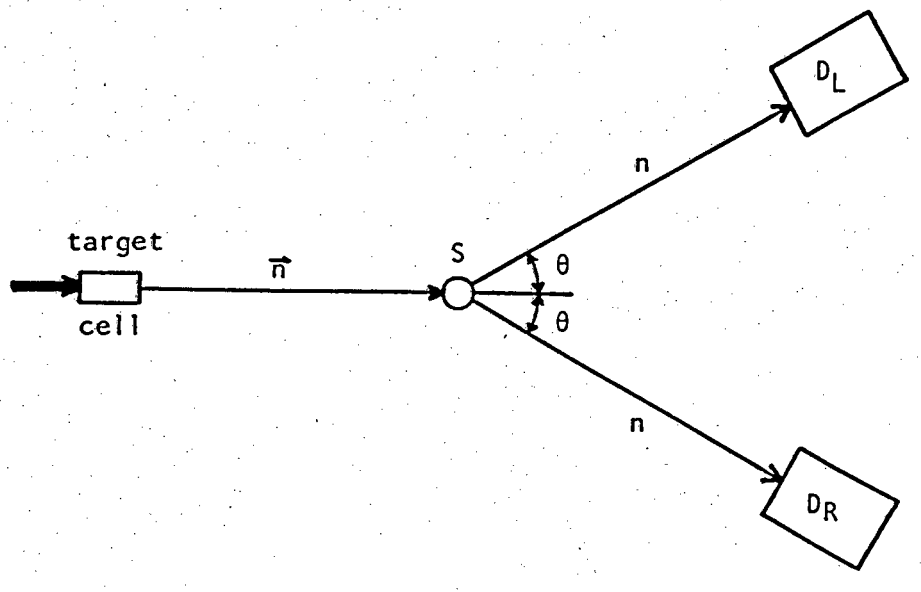

Fig. 1.5 Schematic view of the arrangement for a conventional neutron polarimeter. S is an active scintillation scatterer, D_L and D_R are neutron side detectors. S is bombarded with a source of polarized neutrons, and the scattered neutrons are detected in coincidence with the recoil protons.

1.8 Motivation for additional measurements

There is continuing interest in P_{np} for T=0 phase shift parameters. However, the presently available data are inadequate in terms of accuracy and inconsistencies. There is also interest in isospin splitting, and specific features like F-waves.

The level of precision required to meet these objectives demands not only high statistical accuracy, but also a matching control over systematic errors. Conventional double scattering experiments (see fig. 1.5) detecting neutrons (in coincidence with the recoil protons) usually face problems in obtaining good

statistics unless a "large" (>100g) active scattering target is used. This in turn introduces the need for large multiple-scattering corrections. The anthracene crystal polarimeter (BR74), on the other hand, gives high efficiency (~100%) in a small active target.

This work used a redesigned anthracene polarimeter with modifications aimed at eliminating instrumental errors as far as possible and calibrating scattering angle unambiguously. The analyzing power P_{np} at 21.6 MeV was measured using polarized neutrons from the $T(d,\vec{n})^4He$ reaction with $P_{inc}=0.25$. This was the only convenient source of polarized neutrons locally available. Facilities for rapid reversal of the incident neutron beam polarization, now so common in P_{np} measurements, were not locally available. However, the features of the modified anthracene polarimeter (rotating crystal) are such that this disadvantage is minimised.

CHAPTER 2

THE ANTHRACENE SCINTILLATION POLARIMETER

2.1 Brief Review

Previous n-p and n-d analyzing power measurements (JO74 and ST75) made at the National Accelerator Centre (NAC) were carried out using the scintillation polarimeter (BR74) developed at the University of Cape Town (UCT) (see Appendix 2.1). This polarimeter measures the left-right asymmetry, not of the scattered neutron, but of the associated recoil particle (proton or deuteron). The neutron scatterer is an anthracene (or deuterated anthracene) scintillation crystal in which the recoil p (or d) is internally detected. The method utilizes the directional effects (TS62,BR74) associated with the scintillation properties of anthracene crystals. The direction dependences of the scintillation response and the scintillation decay of anthracene are illustrated by two-parameter analyses of the photomultiplier outputs, L and S , for monoenergetic neutrons (fig. 2.1). For anthracene crystals the direction of minimum L coincides with the crystal b-axis and that of maximum L coincides with the artificial c'-axis, defined as the direction perpendicular to the ab-plane of the crystal.

The pulse shape discrimination (PSD) anisotropy characteristics are such that S is maximum when L is minimum and vice versa (BR74). An optimum orientation for asymmetry measurements is one in which there is maximum variation of S for proton recoils to left and right of the neutron beam direction. This is achieved if the a-axis of the crystal is aligned vertical

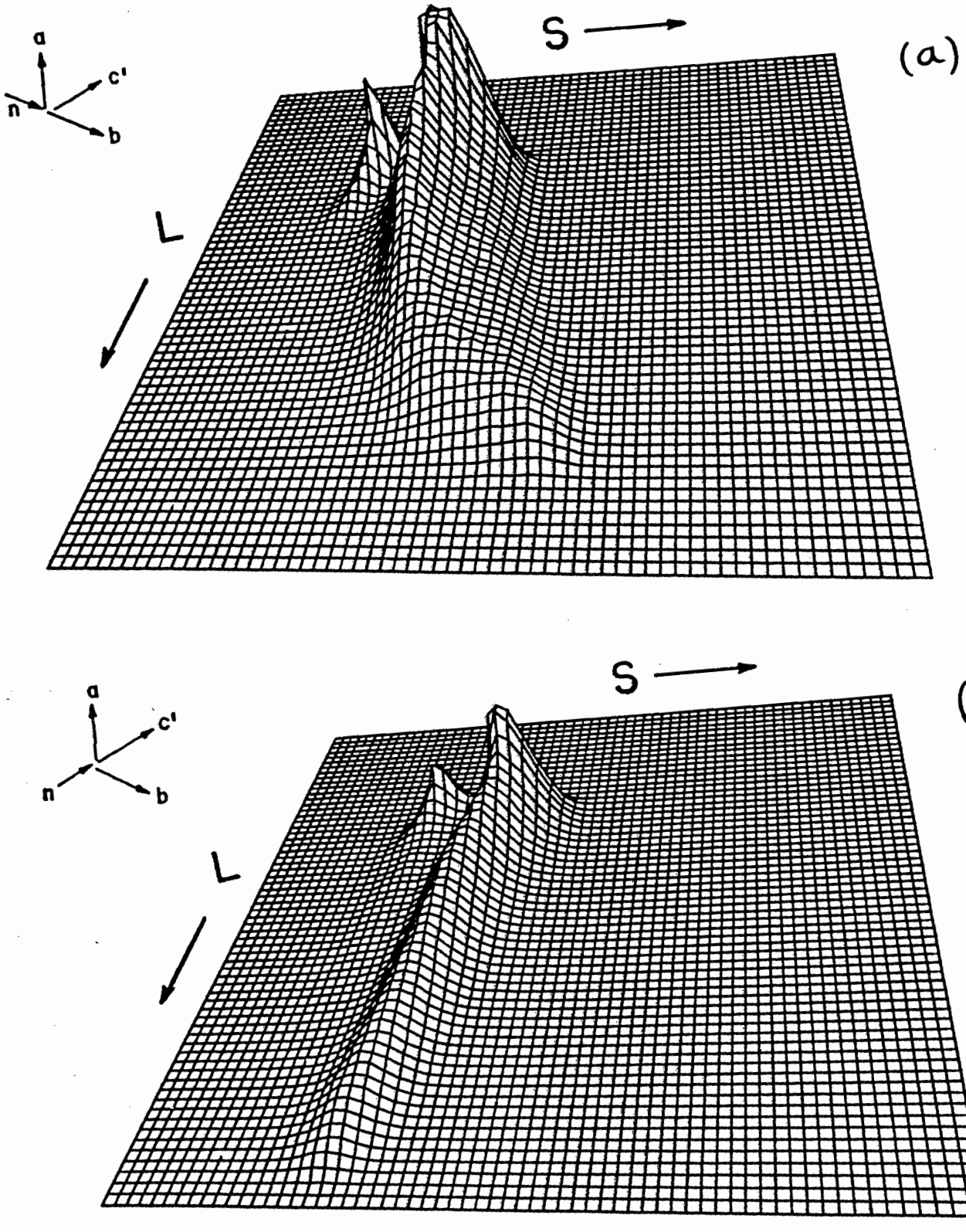

Fig. 2.1 LS proton recoil singles spectrum obtained with the incident neutron beam aligned along (a) the b-axis and (b) the c'-axis. Note the high-L threshold which was set so as to minimise the buffering of unnecessary events on magnetic tape .

(so that the bc'-plane is horizontal) and the neutron beam direction is at an angle of 30^{o} to the b-axis , as shown in fig. 2.2. An L-S spectrum obtained at this crystal orientation is shown in isometric projection in fig. 2.3. It can be seen that the proton events form two ridges over most of the length. These ridges correspond to protons recoiling into the forward quadrants on either side of a vertical plane through the neutron beam. By comparing the numbers of counts under each ridge, the left-right asymmetry of the proton recoils within the crystal can be determined.

This technique has been described by Bugg (BU81) as being "a truly remarkable development" which deserves wide application in the determination of the polarization of low energy neutrons. The scintillation polarimeter has the following advantageous features:

i) There is a high counting efficiency because primary scatters are detected including the non-planar (azimuth) events;

ii) data are collected simultaneously for all scattering angles;

iii) multiple neutron scattering is estimated to have a negligible effect on the observed asymmetry because of the small dimensions of the scintillation crystal target;

iv) the polarimeter may be used in an open geometry (since no shadow bars are required as is the case for the side detectors of a conventional two detector arrangement), thus eliminating the need for corrections to account for possible sources of in-scattering; and

v) although a high intensity source (e.g. the $^{2}H(\vec{d},\vec{n})^{3}He$ reaction) with high incident neutron polarization would be preferred, low intensity sources of polarized neutrons, such

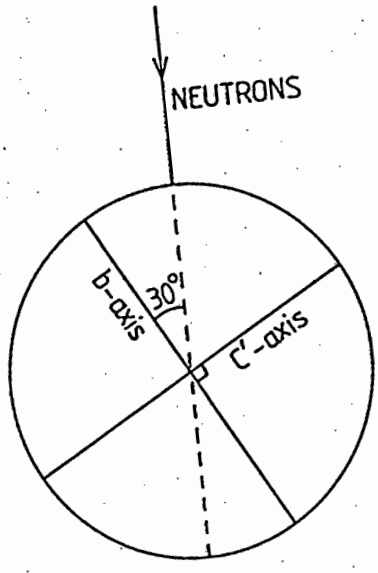

Fig. 2.2 The orientation of the crystal in one of the two possible polarization orientations showing the positions of the axes in the horizontal bc'-plane. The a-axis is vertical to the neutron beam (at right angles to the page).

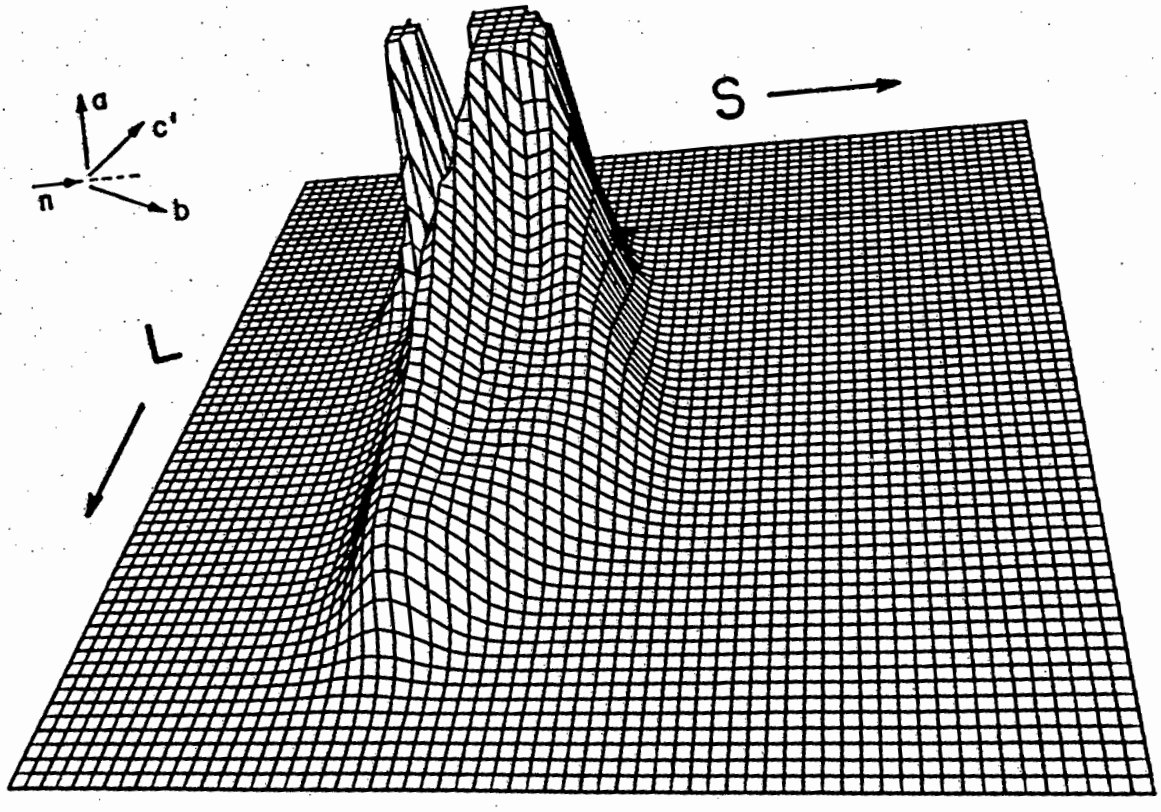

Fig. 2.3 LS singles spectrum obtained with the incident neutron beam aligned at 30° to the b-axis (see fig. 2.2.). The left-right proton ridges are clearly evident. See also fig. 4.9.

as the $T(d,\vec{n})^4He$ reaction, can be used to good effect. This is because a high count rate is still possible as a result of (i).

2.2 Further Developments

All polarization experiments have some means of effectively interchanging the number of scattered particles to the left and right of the incident beam. In the last decade or so this has usually been achieved by inverting the spin state of the incident beam; either via spin-precession of the neutron beam itself, or, when a polarization transfer reaction is the neutron source, by inverting the spin state of the charged particle used to induce that reaction. When spin-reversal is not available, then, in the conventional double scattering polarimeter for example (see fig. I.5), the left-right detectors may be mechanically interchanged. This procedure is aimed at eliminating systematic false asymmetries arising from differences in the efficiencies of the detectors and also from small misalignments of the detection apparatus.

In the previous use of the UCT anthracene scintillation polarimeter, the crystal was optically coupled to the face of the photomultiplier tube (in some cases via a lightpipe). Two positions, A and B, were defined (see appendices 2.1 and 4.3) at the asymmetry orientation (fig. 2.2). The detector assembly was mounted on a goniometer which enabled the crystal to be rotated in the horizontal plane so that the A and B crystal orientations could be interchanged by selecting the appropriate positions of the crystal axes with respect to the incident neutron beam. It is possible that the physical movement of the detection system could

cause fluctuations in gain due to the effect of the differing magnetic field of the earth experienced by the detector.

To minimise this problem more effectively than the use of magnetic shielding alone, the photomultipliers of the present detector were kept stationary and the A and B positions were obtained by mounting the crystal out of contact but close to the photomultiplier cathode, so that it could be rotated through 180° about the beam axis (see fig. 2.4). This ensured that mechanical movement of the detection system was reduced to an absolute minimum, and effectively turned the laboratory (ie. the crystal) around the neutron beam instead of rotating the beam in the laboratory. A design feature was a line-of-sight aperture which was incorporated in the crystal holder mounting to aid in the accurate positioning of the detector. The crystal could be conveniently removed from the holder for this purpose and then be accurately replaced in a reproducible manner.

In the polarization measurements LS spectra such as fig. 2.3 were accumulated in the A and B crystal orientations. In order to render the measurements less sensitive to small electronic drifts or other instrumental instabilities, the crystal was rotated between the A and B orientations by mechanical drive at regular short intervals (typically 1 minute). Thus each data acquisition period was equally divided between the A and B orientations, in such a way as to ensure that effects of electronic drifts, if present, should be the same for the A and B spectra.

To neutralise asymmetries possibly arising from differences in the optical properties or light collection from opposite sides of the crystal, leading to different measured pulse heights for the two crystal orientations, a symmetrical two photomultiplier

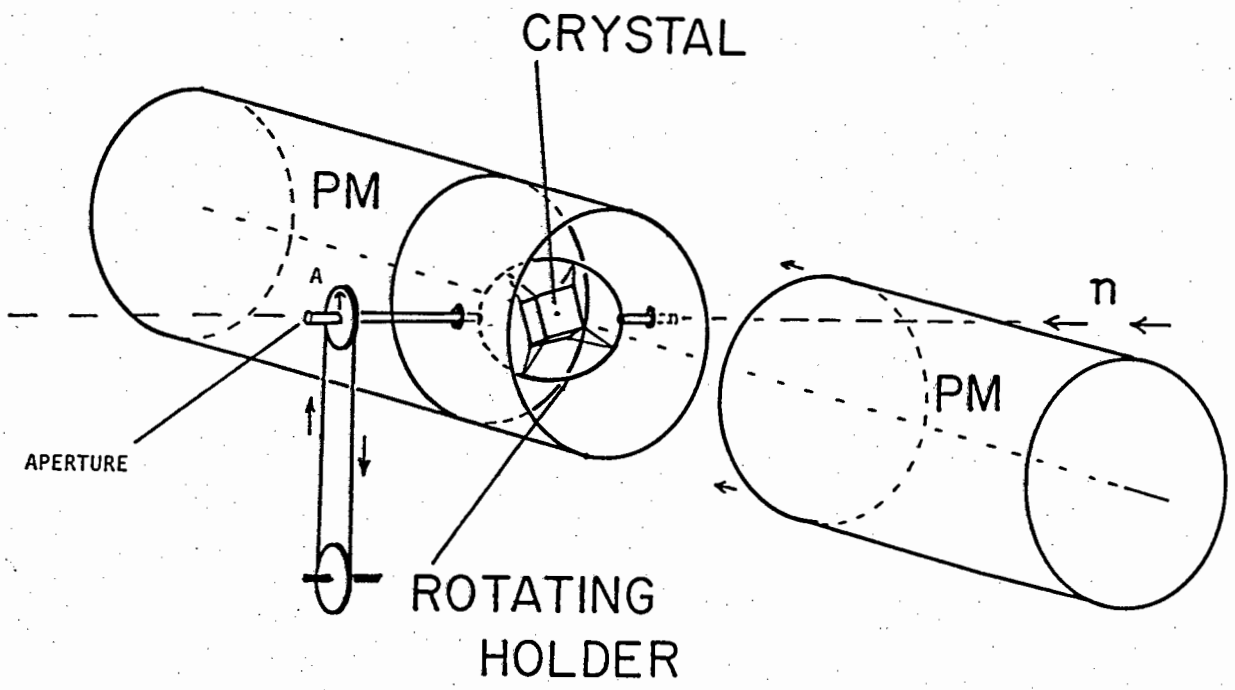

Fig. 2.4 A sketch of the two-photomultiplier polarimeter. The crystal is shown in the "up" position, indicated by the arrow A. The crystal alternated equally between this position and the arrow "down" position during polarization runs. The aperture in the hollow shaft was used, with the crystal removed, to check the alignment of the polarimeter on the neutron target.

arrangement was developed as shown in figure 2.4. The slow signals from the two photomultipliers were summed together after first ensuring that the separate outputs were similar in amplitude. The procedure for achieving the latter (via high voltage adjustment) was not critical for producing matched A and B pulse heights (see Appendix 2.2). The fast signals were also summed at the input of the pulse shape discrimination system (see fig. 3.4).

The two photomultiplier set-up is very photon efficient even though the crystal is not optically coupled to the cathode face, since much of the light falls directly onto one or other of the phototube faces. Extensive pulse height resolution tests were carried out to optimise the light collection using this system. Figure 2.5(a) shows a typical ^{60}Co gamma pulse height spectrum as

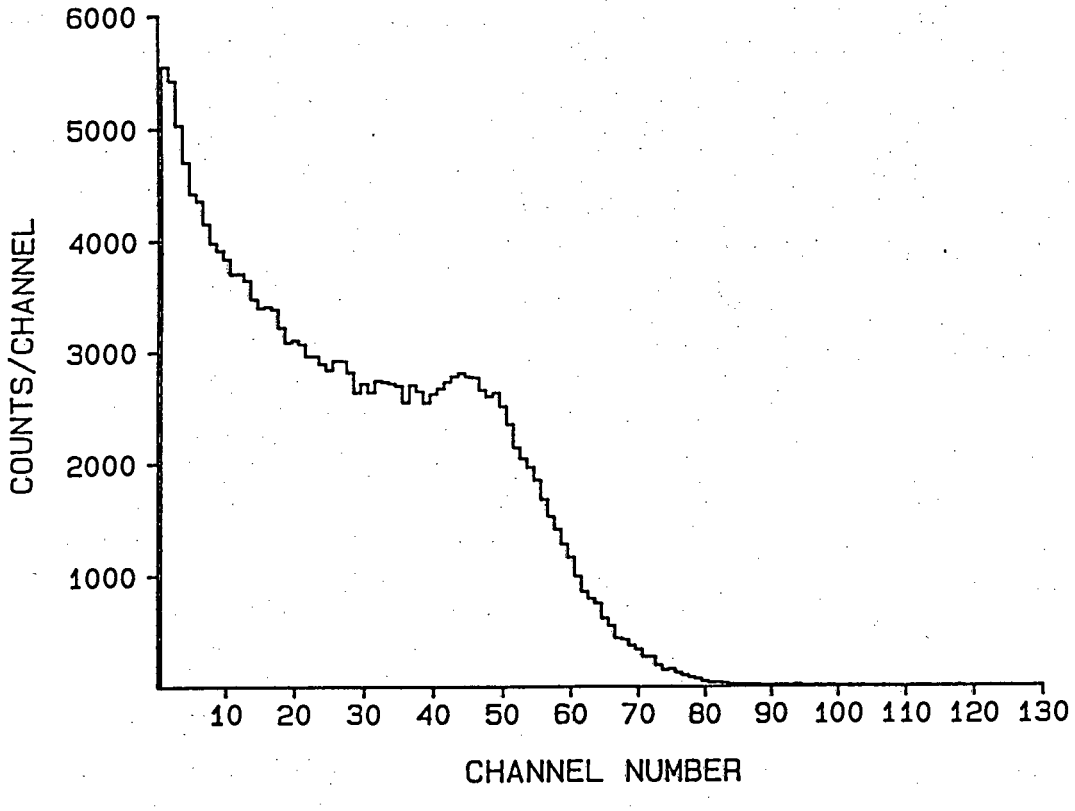

Fig. 2.5(a) ^{60}Co spectrum obtained from a single photomultiplier tube viewing the crystal mounted in air. Anthracene-2 was the scintillation crystal.

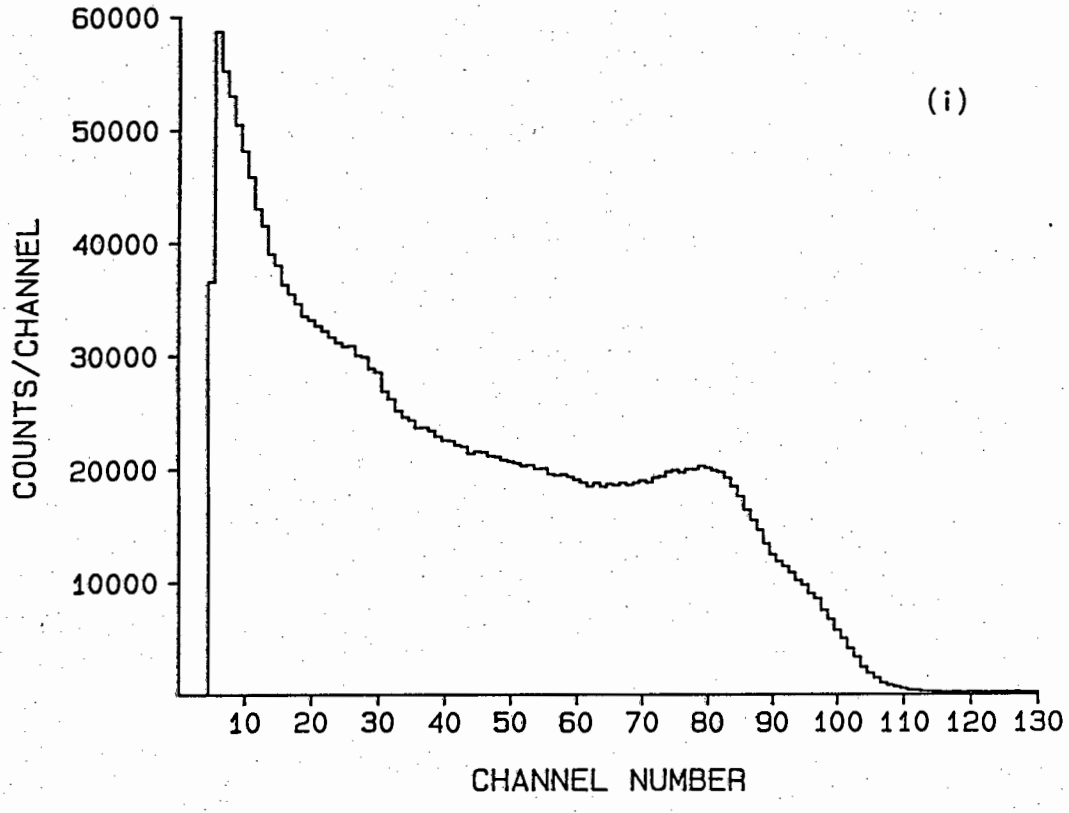

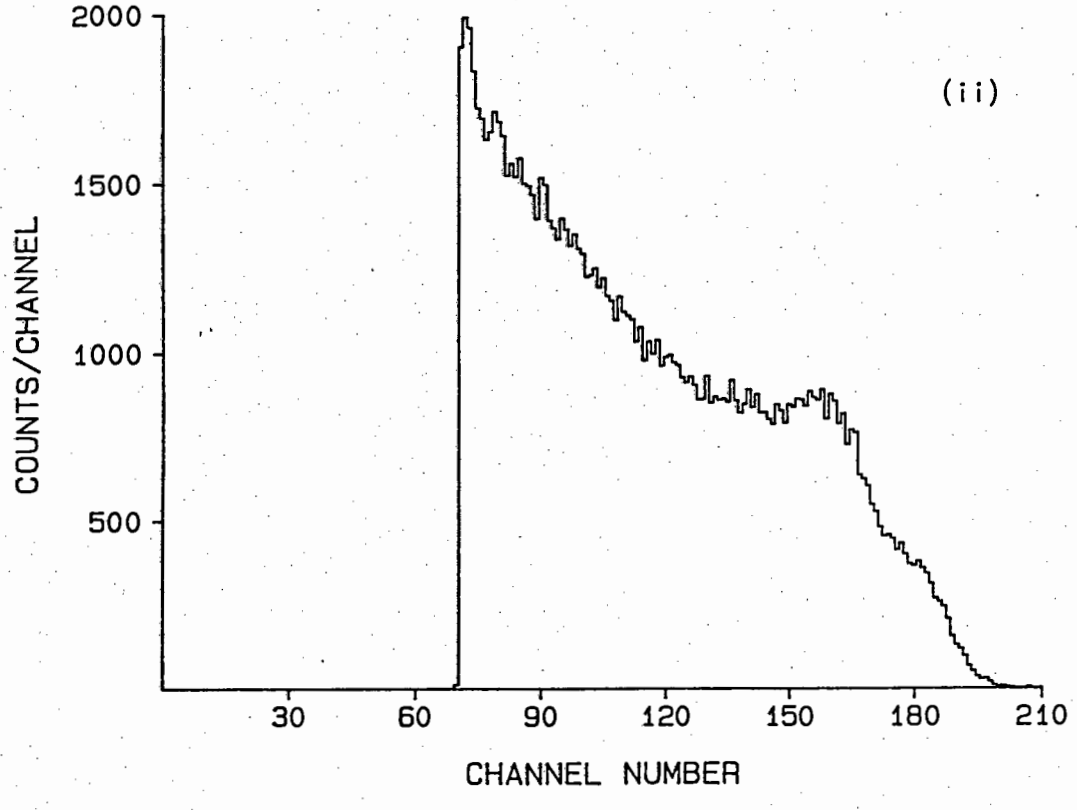

Fig. 2.5(b) ^{60}Co spectra obtained from the two-photomultiplier detection system viewing
i) the Anthracene-2 crystal mounted in air; and
ii) the Anthracene-1 crystal mounted in air.

measured by a single photomultiplier. The resolution is not particularly good, as may be expected for this geometry. Examples of the spectrum obtained using the summed outputs of the two-photomultiplier arrangement (fig. 2.4) are shown in figure 2.5(b). The good resolution is demonstrated by the clear double Compton edge associated with the two γ rays (1.17 & 1.33 MeV). This resolution is comparable with that obtained when the crystal is coupled directly to the cathode face of a single photomultiplier via a lightpipe.

In the data reduction process the LS spectra are divided into bins, each bin corresponding to a certain range of recoil angles. The modified polarimeter employs a new method for defining the angle bins. This method is based on direct observations of the scattered neutrons in coincidence with the recoil protons detected in the polarimeter crystal. Figure 2.6 indicates the scattering of incident neutrons at laboratory angle θ in the bc'-plane of the crystal. Events were selected by requiring a coincident neutron in a second detector at that angle in this plane. Details as to how the angle bin spectra were derived using these coincidence runs is given in the chapter on data reduction.

This new method for the angle calibration is superior to that used previously (BR74), which depended on knowledge of the response characteristics -total light versus energy- of the crystal for both the b and c' orientations.

To summarise then, the important new features of the modified polarimeter are

i) a rotating scintillation crystal;

ii) a symmetrical two photomultiplier arrangement; and

iii) a side detector for aiding the calibration of the proton recoil pulse height in terms of the scattered neutron angle.

In addition, as explained in detail later, a new correction procedure to neutralise drifts, which is applied in the data-reduction, has been developed.

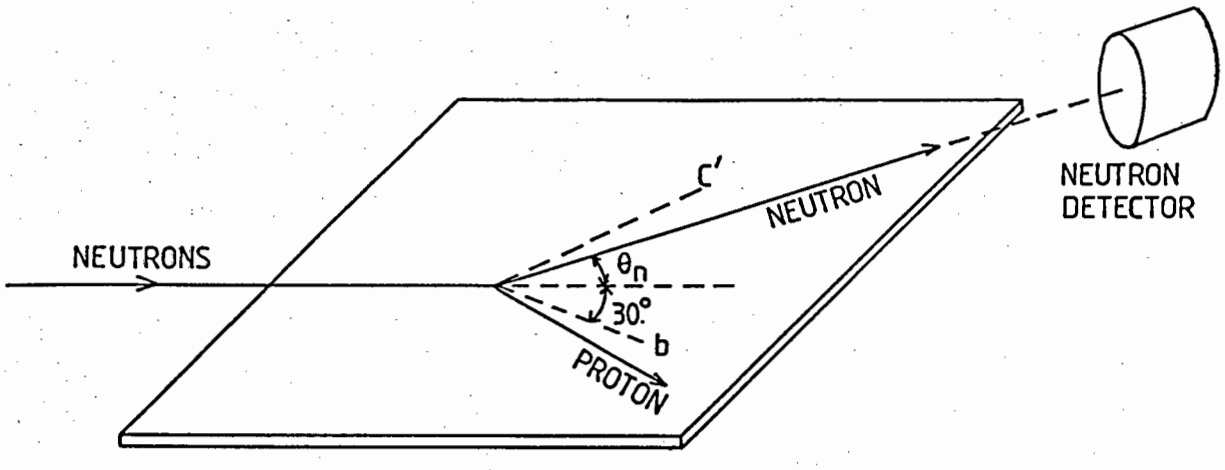

Fig. 2.6 A schematic diagram showing the detection of scattered neutrons by a side detector for calibration purposes.

CHAPTER 3

THE EXPERIMENT

3.1 Neutron production

Polarization measurements were made using neutrons produced by the $T(d,\vec{n})^4He$ reaction (see fig. 3.1). Tritium in a gas cell (0.75 atmospheres) was bombarded with 5 MeV pulsed deuterons produced by the Van de Graaff accelerator at the National Accelerator Centre, Faure. The deuterons were delivered at 500 ns intervals with a mean current of about 1 μA. Neutrons emitted at either 0^o or 20^o to the deuteron beam were used in the experiments. Unpolarized 22 MeV neutrons emitted at 0^o were used to collect null asymmetry data. These null data runs served as a monitor of systematic instrumental error of whatever origin. The use of the null data to correct for systematic false asymmetries where necessary is explained in more detail in a subsequent chapter. Polarized 21.6 MeV neutrons emitted at 20^o to the incident beam were used for the asymmetry measurements.

In each case the primary component in the neutron spectrum was selected by time-of-flight, the flight path in most runs being 0.3 m. In some runs the quality of the neutron source was independently monitored using an additional liquid (NE213) scintillator detector placed between 2 to 3 metres from the tritium target. A typical time-of-flight spectrum obtained from this monitor is shown in fig 3.2.

Although a substantial tail portion of the prompt gamma ray peak was usually included in the neutron window at the 0.3 m flight path used for the asymmetry measurements, the associated Compton electrons were easily separated from the neutron scattering data (recoil protons) by the PSD technique.

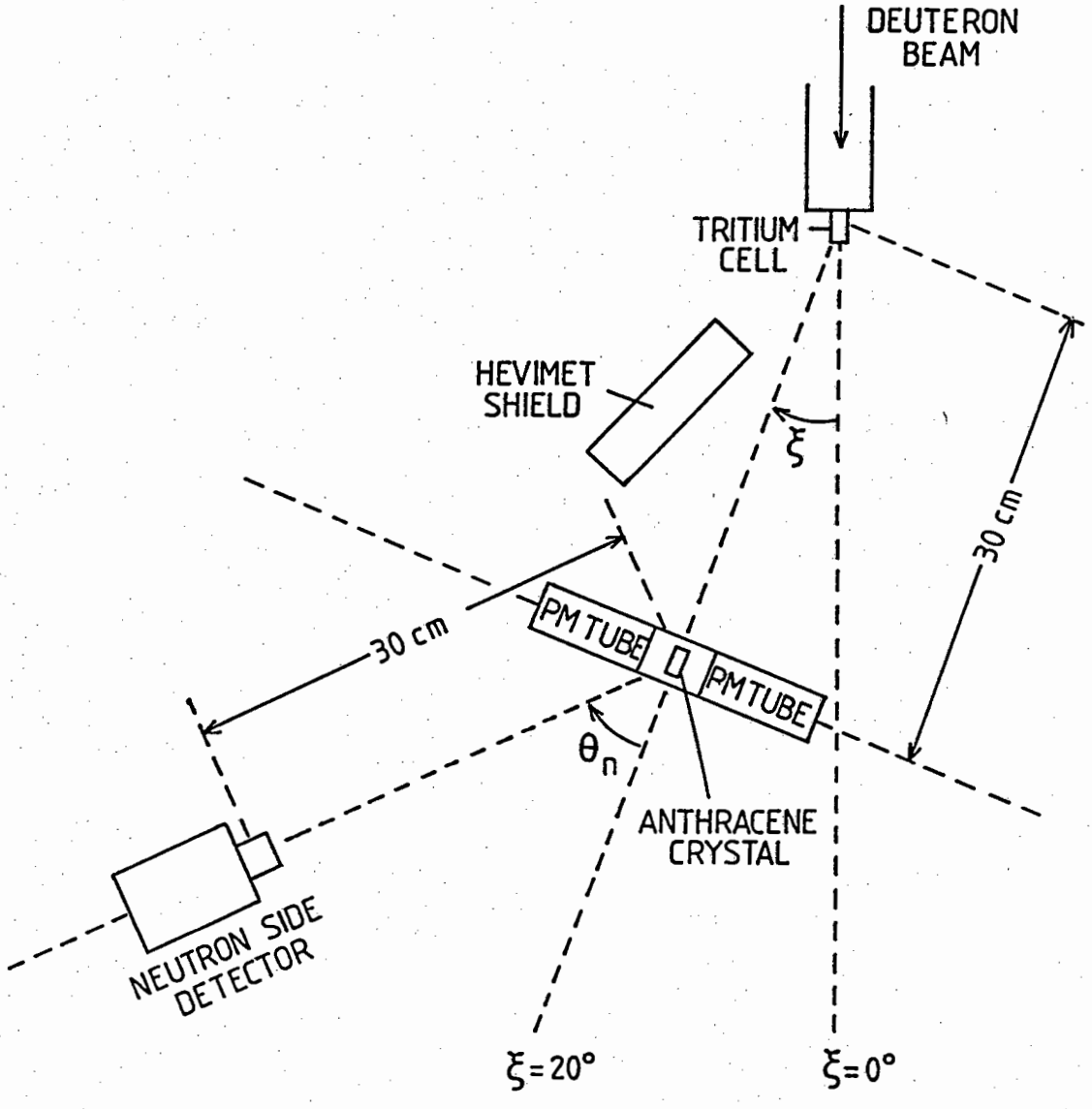

Fig. 3.1 The experimental geometry. Distances indicated are typical for the various runs. The hevimet shield was required only in those runs during which the neutron side detector was introduced (for the recoil angle calibration).

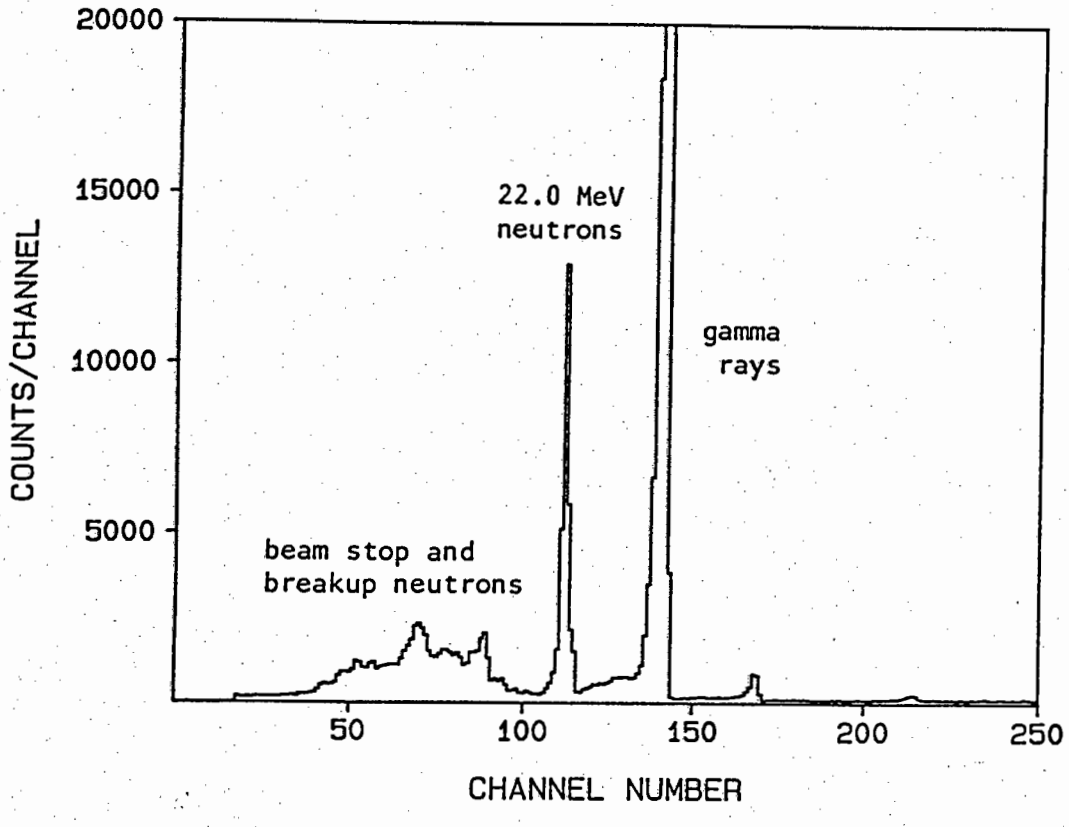

Fig. 3.2 Neutron T.O.F. spectrum as measured by a NE213 liquid scintillation detector placed at a few metres from the $T(d,\vec{n})^4He$ neutron source. The deuteron energy was 5 MeV and the reaction angle $\xi=0^{\circ}$. Pulse shape discrimination was not used.

3.2 Experimental geometry

During the asymmetry measurements, the polarimeter was mounted in completely open geometry so as to minimise the number of scattered neutrons incident on the anthracene crystal. The presence of a scattered component in the neutrons selected by the time window can vary the incident beam polarization significantly from that assumed for the direct beam. The detector arrangement for the entire experiment is shown in fig. 3.1. The angle calibration measurements were made separately, and the side detector and shield were removed during the asymmetry measurements. The set-up was placed on top of an aluminium plate

lined with appropriate angle scales (fig. 3.3). The plate, which rested on a horizontal table, could be rotated about a pivot on the table positioned immediately below the tritium target. This enabled a convenient and reproducible way of selecting different neutron reaction angles without affecting the relative positions of detectors and shielding (in the case of the calibration runs). Any one of a number of positioning holes along the central axes of the plate could be placed over this pivot point, to select different neutron flight paths. The height of the table was carefully adjusted to ensure that the neutron beam passed horizontally through the crystal, care being taken to keep the table top level. The zero degree line on the plate was then accurately positioned to within $\pm 0.1^{\circ}$ to coincide with the zero degree beam direction by means of plumblines and a theodolite. The polarimeter was then positioned on the plate over a central pivot (fig. 3.3). The scintillation crystal was removed and the line-of-sight aperture (fig. 2.4) used to make minor adjustments to ensure that the polarimeter was accurately aligned.

The crystal was mounted with its a-axis vertical and the b- and c'-axes in the horizontal plane. With the polarimeter at the $\theta_n = 0^{\circ}$ mark, the anthracene crystal was oriented so that the b-axis was at 30° to the beam direction , the polarization angle (see fig. 2.2). The b- and c'-axes could then easily be aligned along the beam by rotating the polarimeter about its pivot point by the appropriate angle. These orientations provided data which aided in the angle bin calibrations. When the detector was in the polarization position, the crystal was rotated through 180° about the beam axis at regular short intervals (typically once a minute) during data collection. These two crystal orientations were

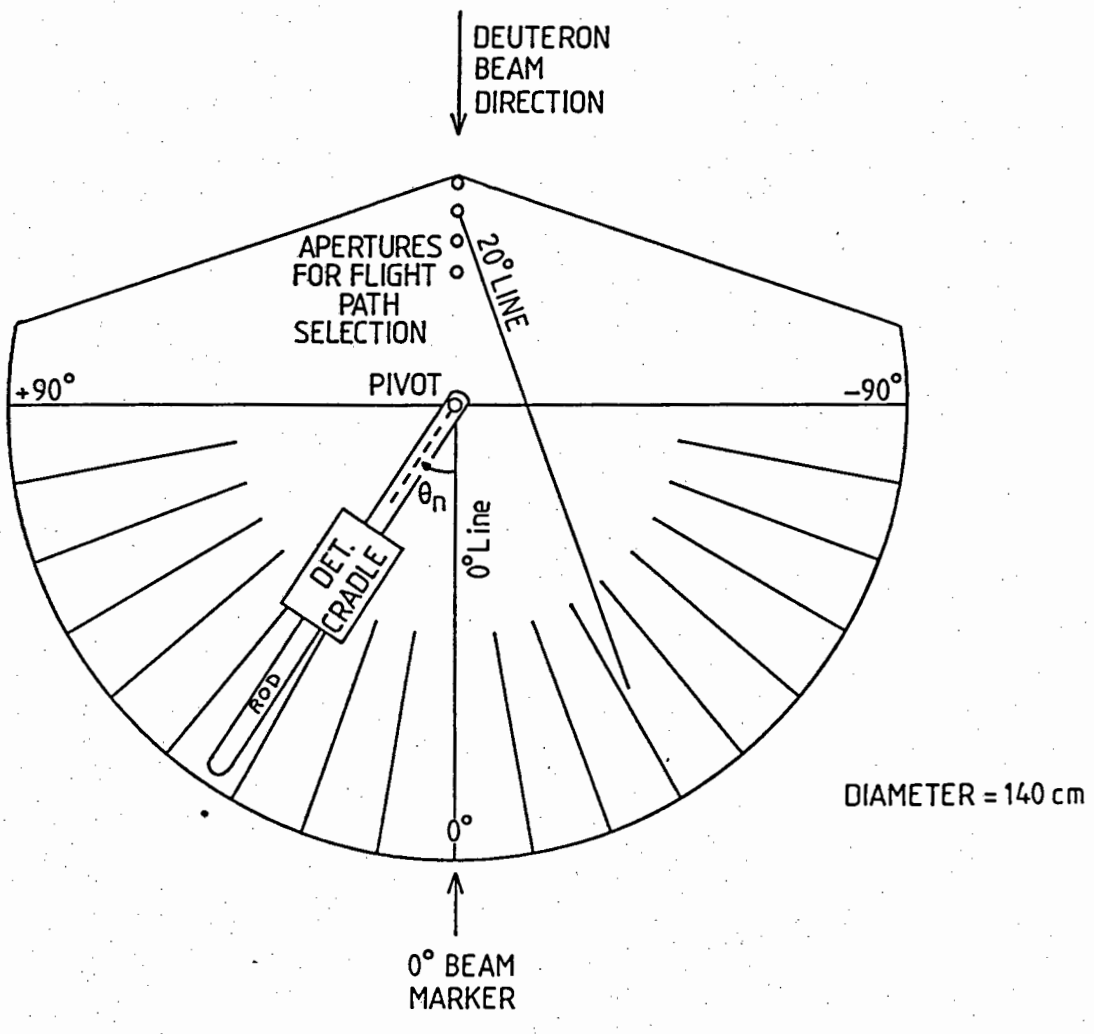

Fig. 3.3 The aluminium plate on which the detectors were arranged (see also fig. 3.1). The plate rested on a table. One of the apertures was selected and placed over a pivot on the table aligned below the tritium target. The anthracene polarimeter was mounted above the pivot on the plate and, for angle calibration runs, the side detector (NE213) was mounted on the detector cradle. The drawing shows the plate aligned for a null run ($\xi=0^{o}$). For polarization runs ($\xi=20^{o}$) it was rotated by 20^{o} about the pivot in the aperture.

referred to as "up" and "down" according to the position of a mark on the rotating wheel mechanism. The "up" and "down" signatures were thus related to the A or B crystal positions as given by the orientation of the crystal at the time of its placement into the holder (see appendix 4.3).

The side detector(s) used for the angle calibrations consisted of a liquid scintillator (NE213) mounted on an RCA8575 photomultiplier tube. The detector was placed on a cradle which was able to rotate about the central pivot via a flat rod which acted as an angle selection marker. The cradle was able to slide along the calibrated rod enabling easy positioning at the desired flight path. The detector could then be set at the required neutron scattering angle. The side detector was shielded against direct neutrons from the source target by blocks of hevimet, each new scattering angle measurement necessitating a rearrangement of the shielding.

Each time the experiment was set up it was necessary to carry out a series of calibration runs with the side detector(s) placed at a sufficient number of neutron scattering angles. So as to avoid possible in-scattering of neutrons from the side detector shadow shielding during the asymmetry measurements, the calibration runs were done separately. Although two side detectors placed at equal angles on either side of the vertex detector were sometimes used, usually a single side detector was employed. In this case the polarimeter crystal was rotated between the up and down orientations during the calibration runs.

3.3 Electronics

The scintillation crystal was viewed by two RCA8850 photomultiplier tubes (see fig. 3.4). Two pulse outputs, slow and fast, were taken from the photomultiplier circuitry. The slow (dynode) outputs were T'eed into a single pre-amplifier using cables of equal length. The pulse output was further amplified and this provided the total light output pulse, L.

The rest of the pulse processing is explained with reference to the block circuit diagram (fig. 3.4). In the two-phototube experimental runs the pulse shape discrimination pulse S was produced via the LINK 5010 module (LINK) based on a Harwell design (AD78) . The primary function of the LINK in standard applications is to provide a logic output which is linked to a bias threshold which can be set so as to distinguish between neutrons and gamma rays. There are also analogue signals available (X and Y) whose use is intended for display purposes.

The fast outputs were taken from the anode of each photomultiplier and directed to a specially made impedance matching unit whose output (the sum of the two inputs) was sent to the signal input of the LINK. The Y display output ,which is unsuitable for driving an ADC , was inverted and the central portion of the resulting pulse was selected using a linear gate. The pulse was then amplified and further shaped to provide a usable S signal. Pulse height matching was achieved using the integrated output (not shown) from the LINK module so that in effect the S pulse was being matched. The pulses were obtained by bombarding the crystal with 22 MeV neutrons. The high voltage supply to each phototube was then adjusted (see appendix 2.2). The

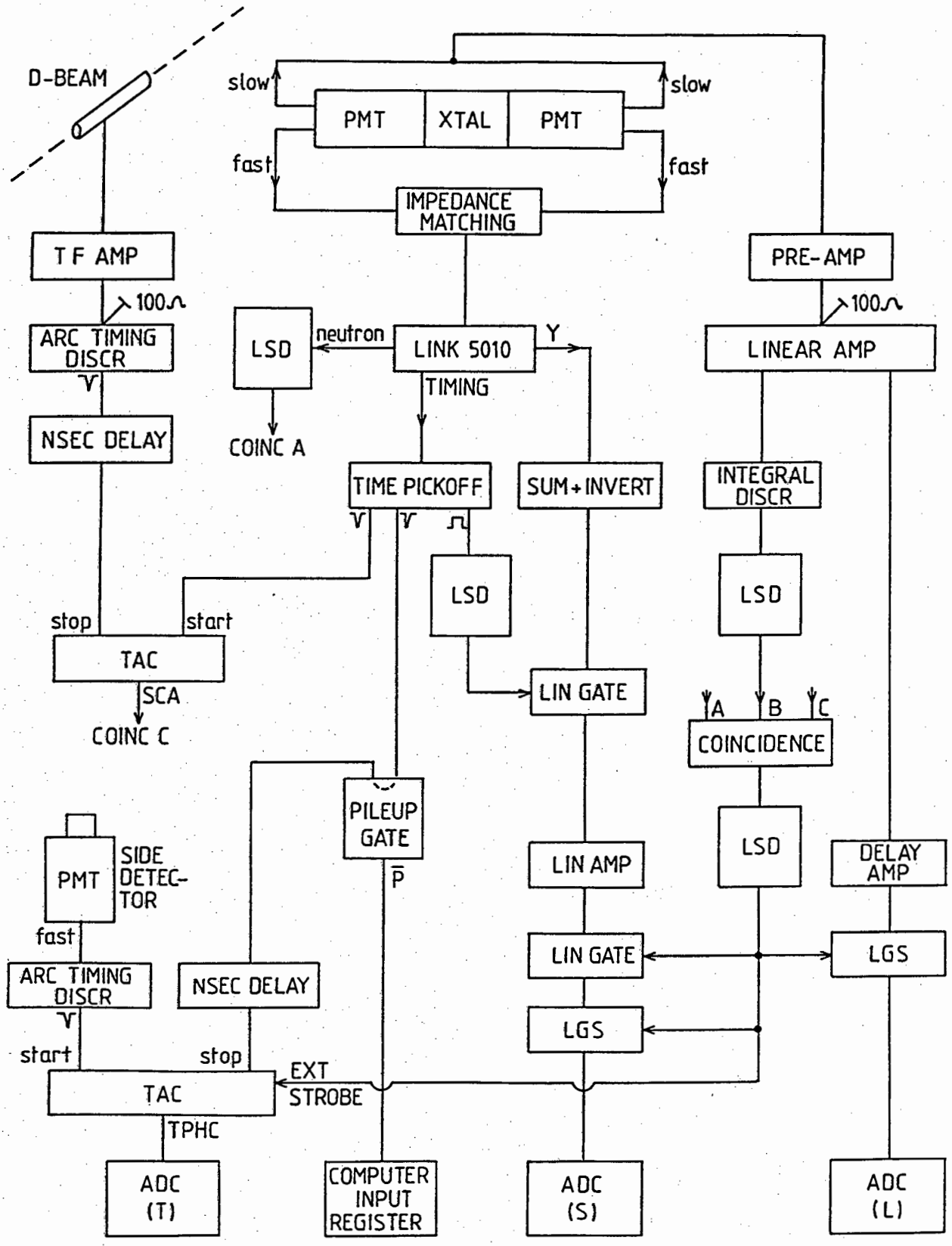

Fig. 3.4 The main electronic circuit used for the pulse processing.

matching of the L pulse was then checked by comparing ^{60}Co spectra collected in each of the two crystal orientations.

In some earlier runs (data sets B and C as given in chapter 5), the crystal was viewed by a single RCA8575 photomultiplier tube. The LINK module was not available at the time, and instead the S pulse was produced via the zero crossover method (AL61,RO64,GL74) as shown in fig. 3.5.

The left hand side of the circuit (fig. 3.4) is the standard pulsed beam time-of-flight arrangement. A window was set over the primary neutron peak and the TAC SCA logic signal, which was only produced when an event fell within the window, acted as one of three signals in coincidence which provided the gating signal for the linear gate modules.

In the angle-calibration runs, the fast signal for the scattered neutron time-of-flight measurement was taken from the anode of the side detector and used as the start pulse of a second TAC. The central detection system provided the stop pulse, after first being suitably delayed. The resulting TAC output pulse, representing the time-of-flight between the detectors, was also recorded.

The electronic arrangement for monitoring the beam condition is shown in fig. 3.6. A liquid scintillator (NE213) was optically coupled directly onto the cathode face of a RCA8575 photomultiplier tube. Both the dynode and anode signals were used so as to produce both a total light output pulse and a target to detector time-of-flight pulse. These pulses were processed as 2-parameter events and displayed on-line as L vs. T.O.F on a cathode ray oscilloscope. In addition, T.O.F spectra were recorded at regular intervals.

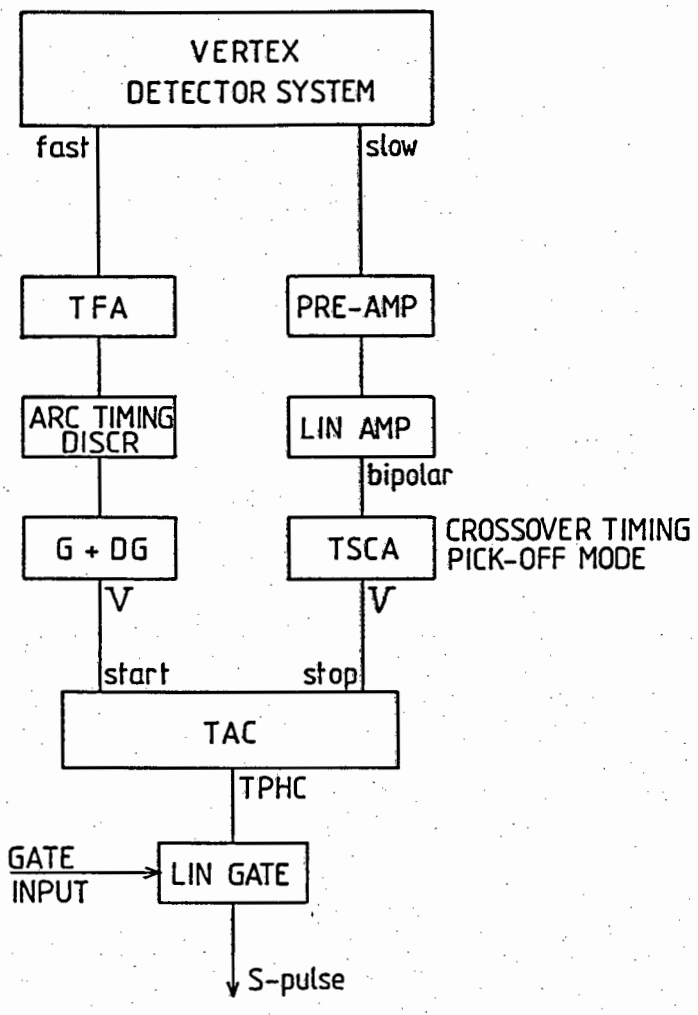

Fig. 3.5 The zero crossover method used to extract an S pulse in some of the runs. "Vertex" here refers to the anthracene crystal photomultiplier detection system.

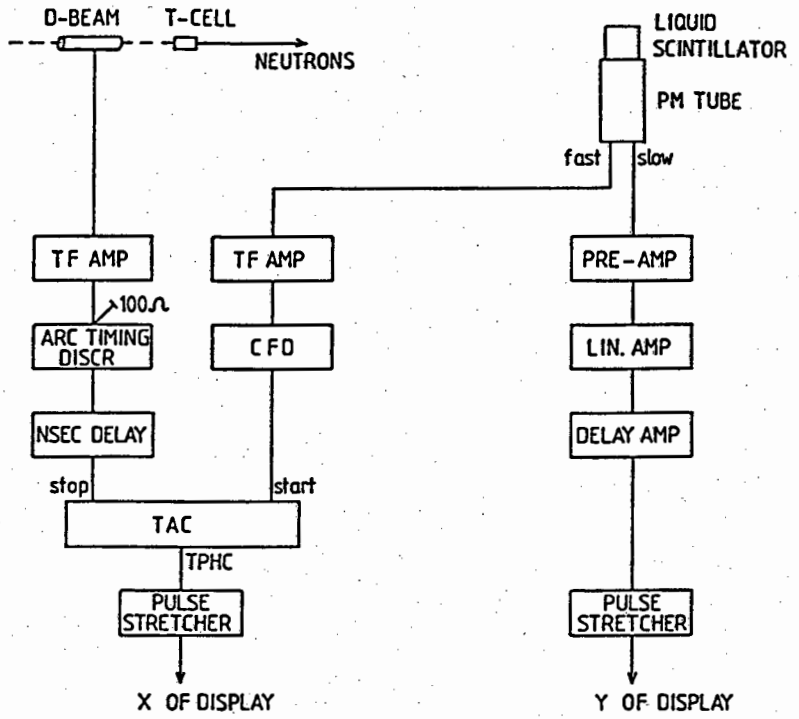

Fig. 3.6 The electronic arrangement used with the neutron monitor detector.

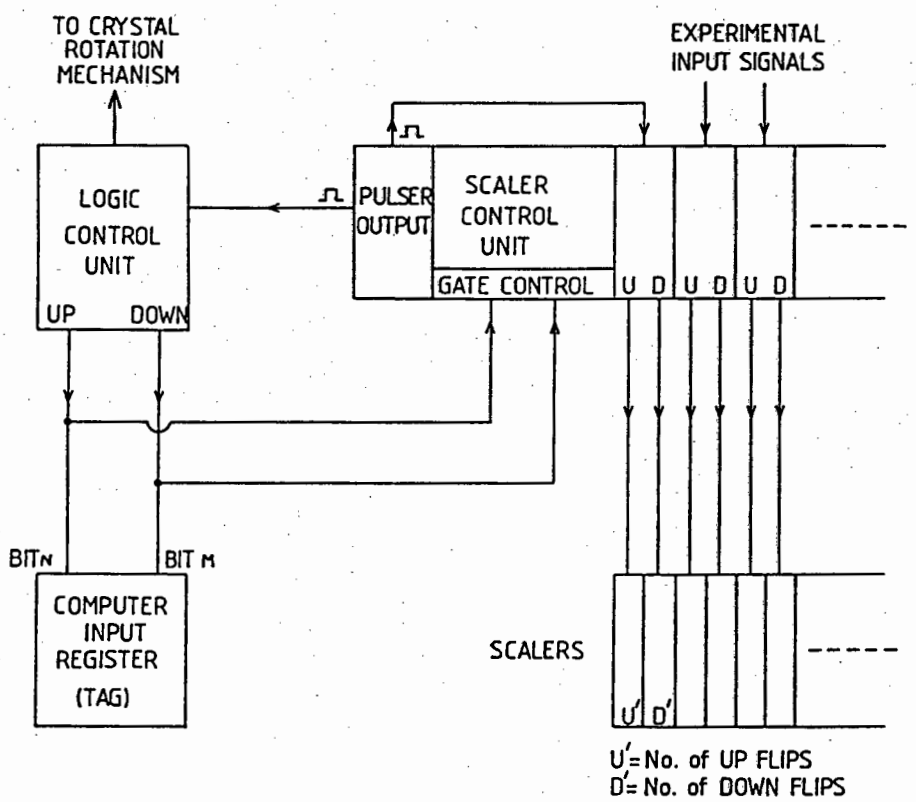

Fig. 3.7 A schematic diagram of the control system used to rotate the crystal at regular intervals. This was connected via a scaler control unit to various scalers so that counts corresponding to the two crystal positions could be recorded separately.

The automatic rotation of the crystal was controlled by a logic module which was designed and built for this purpose. This in turn was coupled to a scaler control unit (fig. 3.7). One of two alternative methods was used to determine when to rotate the crystal. The one method selected L pulses above a high discrimination level and the corresponding logic signals were sent to the logic control module. The other method (effectively a timer) used pulses of a pre-selected rate provided by the scaler control unit. The logic control module then counted the incoming signals and when a pre-set number of counts had been reached, the logic control box sent a signal to the polarimeter via a four-way cable. This activated a motor attached to the polarimeter which rotated the crystal via a pulley (fig. 2.4). After rotating through 180^{o} the mechanism activated a microswitch which caused the motor to stop. At the same time a signal was returned to the logic control module to reset the internal timer and to switch the gate control signal. The net effect of rotating the crystal without operator intervention was effectively equivalent to regularly inverting the spin state of the incident beam.

3.4 Data acquisition

In the asymmetry measuring experiments, three parameters were recorded per event; namely the pulse height L, the pulse shape S and a tagging parameter. This tag was produced by sending a logic pulse generated by the logic control module to a 13-bit register. Two logic pulses, each corresponding to a crystal orientation (up or down), were converted into different fixed parameter values.

Each accepted event was buffered on magnetic tape under control of a data acquisition programme run on a PDP 34/15 computer. The L and S values were first checked to ascertain whether preset software threshold criteria were satisfied before the event was accepted for buffering. During the interval when the crystal was being rotated, no output was generated by the logic unit. These events were rejected via a software gate.

For the scattering angle calibration runs utilising the side detector, the event included an additional parameter T, the time-of-flight of the scattered neutron which was in coincidence with the recoil proton in the anthracene detector.

In order to minimise errors arising from pulse distortion due to random pulse pile-up in the anthracene detector, a pile-up rejector module was included in the electronic circuit (fig. 3.4). If a second signal was detected within a pre-set time after the first pulse, a logic signal generated by the module signifying a pile-up condition was directed to an input of the register. Hence a pulse pile-up event, identified by the tag parameter, could be excluded from the later off-line analysis. Since pile-up rejection is also incorporated in the LINK module, the above procedure acted as a back-up system for those runs using the LINK.

In addition to the runs at the polarization orientation (fig. 2.2), calibration runs were also made with the crystal oriented so as to align its b- or c'-axes with the neutron beam, thus giving LS spectra as shown in fig. 2.1.

Various gamma ray calibration spectra, usually with ^{60}Co being used as the source, were also acquired at regular intervals for the following purposes

i) the determination of the true zero (L_o) of the pulse height

scale (L_o was found by assuming that the amplifier gain calibration was accurate, and collecting spectra for a ^{60}Co source at two different gain settings. The channel numbers corresponding to the Compton edge were then used to deduce the zero energy channel number.) ; and

ii) to have a record of the spectra used for the pulse height matching of the central detector system, as well as information on the pulse height resolution.

All of the above spectra, as well as various time-of-flight spectra, were transferred to magnetic tape for later processing. In addition various scaler readings (such as total number of events, number of crystal flips, number of coincidence events etc.) were recorded. The scalers provided on-line monitoring of the experiment and provided information for cross checking during the off-line data analysis.

CHAPTER 4

DATA REDUCTION AND CORRECTIONS

4.1 Introduction

The raw event-by-event data were processed off-line on a SPERRY 1100 computer and were sorted into 2-parameter (LS) spectra. The calibration data were analysed so as to determine the angle bin boundaries (in the LS plane) associated with the scattered neutron angles. The angle bins corresponding to various scattering angles were defined, then a spectrum was obtained for each bin, from which the left-right asymmetry was extracted for the corresponding scattering angle.

However carefully measurements may be made and corrections estimated, the possibility of an undetected systematic false asymmetry in this experiment remains. In order to minimise this risk, the off-line data reduction of these experiments included checks to detect possible hidden instrumental errors (eg. due to electronic drifts) and to correct for these errors. The approach was to detect shifts between A and B spectra due to instrumental errors and to correct for these shifts while at the same time taking care not to eliminate effects due to true asymmetries, ie. the aim was to discriminate against systematic error only. To develop and test these correction procedures, computer simulated spectra were used extensively.

Another problem is the escape of recoil protons from the crystal surface. The L and S coordinates generated by the escaping protons are differently related to the proton energy and direction than those of protons stopped in the crystal (see fig 4.9). Unless properly accounted for, the escape events can interfere in two ways. Firstly the presence of escape events in the spectrum has

the effect of diluting the asymmetry. Secondly they can interfere with the shift correction procedure thus causing false asymmetries.

A major part of the off-line data analysis concerned these corrections (shift and escape). The methods developed for these purposes are discussed before outlining the procedures used to implement angle bin calibrations, as well as the remainder of the data reduction.

4.2 Outline of method of determining the asymmetry

For the ideal experiment (no shifts, escapes etc.) the asymmetry ε can be extracted from the A and B spectra as follows (BR74). The A and B spectra are summed (the B spectrum first being normalised to the same total count value as the A spectrum). The median channel of the summed spectrum is then calculated, thus providing an estimate of the median channel for each of the A and B spectra. As shown in appendix 4.1, the exact determination of the median is not critical if the spectra coincide properly, ie. if there is no relative shift between the spectra. The position of the median then defines the number of left and right scatters in each spectrum, from which the asymmetry is calculated as outlined below with reference to fig. 4.1 .

The measured asymmetry is given by (see appendix 4.3)

$$\varepsilon_m(\theta) = \frac{\text{(protons left - protons right)}}{\text{total counts}} \quad .$$

This is a measurement of the asymmetry of proton recoils at all azimuthal angles for a given neutron scattering angle θ. This azimuthal asymmetry is related (BR74) to the planar asymmetry $\varepsilon_p(\theta)$ by the expression $\varepsilon_p(\theta) = (\pi/2)\ \varepsilon_m(\theta)$.

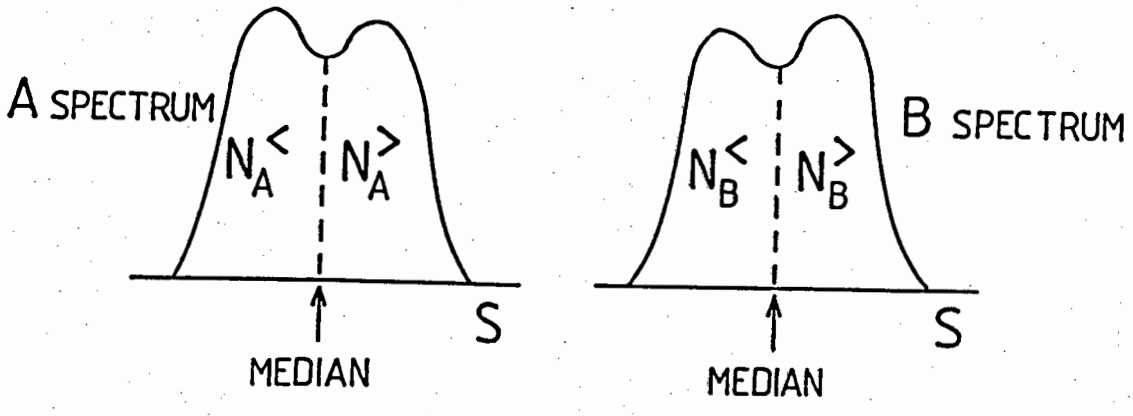

Fig. 4.1 Schematic sketch of an angle bin spectra pair. The spectra are divided by the median channel number into lower S- and higher S-sections denoted by the superscripts "<" and ">" respectively. $N_A^<$, $N_B^<$, $N_A^>$ and $N_B^>$ represent the integrated counts within these sections.

Hence $\varepsilon_P(\theta) = (\pi/2)(N_A^< - N_A^>)/(N_A^< + N_A^>)$ for the A spectrum

and $\varepsilon_P(\theta) = (\pi/2)(N_B^> - N_B^<)/(N_B^> + N_B^<)$ for the B spectrum.

ie. $\varepsilon_P(\theta) = (\pi/4)\{ (N_A^< - N_A^>)/N_A + (N_B^> - N_B^<)/N_B \}$.

If N_A and N_B are normalised to N , then

$$\varepsilon_P(\theta) = (\pi/4N)\{ N_A^< + N_B^> - (N_A^> + N_B^<) \} .$$

If the spectra contain an escape contribution, the asymmetry is effectively diluted (BR74). However, the fraction of escapes comprising the spectra can be estimated, and a correction can then be applied . As explained in appendix 4.2, false asymmetries are calculated from the A and B spectra if their median channels do not coincide because of a relative shift between the spectra. The detection and correction of the A-, B-spectrum shift was considered to be a limitation of the original procedures (BR74), and hence particular attention was given to resolving the problem in this work.

4.3 Development of a spectrum shift correction procedure using simulated data

The requirement

The left-right asymmetry value for a particular scattering angle is computed from two related spectra, the one corresponding to the scintillation crystal in the A polarization orientation, and the other to the B orientation (see appendix 4.3). Due to the nature of the analysis, any shift of the one spectrum relative to the other will result in a systematic false asymmetry being computed. This is explained in more detail in appendix 4.2. Although the design of the polarimeter was primarily aimed at minimising such shifts, even small remaining shifts can have a significant effect on the extraction of a reliable asymmetry value. This sensitivity is due to the fact that non-planar events are also recorded, and these fill up the central region of the spectrum between the left and right planar recoils (fig.4.2). A computer programme routine was therefore developed to detect and correct for these shifts.

Once the amount of shift (if any) is known , it is a simple matter to correct the spectrum for the given shift (and gain change). However, difficulty was experienced in developing a shift determination procedure which is rendered sufficiently insensitive to the statistical fluctuations which are always present in experimental data. In addition, any real asymmetry that is present in the data must not be disturbed and should also not affect the estimation of the correction.

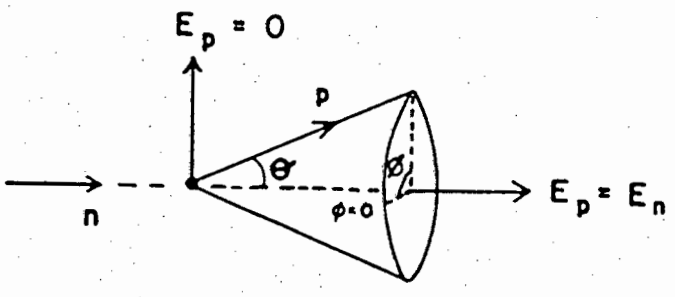

(a)

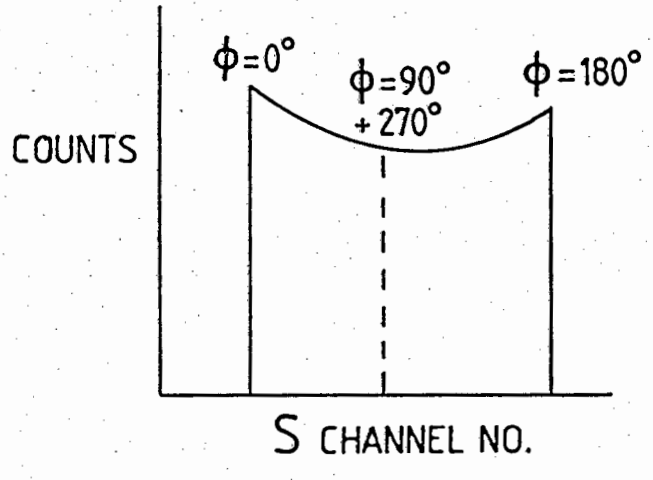

(b)

Fig. 4.2 Schematic representation of n-p scattering in the anthracene crystal.
(a) For a given neutron scattering angle θ_n, the proton recoil direction can lie anywhere along the surface of a cone of half-angle $\theta = 90^\circ - \theta_n$ about the incident neutron direction. The left and right planar recoils correspond to $\phi=0^\circ$ and $\phi=180^\circ$.
(b) A schematic sketch of the resulting angle bin spectrum which would be obtained with perfect resolution. The spectrum represents all azimuthal proton recoils corresponding to a given neutron scattering angle. The median channel number corresponds to proton recoils at $\phi=90^\circ$ and $\phi=270^\circ$. The left and right planar recoils correspond to the channel numbers at the edges of the spectrum.

Simulated data

A number of different shift deduction methods were investigated, and to aid in the selection of the most suitable procedure, simulated spectra were generated. It was found that two overlapping Gaussian curves provided a quick and accurate way of producing spectra which simulated the real situation. The following parameters could then be easily introduced into the simulated spectra, together with randomly generated statistical errors

i) a built in shift along the channel number axis, simulating the systematic errors;

ii) a built in gain change; and

iii) a known true asymmetry.

Statistical fluctuations were simulated by making use of a random number generator. The standard deviation of each channel count value was taken as the square root of the value, and a realistic simulation was possible by selecting random values drawn from a normal distribution centred about the count value. The statistical fluctuations were incorporated into each of the two Gaussians which were then each normalised to their original peak areas, before they were summed. This ensured that any spurious systematic asymmetry that may have entered in the process of adding the statistical fluctuations was eliminated.

A description of the shift-correcting procedure which was finally evolved is now given.

Kinked sine slide percentile method (KSSPM)

This is a method to determine shift and gain changes between A and B spectra (see appendix 4.3). Fig. 4.3 comprises a number of sketches to assist the following explanation of the method. In the

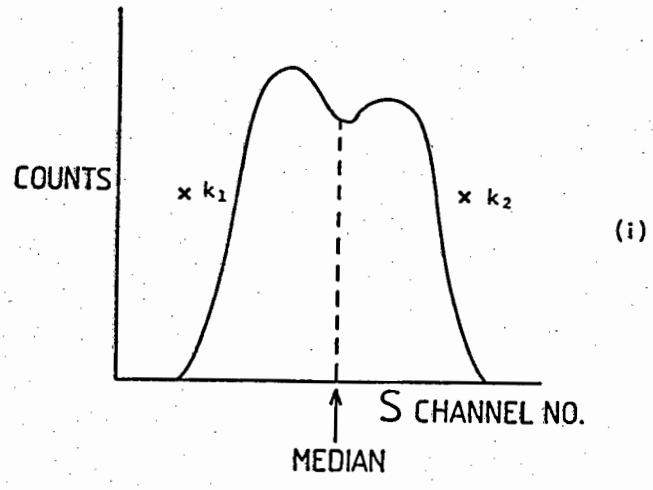

(i)

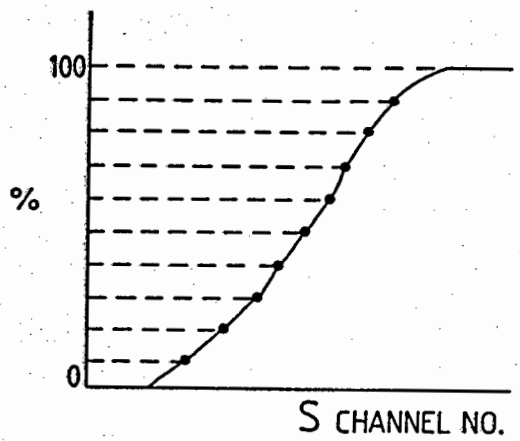

(ii)

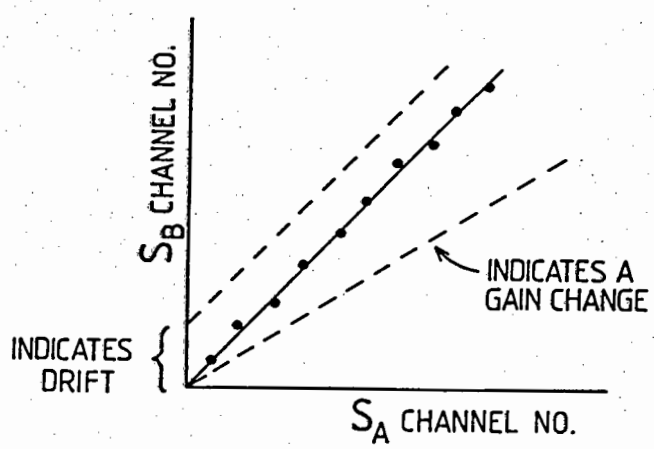

(iii)

Fig. 4.3 Sketches to aid in the explanation of the KSSPM shift correction method (see text). (i) is a schematic sketch of an angle bin spectrum (ii) is a plot resulting from the percentile method, showing the S channel number corresponding to the integrated count value (expressed as a percentage of the total number of counts in the spectrum) at that channel (iii) S channel numbers for the A and B spectra pair corresponding to preselected percentiles.

percentile method, the channel numbers corresponding to preselected percentiles are determined independently for the A spectrum and the B spectrum (fig.4.3(ii)). These points are plotted (B channel no. vs. A channel no. for each selected percentile value) and fitted by a straight line. The slope of this line was then taken as a measure of the gain change of the B spectrum with respect to A, and the intercept as a measure of constant shift (fig.4.3(iii)). This method by itself was found to work well for spectra identical apart from statistical fluctuations. However it proved sensitive to true asymmetries in the data and reduced these asymmetries unpredictably by determining an incorrect shift in the correction procedure. This problem was clearly due to a departure of the percentile level relationship (fig. 4.3(iii)) from linear when true asymmetries were present in the data.

The KSSPM thus attempts to first effectively remove any true, but unknown, asymmetry in the spectra before the percentile method is applied. Ignoring small asymmetries due to statistics, this is achieved by compensating for the height (ie. count) differences (which are manifestations of the true asymmetry) between the A and B spectra. This results in percentile points which lie on a straight line, as expected, rather than on a curve. Specifically, one of the spectra (normally B) is height (ie. count) adjusted on its left and right pulse height edges by factors k_1 and k_2 respectively, which are to be determined by the method (fig. 4.3(i)). The central count region is height-adjusted by factors varying smoothly from 1 to k_1 (or k_2) outwards from the median channel. This was at first accomplished via a linear sliding scale (KLSPM) assuming arbitrarily that the factor should increase

linearly with channel number from 1 to k_1 or k_2. A more realistic and satisfactory approximation (KSSPM) was afterwards introduced in which the increment in k was taken proportional to cos ϕ where ϕ is the proton recoil azimuthal angle. This is based on the fact that the left-right asymmetry is proportional to cos ϕ. In implementing this, the approximation $\phi \propto S$ was assumed.

After each spectrum adjustment, the percentile method is used to obtain shift and gain values together with a least squares value for comparison purposes. The height compensation factor is incremented, and the entire procedure repeated. The shift corresponding to the lowest least squares value is taken as the required correction.

When applying the KLSPM to the artificial spectra, a small systematic error in the asymmetry value is present even with perfect statistics. This is due to the fact that the linear slide does not reproduce the channel number counts with sufficient accuracy. The KSSPM removes most of the systematic error.

Tests using computer-simulated spectra

To check the viability of the KSSPM, comprehensive tests were made with computer-simulated data, to test whether the method corrects for systematic drift asymmetries without distorting the true left-right asymmetries in the data. Fig. 4.4 shows data derived from simulated spectra incorporating a built-in true asymmetry (ε = 0.0118) together with different (drift) false asymmetries. Each group of points incorporates a different false asymmetry in the range -0.02 to +0.03. Ten simulations have been run for each group, each simulation having different random

variations to simulate the statistical fluctuations in a typical experimental run.

The small dots show the uncorrected calculated asymmetry plotted against the known asymmetry value (given by the same simulated spectra but without any statistical uncertainty); crosses show the average of these uncorrected asymmetries; and open points show the averages of the corrected asymmetries together with their mean standard deviations. These values were extracted from the spectra after the shift correction, as determined by the KSSPM, had been applied. The fact that the shift corrected asymmetries reproduce the true value (to within the calculated uncertainties) indicates that the procedure works reliably.

Influence of the escape component

In the procedure developed to deduce the spectrum shift correction, an assumption is made concerning the spectrum edge normalisation factors: if the left edge of the B spectrum needs a normalisation factor of $k_1=k$ (see fig. 4.3(i)) to compensate for possible asymmetry differences between the A and B spectra, then it is assumed that the right edge requires a factor of $k_2=1/k$. This assumption does not hold for the real data (see Appendix 4.4) when the spectra have an escape component (fig. 4.5). In this case incorrect shift correction values are determined leading to systematically incorrect asymmetry values. So as to validate the assumption during the data reduction, the escape contribution was estimated and first subtracted from the spectra before the procedure to deduce the shift correction was applied. An outline of the escape component estimate is given later in this chapter.

Other attempts

For the sake of completeness, a brief description of other methods tried but discarded in favour of the KSSPM described above, is documented.

An incremental shift method was developed in which one spectrum, usually the B, is shifted with respect to the other in incremental steps (i.e. effectively re-binning the data). A range of channel numbers making up the A spectrum left edge is chosen to effectively define a window. Similarly a window about the A spectrum right edge is selected. The channel count values of the B spectrum falling within each window as the spectrum is shifted is compared with the A spectrum window count values. Each spectrum edge is then monitored independently using a chi-squared minimising technique to establish the amount of shift existing. Two methods were attempted to account for real asymmetry in the data.

i) For each shift increment, the B spectrum window count total is first normalised to the A spectrum window total before the chi-square value is calculated. This simple asymmetry compensation method works very well using data with no statistical fluctuations, but gets progressively more unreliable as the range of fluctuation increases.

ii) the height (ie. count) adjustment is done in incremental steps for each shift increment. The chi-square values are fitted by a second order polynomial and the value corresponding to the parabolic minimum is calculated. This procedure is repeated for each shift step and the shift value corresponding to the overall minimum χ^2 is the deduced correction required. Again the method is excellent for data

with perfect statistics, but when statistical fluctuations are present the deduced shift becomes unreliable. Problems are probably due to the fact that only the edge is analysed resulting in too few datum points for the method to be sufficiently effective.

In an effort to render the method insensitive to the statistical fluctuations, considerable effort went into developing a suitable spectrum smoothing routine. The most effective procedures were a moving point polynomial method (SA64) and a discrete fast Fourier transform method. Although the introduction of the smoothing improves the situation, there remains a systematic error in the deduced shifts making the entire procedure unsuitable for extracting asymmetry values to the desired accuracy.

4.4 Raw data analysis

Defining the angle bins

In the experimental configuration a side detector was used so that the recoil proton events could be calibrated in terms of the corresponding neutron scattering angle.

The coincidence events of each calibration run were read from the buffer tapes using a SPERRY 1100 computer and stored on hard disc to facilitate rapid data analysis. Each run (corresponding to a particular neutron scattering angle) was processed as follows:-

i) The events were scanned and the coincidence time-of-flight parameter was binned so as to derive a spectrum. This coincidence T.O.F. spectrum was plotted in the form of a 256 channel histogram (fig. 4.6). The spectrum comprised the true coincidence T.O.F.

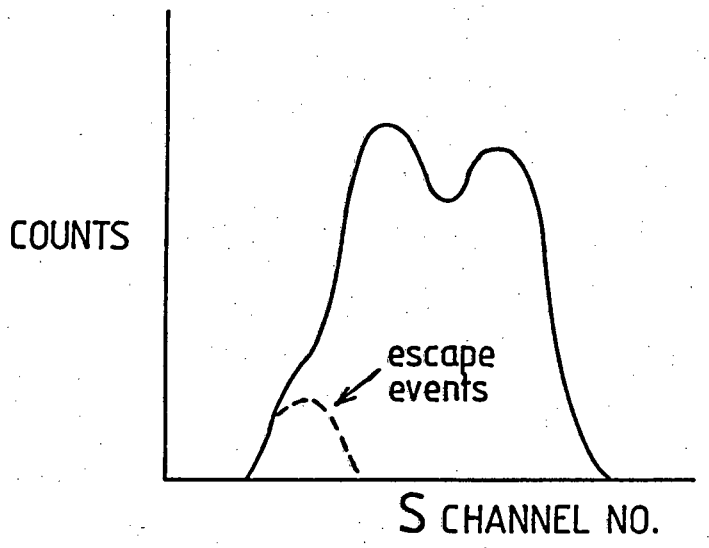

Fig. 4.5 Schematic sketch of an angle bin spectrum for the polarization orientation showing an escape component.

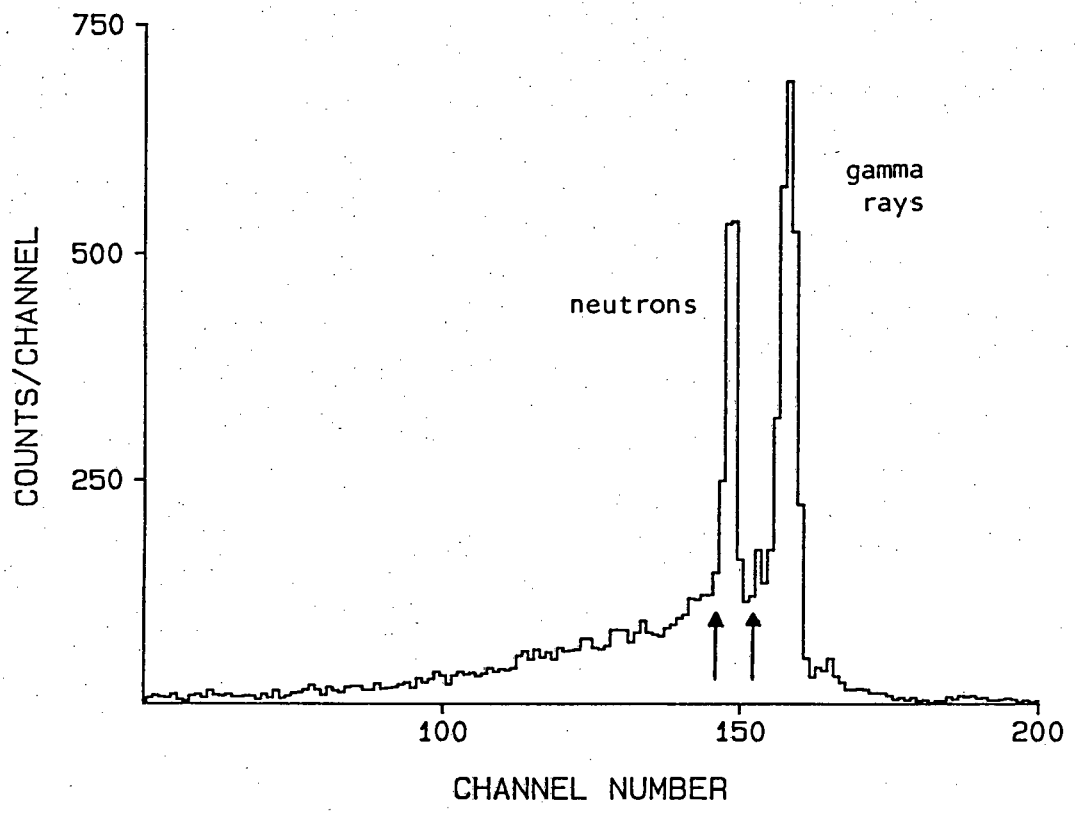

Fig. 4.6 Neutron T.O.F. spectrum for neutrons scattered from the anthracene target and detected by the side detector (in this particular case $\theta_n=50^\circ$ lab angle). The window (indicated by the arrows) was used so that the associated coincidence recoil protons could be selected as explained in the text. The flight path was 45 cm. One channel number approximately equals 1.1 nanoseconds.

peak sitting on a broad background resulting from random coincidence events.

ii) The events were once again scanned but this time only those events which fell within a window set on the T.O.F. peak were selected. In addition, the value of the tagging parameter of each selected event was used to separate the events corresponding to the up and down crystal orientations. The events were stored in a 2-dimensional array (64 x 64 channel matrix) according to the L and S parameter values. A density plot of the combined data (fig. 4.7) shows peaks in the L-S plane indicating those planar proton recoils which were elastically scattered by the detected neutrons. In the one crystal orientation the recoil protons were closer to the c'-axis and hence a peak was obtained at a low S value. In the other orientation the protons were closer to the b-axis and a peak was obtained at a high S value (and the L value was lower than for the corresponding low S peak). A line joining the centroids of these two peaks defined a locus corresponding to those proton recoil events (mostly non-planar) which were associated with the particular neutron scattering angle. Additional measurements indicated that a straight line locus is indeed appropriate. Fig. 4.8(a) indicates a series of coincidence peaks for different neutron scattering angles.

iii) When all of the calibration runs had been processed as explained above, a series of loci defined the scattering angles in the L-S plane (fig. 4.8(b)). The widths of the coincidence peaks suggested that an appropriate angle bin width should be 10° laboratory angle (ie. 20° centre-of-mass). Since there is a spread in the peaks contributed by the resolution of the side detector, the 20° c.m. width is an upper limit.

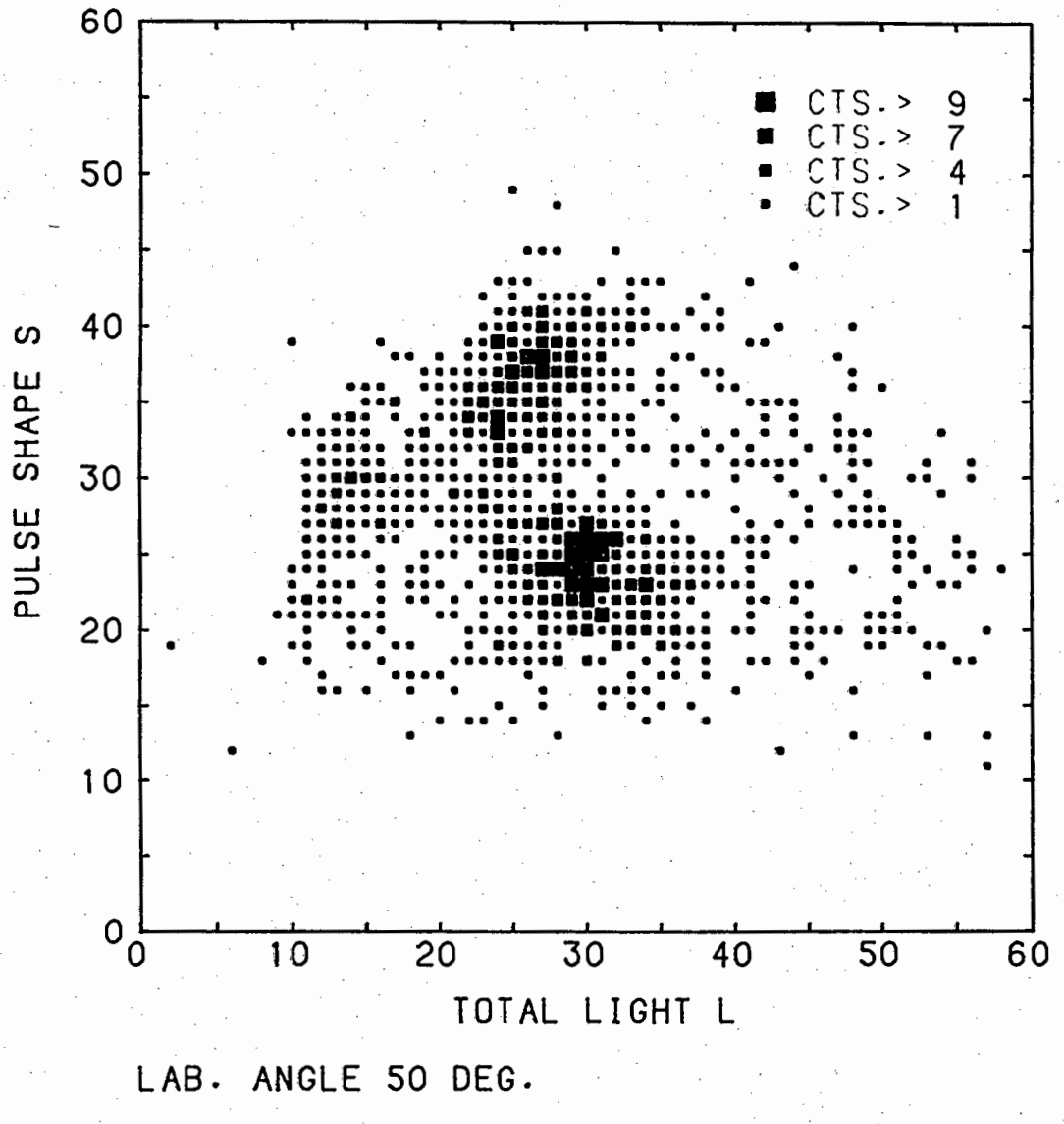

Fig. 4.7 A density plot showing the proton recoil coincidence peaks in the LS plane. The associated scattered neutron laboratory angle was 50°. The z-scale corresponds to the number of counts as indicated.

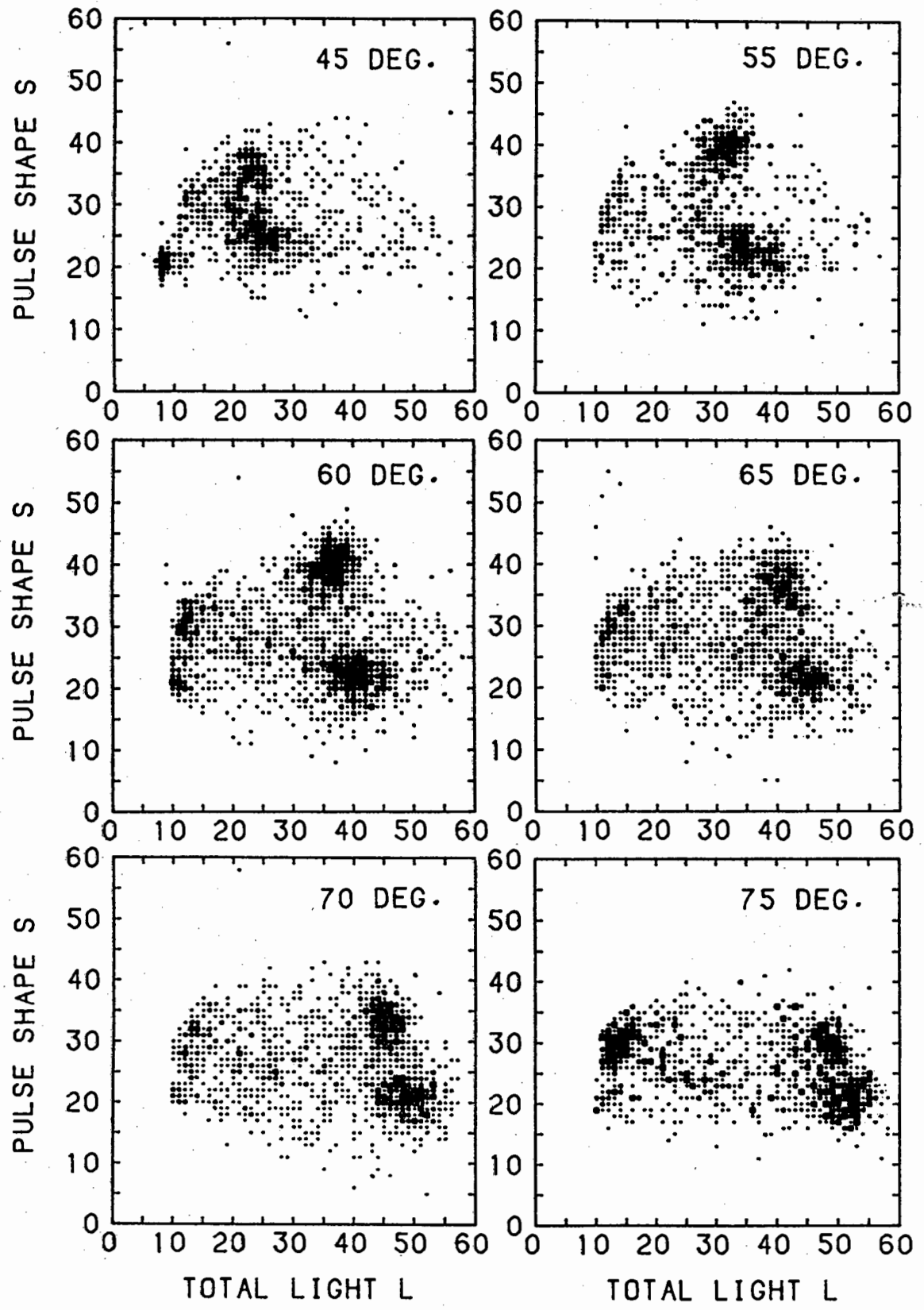

Fig. 4.8(a) A series of density plots showing proton recoil events in coincidence with scattered neutrons at the neutron laboratory angle indicated. The z-scale ranged from between 1 and >10 counts in steps of 3.

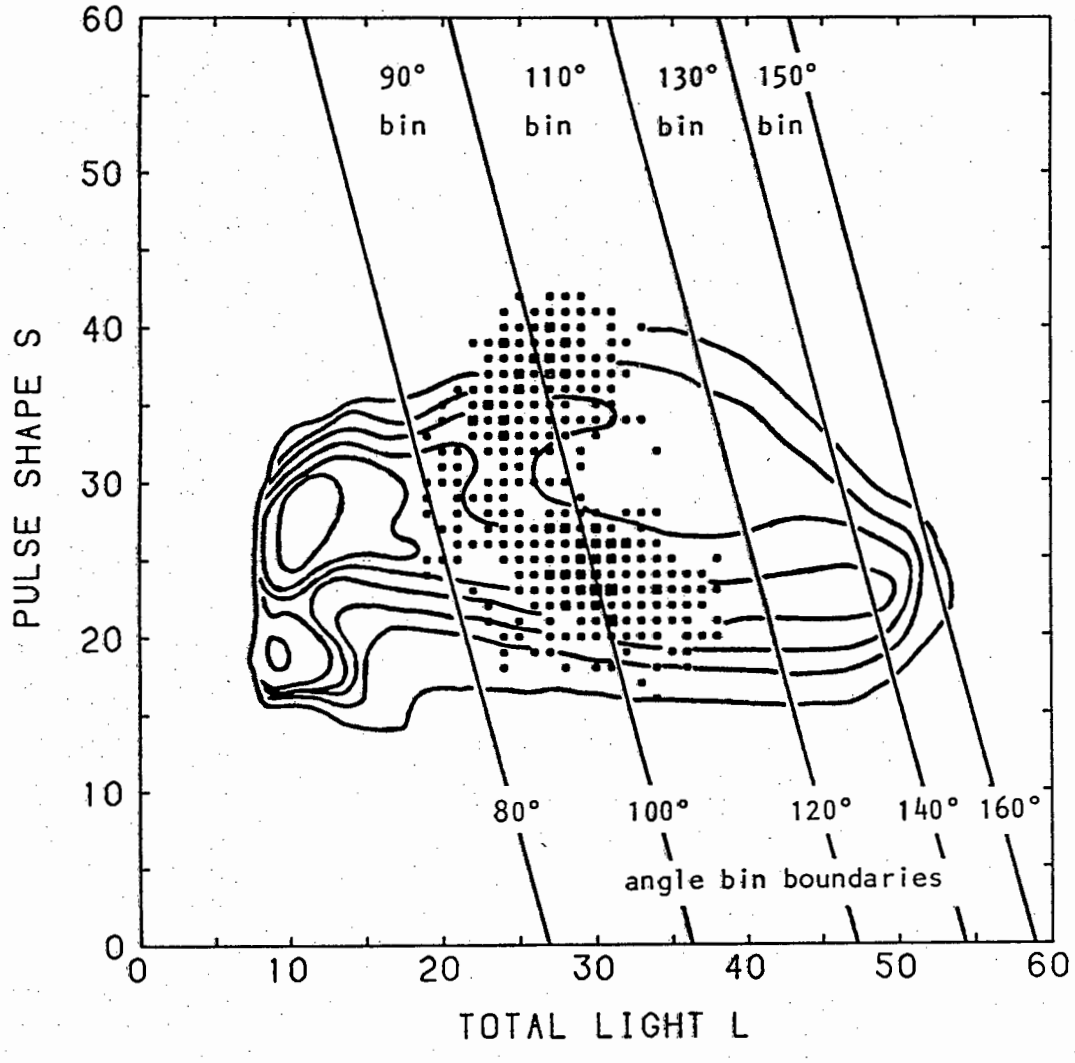

Fig. 4.8(b) Angle bins in the LS plane as defined by the coincidence proton recoil peaks. The associated neutron centre-of-mass scattering angles are shown. The angle bin boundaries are superimposed on a contour plot of an LS singles spectrum and on a density plot of the proton recoil coincidence peak at $\theta_n = 50^\circ$ neutron lab angle (100° c.m.).

Producing angle bin spectra

During the data collection for an asymmetry measurement, several 2400' magnetic tapes of event-by-event data were collected. The processing of each buffer tape separately hence constituted a convenient subset of the total available data. Each tape was processed as follows:-

i) The tape was scanned and each event was sorted according to the value of the tag parameter. The events tagged as pile-ups were rejected. Two L-S matrices (64 x 64 channels each) labelled A and B were accumulated. The sorting of events into the A or B matrix was designed so that the sign of the extracted asymmetry values would be consistent with the Basel convention (see Appendix 4.3). An isometric plot of one of these matrices containing data obtained at the polarization orientation is shown in fig. 4.9.

ii) A projected L spectrum was obtained from each of the matrices to check whether the pulse heights L were properly matched. Where necessary a relative gain correction factor was determined using an incremental method incorporating a minimum χ^2 comparison test. The L axis of one of the matrices was then effectively adjusted so as to correspond with the other.

iii) Using the appropriate angle bin boundaries to define the required angle bins, the L-S spectrum count values lying within the boundaries were projected onto the S axis (or at some angle other than 90° to the S axis where necessary) using the A and B matrices. Fig. 4.10 shows histogram plots of typical angle bin spectra. Because the boundary loci are angled with respect to the L axis, the appropriate fraction of a matrix element count value was used when the boundary cut through it. This was also

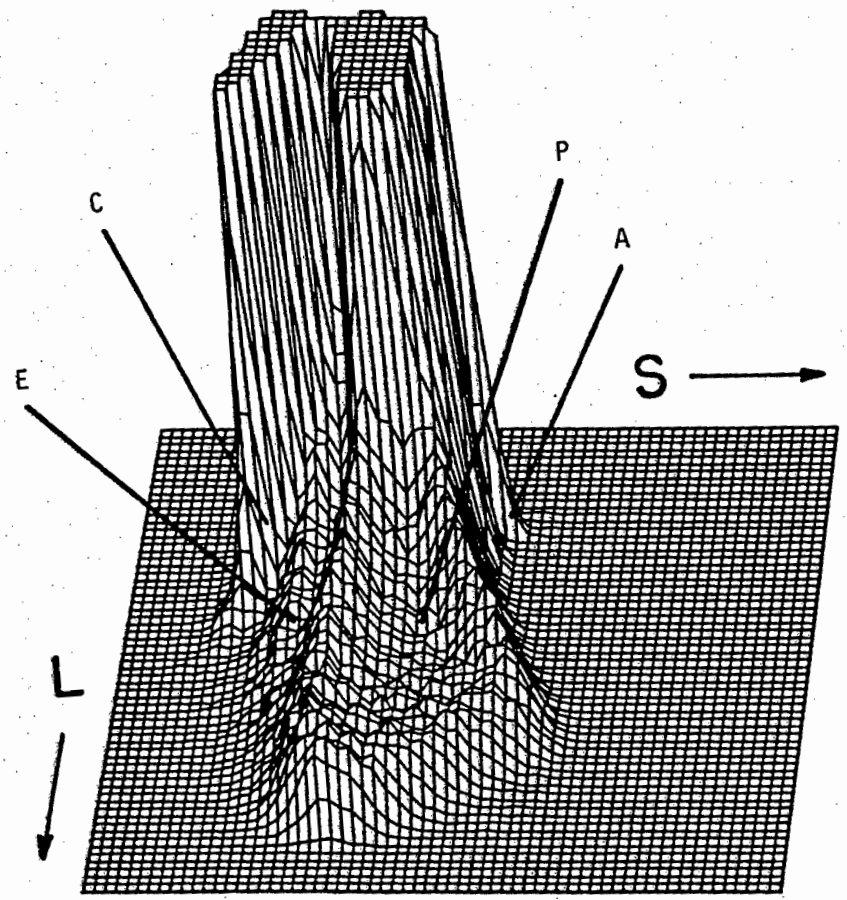

Fig. 4.9 An LS singles spectrum recorded with the anthracene-2 crystal in the polarization orientation. The L threshold is lower here than in fig. 2.3. C indicates Compton electrons, P the recoil protons, E the proton escape ridge and A alpha particles from the $^{12}C(n,\alpha)^{9}Be$ and $^{12}C(n,n')3\alpha$ reactions.

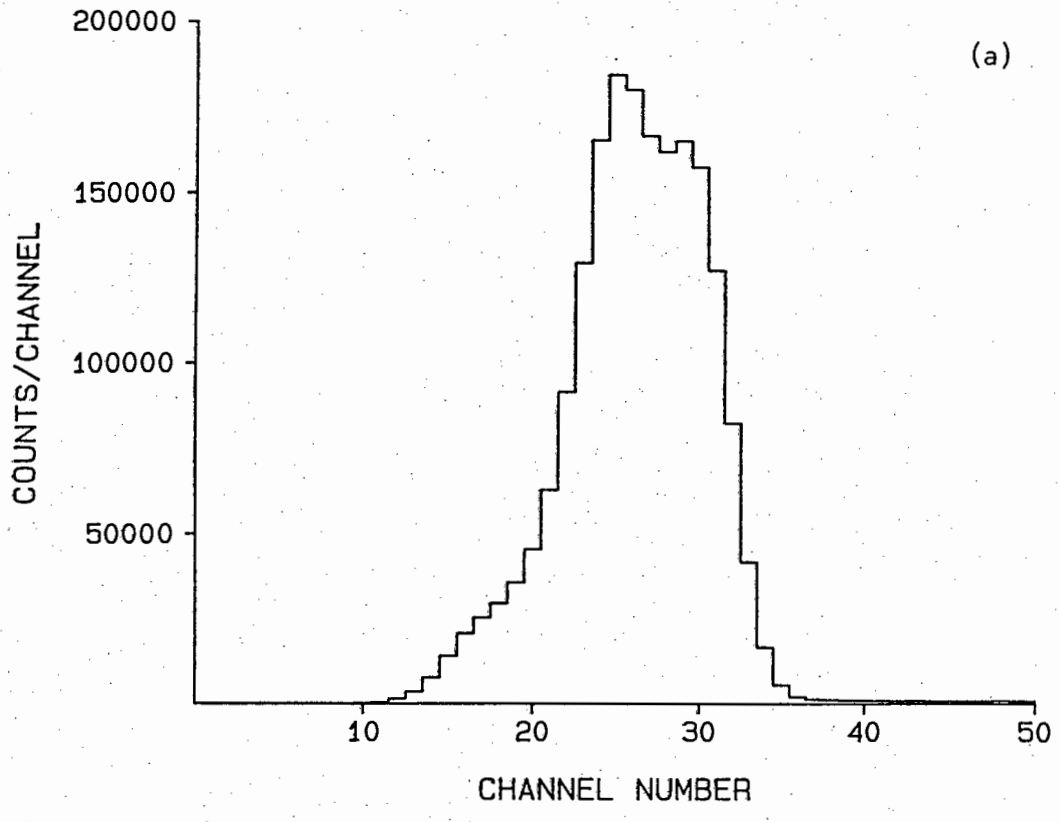

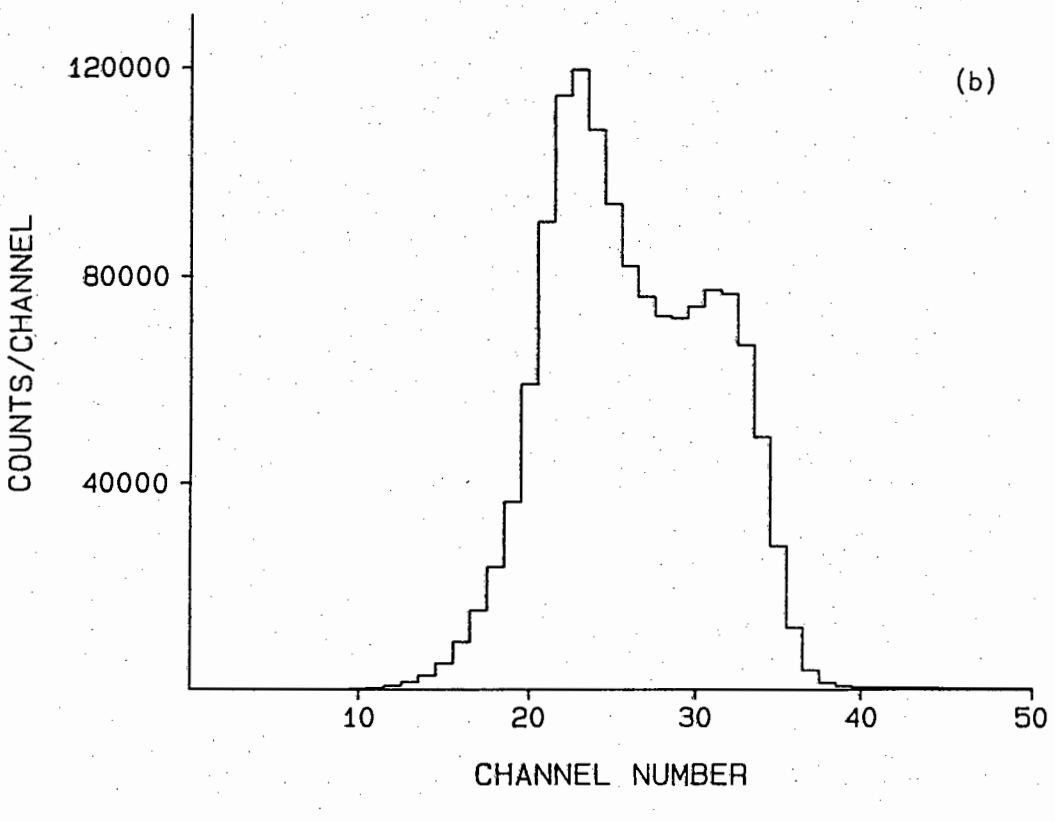

Fig. 4.10 Typical angle bin spectra at the polarization orientation for (a) 90° bin and (b) 110° bin. The proton recoil escape component can clearly be seen on the left edge of the 90° spectrum.

the case when S projections non-perpendicular to the S axis were done. Thus an angle bin spectrum pair for each specified neutron scattering angle was then available for analysis as previously outlined so that the asymmetry value could be determined.

4.5 Estimation of the escape contribution

The estimation of the escape component of the angle bin spectrum has a two-fold purpose.

i) To correct for the diluting effect due to the inclusion of escapes in the total number of events, an estimation of the fraction of escapes making up the spectrum is all that is required. A simple correction can then be applied to the asymmetry value, or equivalently, the number of escape events can be subtracted from the total number of events making up the spectrum before the asymmetry is calculated; and

ii) In order to validate assumptions made in the shift correction procedure, the distribution of the escape component lying under the spectrum needs to be estimated and removed. This is effectively a second order correction which is applied so that the shift correction can be correctly determined. As a result, the overall sensitivity of the analysis is not expected to be as dependent on the escape estimation as it is on the shift correction value. This is fortunate because the true distribution of the escape events lying within the angle bin data is unknown.

By using a c'-axis angle bin spectrum, where the escape events are more clearly separated from the main body of non-escape events (fig. 4.11), a good estimation of the fraction of events escaping can be made. Since the range of the protons is small

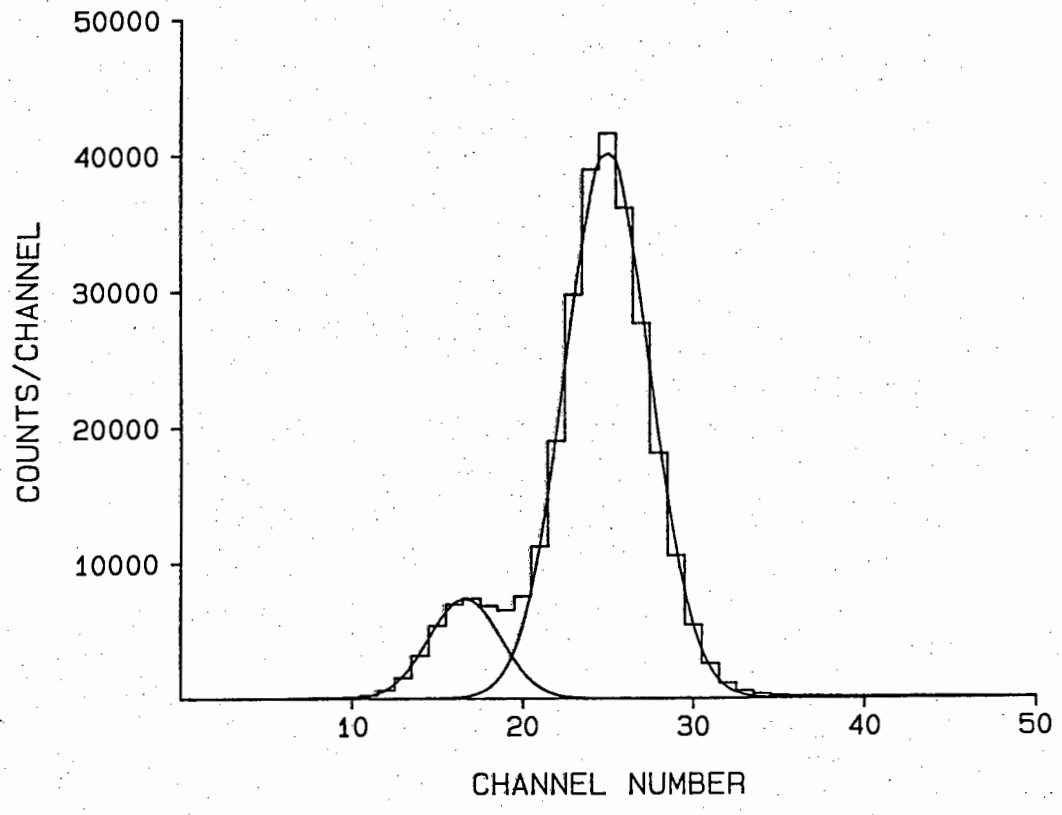

Fig. 4.11 The 90° c.m. angle bin spectrum obtained from the c'-axis crystal orientation showing the clear separation of the escaping and non-escaping proton recoils. The curves are a least squares fit to the data of overlapping Gaussian distributions.

with respect to the dimensions of the crystal, the fraction of escapes is expected to be approximately independent of the orientation of the crystal.

The escape distribution in the polarization orientation angle bin spectra was assumed to be Gaussian in shape, and the protrusion in the left edge of the spectrum (especially for the low neutron scattering angles) aided in the estimation of the position and width of the escape peak. Although the number of escape events contributing to the angle bin spectra decreases as the scattering angle increases, the escape distribution is pulled into the spectrum and is difficult to estimate reliably.

4.6 Polarization and null runs

The polarization runs, which were collected at $\xi=20^{\circ}$, provided the asymmetry data for the P_{np} analyzing power measurements. To monitor and correct for possible systematic false asymmetries remaining after all corrections had been applied during the data reduction process, null runs at $\xi=0^{\circ}$ were also collected. Where the null data indicated an asymmetry inconsistent with zero, this was taken as an indication of the residual false asymmetry. This residual asymmetry was treated as an estimate of the systematic error remaining in the corresponding polarization data collected under the same experimental conditions. The removal of the systematic error was thus the final correction applied to the measured asymmetry.

4.7 Asymmetry uncertainty estimate

A formula for estimating the uncertainty $\Delta\varepsilon$ of a left-right asymmetry measurement ε is derived from first principles in

appendix 4.5. In the present situation the asymmetry ε_P is given by (see section 4.2 and fig. 4.1) :

$$\varepsilon_P = (\pi/4N) \, (N_L - N_R)$$

where $N_L = N_A^{<} + N_B^{>}$ and $N_R = N_A^{>} + N_B^{<}$.

Since $N_R = 2N - N_L$, it follows that $\varepsilon_P = (\pi/2N) \, (N_L - N)$.

From appendix 4.5 the asymmetry $\Delta\varepsilon_P$ is

$$\Delta\varepsilon_P = \pi \, \Delta N_L / 2N ,$$

where $\Delta N_L = [(\Delta N_A^{<})^2 + (\Delta N_B^{>})^2]^{1/2}$ since $N_A^{<}$ and $N_B^{>}$ are independent measurements.

Now, by Bernoulli statistics (see appendix 4.5),

$$\Delta N_A^{<} = (N_A^{<} N_A^{>}/N)^{1/2} = [N_A^{<} (N - N_A^{<})/N]^{1/2}$$

and $$\Delta N_B^{>} = (N_B^{>} N_B^{<}/N)^{1/2} = [N_B^{>} (N - N_B^{>})/N]^{1/2}$$

Hence $$\Delta\varepsilon_P = \pi/2N \{ N_A^{<} (N-N_A^{<})/N + N_B^{>} (N-N_B^{>})/N \}^{1/2} .$$

To test the validity of this formula, an experimental run was divided into six subsets. The asymmetry was calculated from each spectrum subset (no corrections being made for shifts etc.), and the mean and standard deviation of the mean were calculated in the usual way

ie. $$\varepsilon = \frac{\Sigma_i \, \varepsilon_i}{n} \qquad \text{and} \qquad (\Delta\varepsilon)^2 = \frac{\Sigma_i \, (\varepsilon - \varepsilon_i)^2}{n(n-1)}$$

This was then compared with the value calculated from the spectrum comprising the sum of the spectrum subsets using the derived formula. This comparison was done for several scattering angles. As can be seen from table 4.1, the viability of the formula has been demonstrated. It is noted that this formula should be used instead of that given in reference BR74 which underestimates the statistical uncertainty by a large amount.

Table 4.1. An analysis of i) subsets of asymmetry data, and ii) the combined data.

angle	Asymmetry in percent							
	set 1	set 2	set 3	set 4	set 5	set 6	mean of sets	Combined
90°	1.01	1.03	1.48	0.97	1.47	1.01	1.16±0.10	1.17±0.10
105°	0.85	0.50	0.94	1.65	0.79	1.01	0.96±0.16	0.97±0.13
115°	0.97	1.14	1.11	0.76	1.37	0.67	1.00±0.11	1.03±0.14
130°	0.60	0.58	0.77	1.52	1.13	1.03	0.94±0.15	0.91±0.12
150°	0.36	0.38	0.44	0.48	0.33	-0.10	0.31±0.09	0.37±0.16

4.8 Summary of procedures applied in data reduction

A and B angle bin spectra were generated for both the polarization and null runs. The analysis procedures were identical for both types of run. The spectrum component comprising proton recoil escapes was estimated and removed from the spectra. The relative shift between an A and B spectra pair was then determined, and a spectrum shift correction applied when indicated. The asymmetry and the associated uncertainty were then extracted from each spectra pair. The asymmetry value from the polarization run was then corrected for any remaining systematic false asymmetry when the corresponding null run indicated this to be necessary.

CHAPTER 5

RESULTS

The results presented comprise four experimental runs, identified as A,B,C and D, made using two different anthracene crystals. Runs A and B used a cylindrically shaped (radius=1.25cm, length=2.5cm) anthracene crystal (anthracene-2) of volume ~12 cm^3. The other runs C and D used an irregularly shaped crystal (anthracene-1) of volume ~1.5 cm^3. Although anthracene-2 has scintillation characteristics inferior to those of anthracene-1, it was selected in two of the runs because it enabled the desired counting statistics to be obtained in a shorter running period.

In all of the runs, data were collected using neutrons from the $T(d,\vec{n})^4He$ reaction, with E_d=5.00 MeV and neutron angle $\xi=0^o$ or 20^o to the deuteron beam. At $\xi=0^o$, the incident neutron polarization is zero, and so the measured asymmetry is expected to be zero. The data collected at this angle are referred to as the null data. The incident neutron polarization for runs at $\xi=20^o$ was taken as 0.25 based on a Legendre polynomial fit to a number of angular distribution measurements (see SM72) for the T(d,n) reaction at this energy.

Since the incident neutron energy is similar for the null and polarization runs (22 MeV and 21.6 MeV respectively), the conditions for the two types of run were essentially the same, apart from the incident neutron polarization. The null runs were aimed at monitoring residual systematic asymmetries of whatever origin in the polarization runs, not removed by instrumental design or shift corrections etc. They also provided an estimate of the magnitude of these unknown systematic errors.

The criterion used to determine whether residual asymmetries requiring correction were present in the polarization run was based on the statistical uncertainty measured for the associated null asymmetry measurement. If the null asymmetry values showed a statistically significant systematic trend (ie. $|\varepsilon_{null}| \geq \Delta\varepsilon_{null}$), then the null measurement was regarded as an estimate of the systematic error in the polarization asymmetry measurement, ie. the true polarization asymmetry was taken as

$$\varepsilon_{corr} = \varepsilon_{pol} - \varepsilon_{null}$$

where ε_{pol} and ε_{null} are the asymmetries measured in the polarization and null runs respectively. This situation applied to runs A, B and C. Where the null run showed no statistically significant non-zero trend however, as was the case for run D, this correction was ignored and $\varepsilon_{corr}=\varepsilon_{pol}$ was assumed.

The results of the various runs are given in tables 5.1 to 5.4. In all cases except one, the data were analyzed using angle bins of width equivalent to 20° c.m. scattering angle ie. 10° lab scattering angle. In data set A, the 77.5° angle bin has a 5° c.m. width. This was because the experimental pulse height threshold used for this run restricted the lower limit of the angle bin boundary to 75° c.m. The angles listed in the table are the centres of the angle bins used and correspond within ± 0.5° to the associated mean c.m. scattering angles.

The asymmetry values listed are planar asymmetries (ie. including the $\pi/2$ factor) calculated either without any correction or with a spectrum shift correction. Where it was found necessary to account for the interference of the escape events during the shift correction, this was done. P_{np} is the n-p polarization value

Table 5.1. Results of run A.

θ_n		no shift correction	with shift correction
77.5°	ε_{null}	-0.0076 ± 0.0021	-0.0035 ± 0.0021
	ε_{pol}	0.0059 ± 0.0016	0.0109 ± 0.0016
	ε_{corr}	0.0135 ± 0.0016	0.0144 ± 0.0016
	P_{np}	0.0540 ± 0.0065	0.0575 ± 0.0065
90°	ε_{null}	-0.0048 ± 0.0011	0.0002 ± 0.0011
	ε_{pol}	0.0070 ± 0.0009	0.0115 ± 0.0009
	ε_{corr}	0.0118 ± 0.0009	0.0115 ± 0.0009
	P_{np}	0.0472 ± 0.0035	0.0462 ± 0.0035
110°	ε_{null}	-0.0001 ± 0.0013	0.0089 ± 0.0013
	ε_{pol}	0.0082 ± 0.0010	0.0171 ± 0.0010
	ε_{corr}	0.0082 ± 0.0010	0.0082 ± 0.0010
	P_{np}	0.0326 ± 0.0041	0.0330 ± 0.0041
130°	ε_{null}	0.0052 ± 0.0019	0.0138 ± 0.0019
	ε_{pol}	0.0172 ± 0.0012	0.0205 ± 0.0012
	ε_{corr}	0.0120 ± 0.0012	0.0067 ± 0.0012
	P_{np}	0.0483 ± 0.0048	0.0267 ± 0.0048
150°	ε_{null}	0.0111 ± 0.0027	
	ε_{pol}	0.0137 ± 0.0017	
	ε_{corr}	0.0026 ± 0.0017	
	P_{np}	0.0104 ± 0.0068	

Table 5.2. Results of run B.

θ_n		no shift correction	with shift correction
90°	ε_{null}	0.0140 ± 0.0031	0.0069 ± 0.0031
	ε_{pol}	0.0256 ± 0.0028	0.0209 ± 0.0028
	ε_{corr}	0.0116 ± 0.0028	0.0140 ± 0.0028
	P_{np}	0.0464 ± 0.0112	0.0560 ± 0.0112
110°	ε_{null}	0.0305 ± 0.0034	0.0424 ± 0.0034
	ε_{pol}	0.0468 ± 0.0030	0.0609 ± 0.0030
	ε_{corr}	0.0163 ± 0.0030	0.0185 ± 0.0030
	P_{np}	0.0652 ± 0.0120	0.0740 ± 0.0120
130°	ε_{null}	0.0856 ± 0.0039	0.0796 ± 0.0039
	ε_{pol}	0.0955 ± 0.0035	0.0851 ± 0.0035
	ε_{corr}	0.0099 ± 0.0035	0.0055 ± 0.0035
	P_{np}	0.0396 ± 0.0140	0.0220 ± 0.0140
150°	ε_{null}	0.0102 ± 0.0068	
	ε_{pol}	0.0067 ± 0.0066	
	ε_{corr}	-0.0035 ± 0.0066	
	P_{np}	-0.0140 ± 0.0264	

Table 5.3. Results of run C.

θ_n		no shift correction	with shift correction
90°	ε_{null}	-0.0048 ± 0.0036	-0.0119 ± 0.0036
	ε_{pol}	0.0056 ± 0.0023	0.0005 ± 0.0023
	ε_{corr}	0.0104 ± 0.0023	0.0124 ± 0.0023
	P_{np}	0.0416 ± 0.0091	0.0494 ± 0.0091
110°	ε_{null}	-0.0104 ± 0.0042	-0.0163 ± 0.0042
	ε_{pol}	-0.0040 ± 0.0026	-0.0082 ± 0.0026
	ε_{corr}	0.0064 ± 0.0026	0.0081 ± 0.0026
	P_{np}	0.0255 ± 0.0105	0.0324 ± 0.0105
130°	ε_{null}	-0.0422 ± 0.0052	-0.0161 ± 0.0052
	ε_{pol}	-0.0265 ± 0.0033	-0.0052 ± 0.0033
	ε_{corr}	0.0157 ± 0.0033	0.0109 ± 0.0033
	P_{np}	0.0628 ± 0.0131	0.0435 ± 0.0131

Table 5.4. Results of run D.

θ_n		no shift correction	with shift correction
90°	ε_{null}	0.0123 ± 0.0042	0.0138 ± 0.0042
	ε_{pol}	0.0049 ± 0.0041	0.0087 ± 0.0041
	ε_{corr}	0.0049 ± 0.0041	0.0087 ± 0.0041
	P_{np}	0.0195 ± 0.0165	0.0347 ± 0.0165
110°	ε_{null}	-0.0059 ± 0.0051	-0.0045 ± 0.0051
	ε_{pol}	0.0118 ± 0.0056	0.0144 ± 0.0056
	ε_{corr}	0.0118 ± 0.0056	0.0144 ± 0.0056
	P_{np}	0.0471 ± 0.0225	0.0578 ± 0.0225
130°	ε_{null}	0.0053 ± 0.0060	0.0045 ± 0.0060
	ε_{pol}	0.0054 ± 0.0066	0.0048 ± 0.0066
	ε_{corr}	0.0054 ± 0.0066	0.0048 ± 0.0066
	P_{np}	0.0217 ± 0.0264	0.0192 ± 0.0264

Table 5.5. Polarization values (expressed as a percentage) used for calculating the weighted mean.

Data Set	centre-of-mass scattering angle				
	77.5°	90°	110°	130°	150°
A	5.75 ± 0.65	4.62 ± 0.35	3.30 ± 0.41	2.67 ± 0.48	1.04 ± 0.68
B		5.60 ± 1.12	7.40 ± 1.20	2.20 ± 1.40	-1.40 ± 2.64
C		4.94 ± 0.91	3.24 ± 1.05	4.35 ± 1.31	
D		3.47 ± 1.65	5.78 ± 2.25	1.92 ± 2.64	
mean P_{np}	5.75 ± 0.65	4.69 ± 0.31	3.72 ± 0.36	2.78 ± 0.42	0.89 ± 0.66

and is given by $\varepsilon_{corr}/0.25$. In all of the tables, the uncertainties reported are statistical only.

In all cases, the asymmetry values extracted using the shift procedure were considered more reliable, and the associated polarization values were carried forward to table 5.5.

The set A asymmetry values extracted without applying a spectrum shift correction, are shown plotted as a function of θ_n in fig. 5.1a. These can be compared (fig. 5.2a) with the values obtained when a spectrum shift correction was applied. It can be seen that there is a significant null asymmetry of $\leq 1\%$ even after the shift correction. The cause of this residual asymmetry is unknown. If there were no residual systematic error, then the null asymmetry values would form an envelope (enclosing the data points and error bars) parallel to and consistent with the abscissa. As can be seen, the null asymmetry values instead show a systematic trend (approximately linear) with respect to θ_n. This tilt of the envelope away from the horizontal is an indication, then, of the residual systematic error, and provides an estimate of the correction to be applied to the ε_{pol} values. An estimate of the mean width of the envelope gives the uncertainty in the systematic correction. For set A, the systematic uncertainty in the final asymmetry values is thus 0.00085. This implies that the systematic uncertainty in the polarization values for run A is 0.0034.

It is also noted that the <u>net</u> effect of the shift corrections on the final asymmetry values is small (figs. 5.1b and 5.2b). It was found that the shift correction could not be reliably estimated for the $\theta_{n=150^\circ}$ angle bin data. This was due to a combination of poorer statistics and the fact that the data lie close to the L pulse height edge.

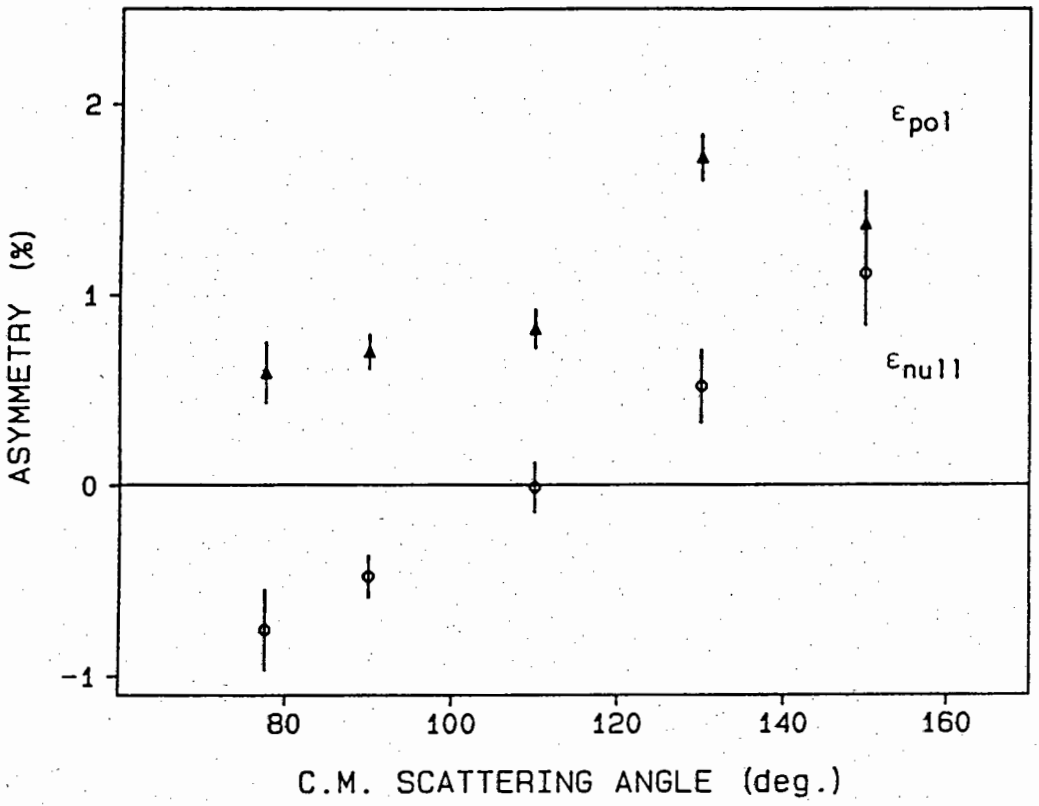

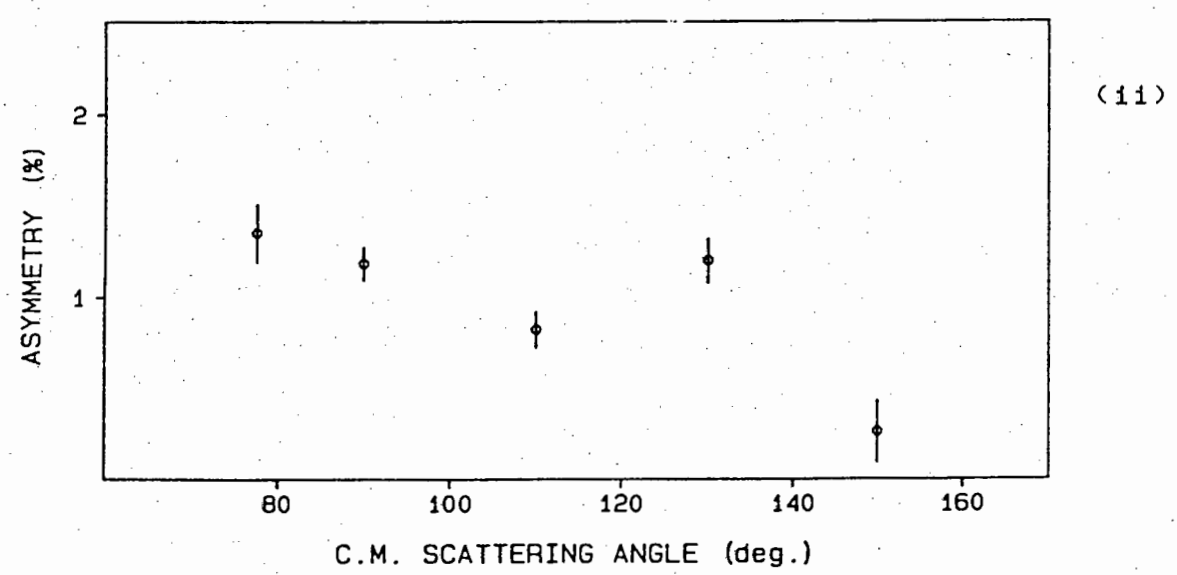

Fig. 5.1 The uncorrected asymmetry values for run A, showing (i) ε_{pol} and ε_{null} asymmetries as a function of θ_n c.m.; and (ii) ε_{corr} asymmetry as a function of θ_n c.m.

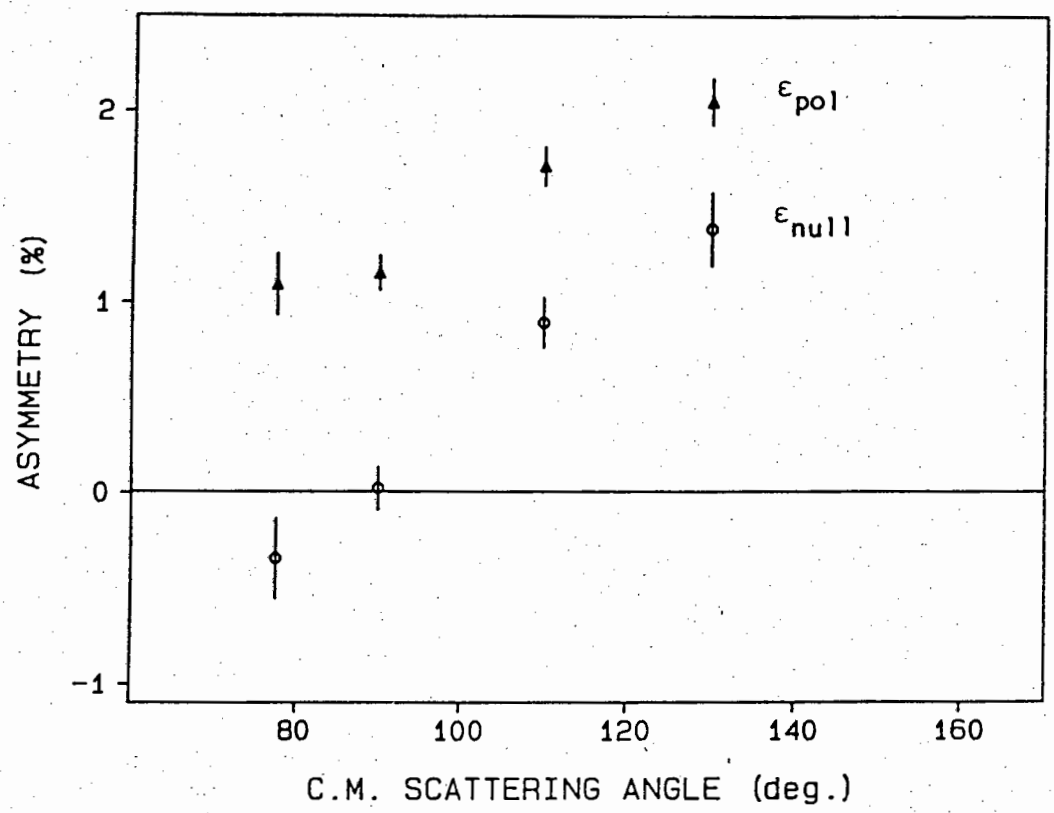

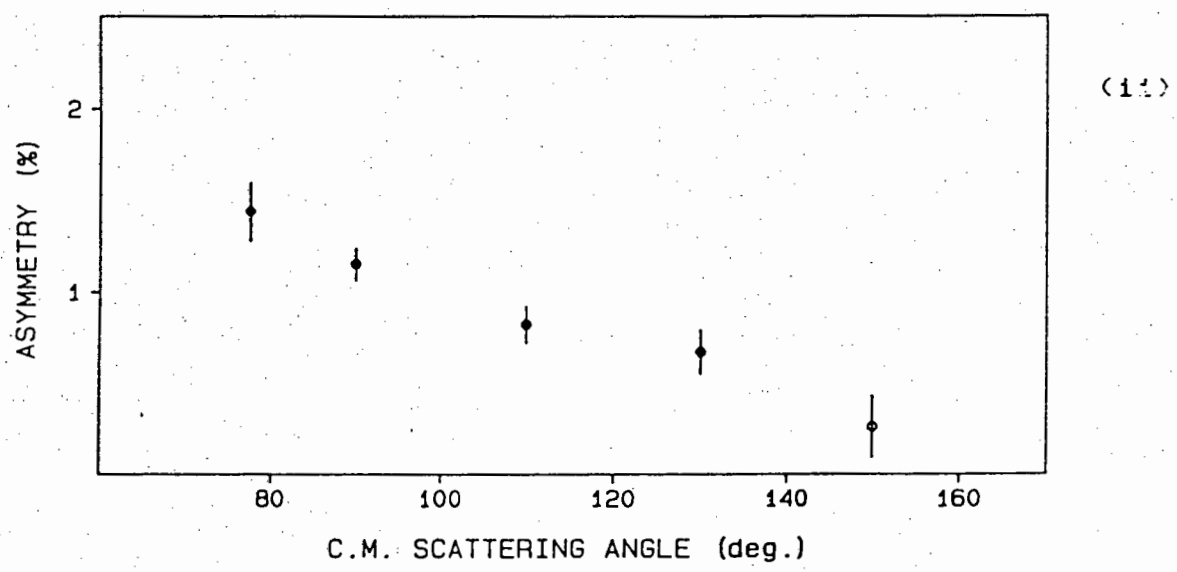

Fig. 5.2 The corrected asymmetry values for run A, showing (i) ε_{pol} and ε_{null} asymmetries as a function of θ_n c.m.; and (ii) ε_{corr} asymmetry as a function of θ_n c.m. The open point is the uncorrected ε_{corr} value.

The final polarization values obtained from each data set are summarised in table 5.5 and in fig. 5.3. The individual values for each scattering angle were weighted by the inverse square of the statistical error to obtain the average. The dominance of set A in the mean, because of the much smaller uncertainties, is evident. Nevertheless, the internal consistency between the sets can be clearly seen (fig. 5.3). This consistency lends confidence to the method of using the null measurements to estimate corrections to the asymmetry data. It can be seen that the asymmetry values measured for a given θ_n, which differ between sets, sometimes by large amounts, agree after this correction has been applied.

A plot of the final polarization values is given in fig. 5.4. Since set A dominates the mean P_{np} values presented in table 5.5, the systematic uncertainty (due to the null correction) associated with these mean values may be taken to be the same as those for set A. The uncertainty in the incident neutron polarization is estimated as ± 0.01. The systematic error due to this uncertainty in the incident polarization is estimated as being negligible by comparison with that introduced by the null correction. The final results of the present P_{np} measurements are thus presented in table 5.6. The total uncertainty includes the statistical and the systematic uncertainties combined in quadrature. This gives an indication of the overall error with the scale error folded in with the statistical error.

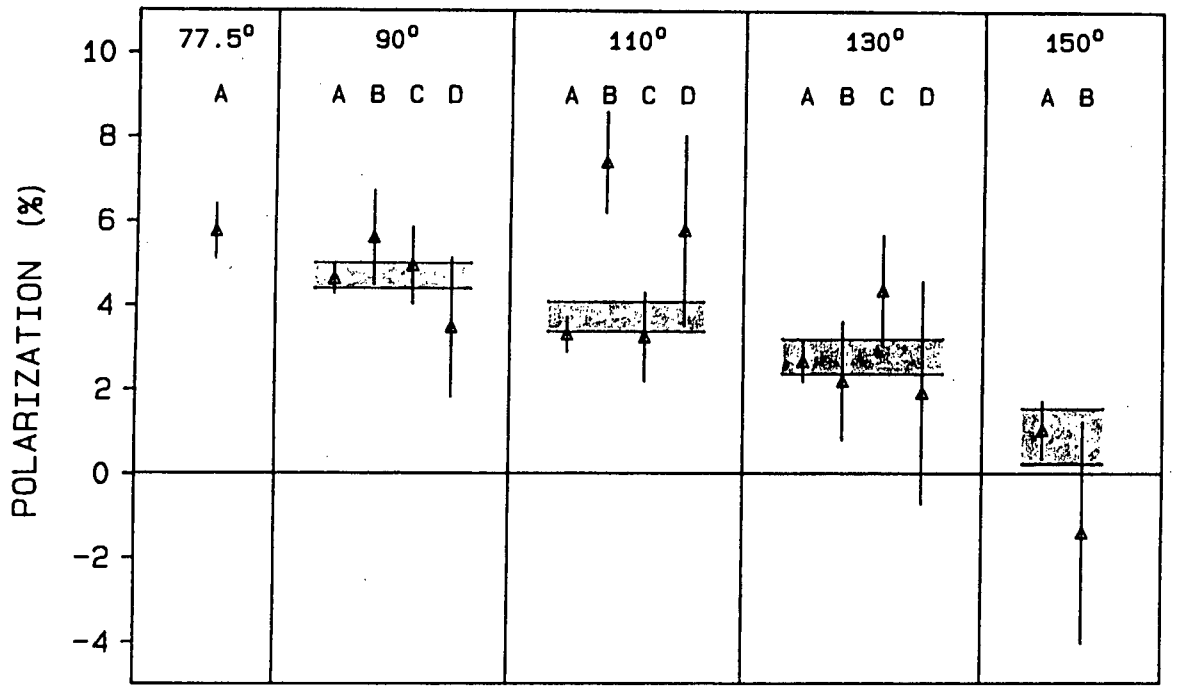

Fig. 5.3 A plot of P_{np} in percentage for the four data sets. The shaded areas represent the weighted mean values (± one std. dev.) for each c.m. scattering angle.

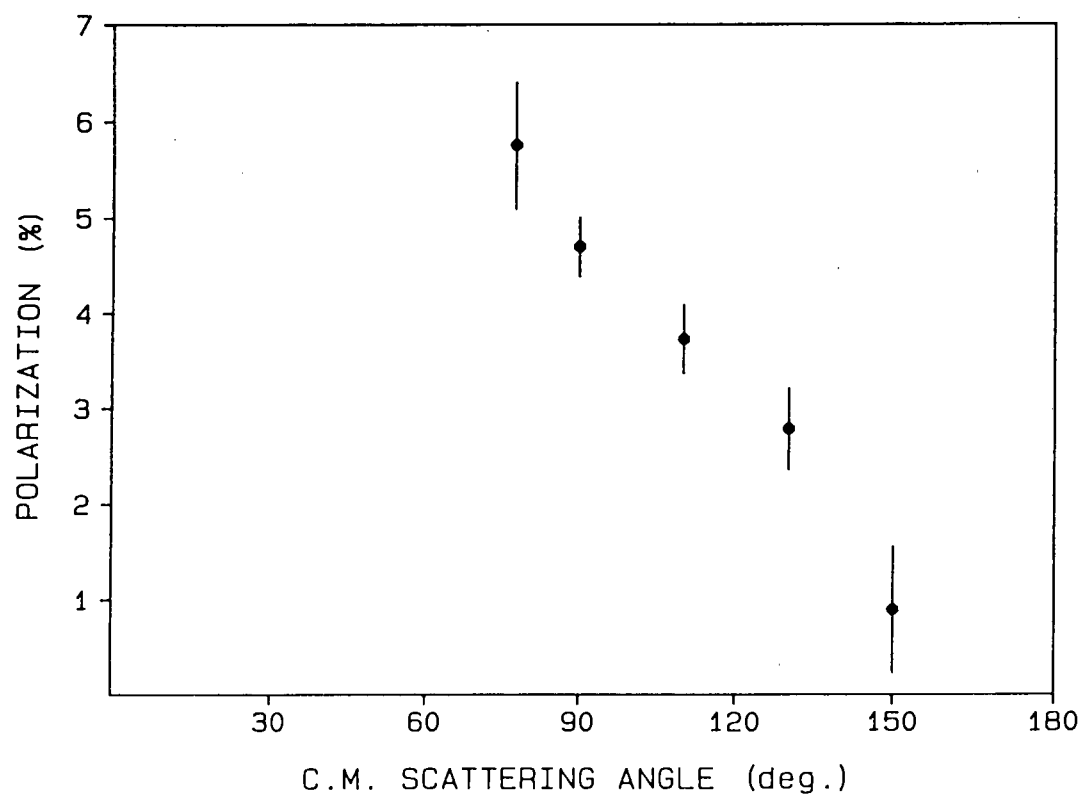

Fig. 5.4 A plot of the present n-p polarization data at E_n=21.6 MeV. The uncertainties shown are statistical only.

Table 5.6. The present P_{np} results (in %).

θ_n (c.m.)	P_{np}	(absolute) uncertainties statistical	systematic	total
77.5°	5.75	0.65	0.34	0.73
90°	4.69	0.31	0.34	0.46
110°	3.72	0.36	0.34	0.50
130°	2.78	0.42	0.34	0.54
150°	0.89	0.66	0.34	0.74

CHAPTER 6

DISCUSSION AND CONCLUSION

6.1 Introduction

The polarization data from this experiment (fig. 5.4 and table 5.6) may be compared with other measurements at the same or nearby energies, with predictions based on phase shift analyses and with predictions based on N-N potentials such as the Paris potential. To facilitate such comparisons it is convenient to parameterize the experimental and the theoretical and phase predictions in a form suggested by Mutchler and Simmons (MU71).

As shown by Mutchler and Simmons, for orbital angular momenta up to $L_{max} = 2$, the polarization data in n-p scattering combined with the differential cross section data can be fitted with the function

$$p(\theta)\sigma(\theta) = \sin\theta\,(A + B\cos\theta)\ . \qquad (6.1)$$

Here θ is the c.m. scattering angle. The cross section can be approximated by using the expression (GA63)

$$\sigma(\theta) = (\sigma_T/4\pi)(1 + b\cos^2\theta)\ /\ (1 + b/3)\ , \qquad (6.2)$$

where $b=2(E_n/90)^2$. Here σ_T is the total n-p scattering cross section, which can be obtained from Gammel's formula (GA63). E_n is the laboratory neutron energy in MeV.

The parameters A and B are related to the phase parameters Δ^{ℓ}_{LS} representing combinations of triplet ℓ-wave phase shifts arising from the spin-orbit part of the nucleon-nucleon interaction. Approximations for the Δ^{ℓ}_{LS} are derived from expressions given by Chisholm et al. (CH80), where it is assumed

that the phase shifts for $L \geq 1$ are small, and the ε_1 mixing parameter is zero:

$$\Delta^P_{LS} = 4k^2A/12\sin^2(^3S_1) \text{ , and}$$
$$\Delta^D_{LS} = 4k^2B/60\sin^2(^3S_1) \qquad (6.3)$$

where k is the centre of mass wave number of the incident neutron. The magnitude of the polarization depends on the spin-orbit splitting Δ^P_{LS} of the T=1 triplet P-waves, whereas the shape relates to the spin-orbit splitting Δ^D_{LS} of the T=0 triplet D-waves.

6.2 The P_{np} measurements

A least squares fit of eq. (6.1) was made to the present experimental data using the matrix approach (DR66). The value used for σ_T at E_n=21.6 MeV was 0.447 barns. The values obtained from the fit for the parameters A and B are given in table 6.1. The curve drawn in fig. 6.1 indicates the fit to the present data.

Table 6.1 also includes the results of similar fits to the corrected MO74 and JO74 data, as well as to the 22 MeV Karlsruhe (WI84) data. There is good agreement in both the A and B values for the present, JO74 and Karlsruhe data. There is, however, disagreement between the values obtained from the corrected MO74 data, both in terms of magnitude and shape.

The present polarization data are also compared with the above mentioned measurements in fig. 6.2. The curve representing a fit to all of the data points is also shown.

6.3 Phase analyses and potential predictions

The polarization data are also compared in fig. 6.2 with some recent phase analysis and potential predictions. The curves represent

Table 6.1. Comparison of A and B from fits to various data sets and phase shift predictions.

	energy(MeV)		A (fm^2)	B (fm^2)
Present	21.6		0.1663 ± 0.0070	0.0782 ± 0.0212
JO74 corrected	21.6		0.1578 ± 0.0037	0.1096 ± 0.0089
MO74 corrected	21.1		0.1953 ± 0.0071	0.1696 ± 0.0135
Karlsruhe	22±1.5		0.1699 ± 0.007	0.0990 ± 0.0128
Combined [1]	21.6 used		0.1686 ± 0.0037	0.0978 ± 0.0081
Combined [2]	21.6 used		0.1752 ± 0.0045	0.1167 ± 0.0096
Paris potential [3]	21.6		0.1555	0.1064
Arndt 1983 [4]	21.6		0.1469	0.0717
LRL-X [5]	21.1		0.156	0.06
Yale-IV [5]	21.1	n-p	0.158	0.13
		p-p	0.144	

1) present, JO74 and Karlsruhe

2) present, JO74 , Karlsruhe and MO74

3) A and B are calculated directly from the phase shifts using the spin-orbit combinations:

$\Delta^{P}_{LS} = (1/12)(-2\ {}^3P_0 - 3\ {}^3P_1 + 5\ {}^3P_2)$ and

$\Delta^{D}_{LS} = (1/60)(-9\ {}^3D_1 - 5\ {}^3D_2 + 14\ {}^3D_3)$.

4) from a fit to the n-p polarization predictions. Hence this is just an approximation.

5) these values are taken from the paper by Morris et al. (MO74)

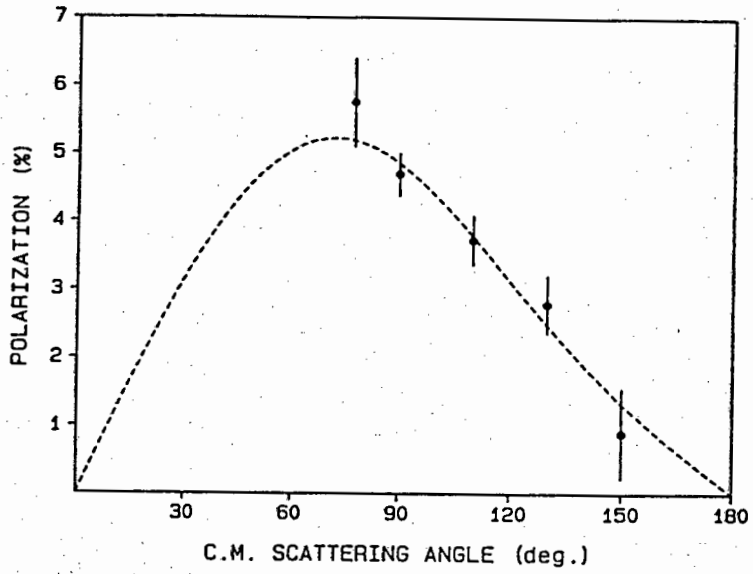

Fig. 6.1 A least squares fit to the present data of the form $p(\theta)\sigma(\theta) = \sin\theta(A + B\cos\theta)$ (see text).

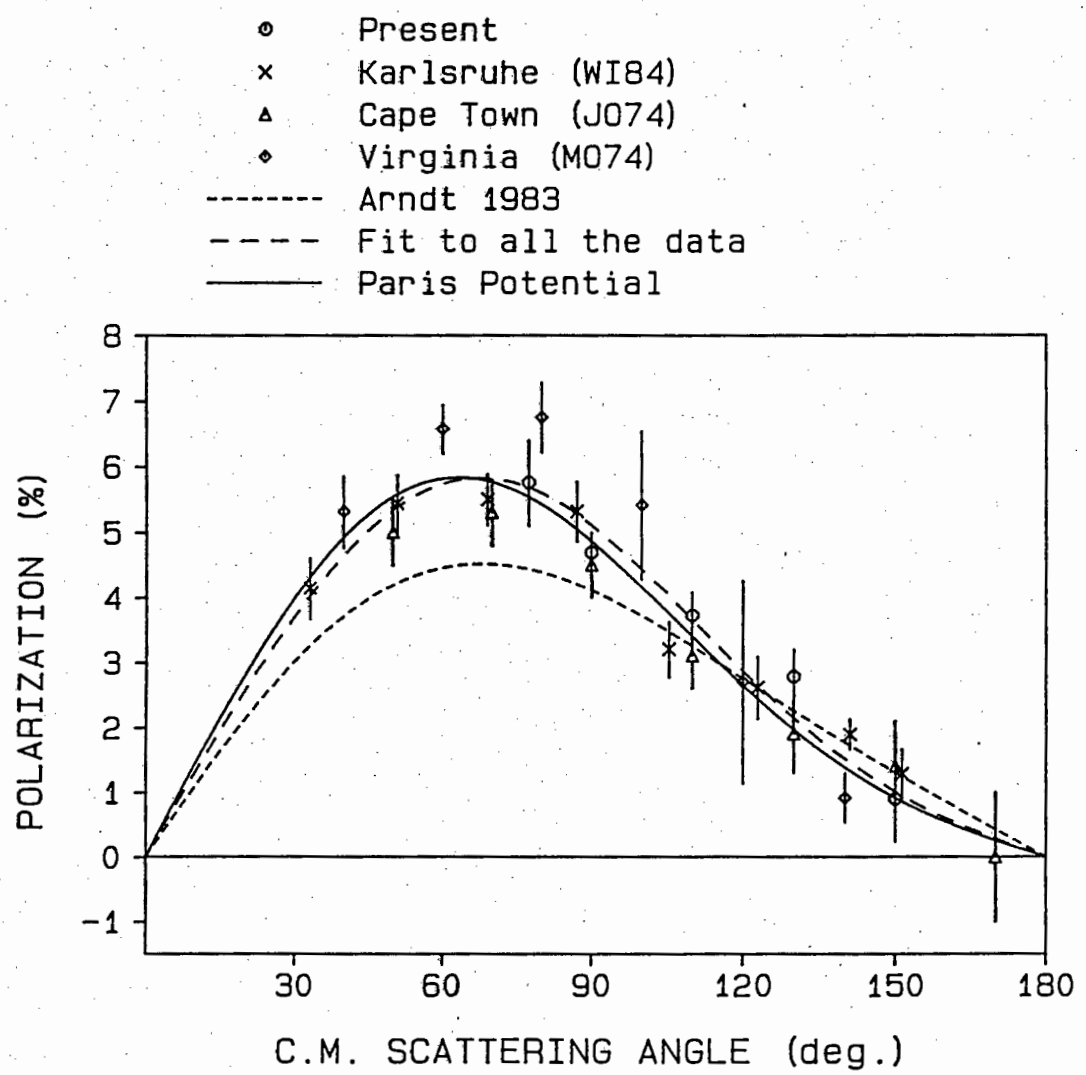

Fig. 6.2 The most recent n-p polarization values in the vicinity of E_n=21.6 MeV.

i) the polarization observable at 21.6 MeV as predicted by the energy dependent nucleon-nucleon partial-wave analysis of Arndt et al. (AR83). The calculation was made using phase shifts corresponding to 21.6 MeV which were estimated by interpolating between the published n-p phase shifts at nearby energies (see table 6.2); and

ii) the polarization values at 21.6 MeV as predicted by the Paris potential. The phase shift parameters (MI86) which were used in this calculation are listed in table 6.2.

Values of the parameters A and B in eq. (6.1) were obtained for the predictions represented by curves (i) and(ii). In the case of (i), the Arndt phase predictions, the curve was fitted to eq. (6.1) in the same way as for the experimental data. For curve (ii), the Paris potential prediction, phase shifts at exactly 21.6 MeV were available and so A and B were calculated directly from these. The A and B values that were determined for (i) and (ii) are shown in table 6.1. The values of A and particularly B derived from the combined data show good agreement with those of the Paris potential, but disagree with the values given by the global phase shifts of Arndt 1983. For completeness, values from the earlier global phase shifts Yale-IV (SE68) and LRL-X (MA69) as given in the paper by Morris et al. (MO74) are also tabulated.

The Bohannon single energy analysis at 25 MeV is probably in need of review owing to the inclusion of the uncorrected MO74 and JO74 data. This conclusion is substantiated by comparing the subsequent Karlsruhe (WI84) and Wisconsin (SR86) n-p polarization measurements at 25 MeV with the values predicted by the Bohannon phase shift parameters (see fig. 6.3). It can be seen that there

is disagreement, particularly in the shape of the polarization distribution.

Table 6.2. Phase shifts (in degrees).

phase shifts	Arndt et al.	Arndt et al.	Paris potential
	20.0 MeV	25.0 MeV	21.6 MeV
$^1S_0$	52.90	50.30	50.15
$^1D_2$	0.56	0.76	0.64
$^3P_0$	8.18	9.61	8.36
$^3P_1$	-4.49	-5.38	-4.68
$^3P_2$	2.00	2.66	2.41
$^1P_1$	-3.23	-3.66	-6.40
$^3S_1$	86.92	81.68	83.99
ε_1	1.07	0.95	1.62
$^3D_1$	-1.67	-2.33	-2.42
$^3D_2$	2.79	3.82	3.20
$^3D_3$	0.13	0.20	0.045

6.4 The anthracene polarimeter

It has been shown that the anthracene scintillation polarimeter is capable of measuring n-p analyzing powers reliably. The statistical accuracy of a measurement has been clarified, and the main sources of systematic error have been identified. These have been eliminated as far as possible both by means of improved instrumental design and in more critical data reduction techniques. The new correction procedure for deducing spectrum shifts has proven its effectiveness.

In the present experiment the null asymmetry measurements showed a residual asymmetry of $\leq$ 1%. The origin of this residual

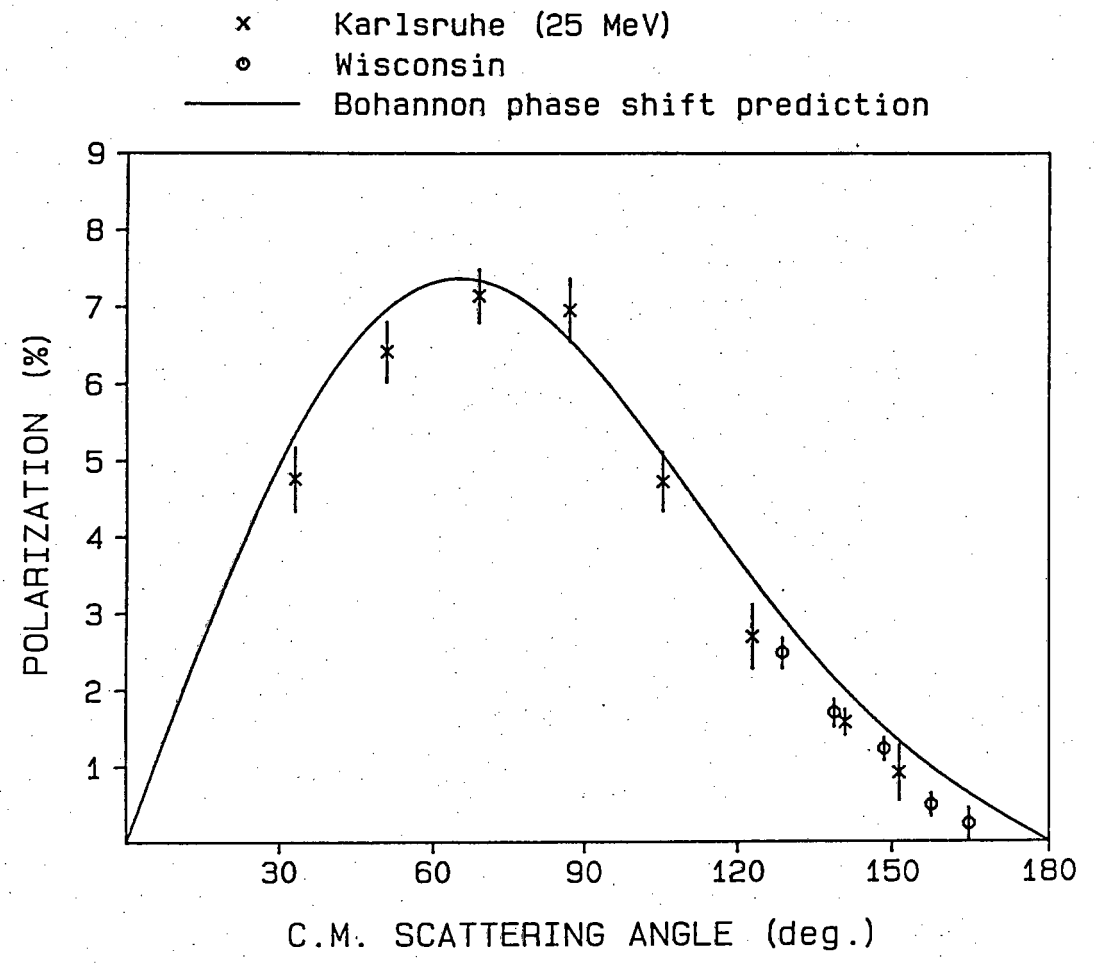

Fig. 6.3 Recent n-p polarization values at 25 MeV compared with the Bohannon phase shift prediction. References are : Karlsruhe(WI84), Wisconsin(SR86) and Bohannon(BO76).

asymmetry is unknown. A possible cause could be that the proton recoil escape component is different for the "up" and "down" crystal orientations. While this residual asymmetry has proved a severe limitation in this experiment, it would be less so if (a) the incident polarization P_o were larger, as obtained for example at most other laboratories where this kind of work is done; and/or
(b) the polarimeter was used at higher energies where P_{np} is larger.

In view of these considerations it may thus be seen that the new anthracene polarimeter developed for this work is a significant improvement over its predecessor (BR74).

6.5 Further developments and applications

The present achievements suggest further applications of the anthracene polarimeter. Some possible applications and further developments are outlined below.

i) If the crystal polarimeter were used at a facility with beam spin-reversal, no relative change in the A and B spectra should be evident due to the fact that the crystal will not need to be rotated. Hence the need for the determination of a spectrum shift correction should not arise, and hence the main source of systematic uncertainty in the measurements will be eliminated. The analysis will be straightforward, and reliable analyzing power measurements with excellent statistics (between 0.1% and 0.2%) should be possible. The same should apply to n-d measurements using a deuterated anthracene crystal.

ii) The crystal scintillation polarimeter can also be used in reverse as an analyzer to determine the polarization of a neutron

beam. In this application n-p phase-shifts can be used to calculate the n-p polarization values $P_{np}(\theta)$ at the beam energy being used. The polarization of the neutron beam is then given by $P=\varepsilon(\theta)/P_{np}(\theta)$, where $\varepsilon(\theta)$ is the measured asymmetry at scattering angle θ. The anthracene analyzer measures the asymmetry for a range of scattering angles simultaneously. Naturally the accuracy of the beam polarization measurement will be limited by the accuracy to which the phase shift parameters at the energy of interest are known. This use of the polarimeter is envisaged for various medium energy (up to 200 MeV) experiments at the new NAC facility.

To demonstrate the analyzer in operation, a run was carried out under slightly different conditions from those of the n-p polarization experiments. The $T(d,\vec{n})^4He$ reaction was again used and a deuteron energy of 5.6 MeV was selected. This energy was considered to be of interest because it has been noted by Mutchler et al. (MU71b) that the ^5He compound system has a broad level at 20-MeV excitation (LA66) that occurs at E_d=5.62 MeV. They have suggested that the level structure of ^5He may affect the polarization observable.

The measurements were made using the anthracene-2 crystal and included null runs at $\xi=0^o$ (E_d=5.0 MeV) and polarization runs at $\xi=25^o$ (E_d=5.6 MeV). The neutron energy in both cases was 22 MeV.

The results of the asymmetry measurements and the subsequent analysis are given in appendix 6.1. The calculation gives P_{inc} = 0.110 ± 0.015 . Fig. 6.4 shows this value together with previous measurements made at a nearby neutron reaction angle ($\xi=30^o$). The present result indicates that a depolarization resonance occurs at E_d=5.6 MeV. It is hard to say whether the earlier measurements

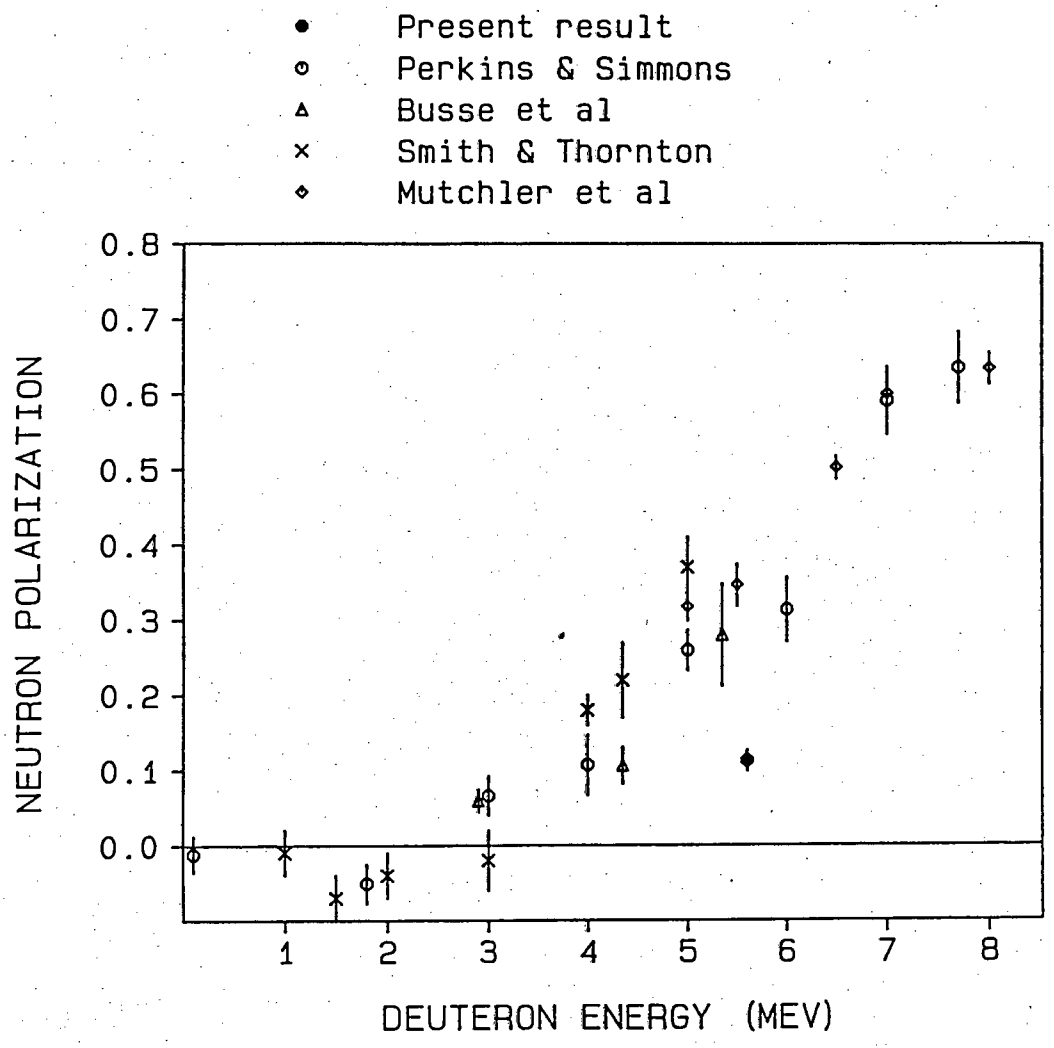

Fig. 6.4 Neutron polarization values from the $T(d,n)^4He$ reaction at reaction angle $\xi=30^o$. The present measurement was made at $\xi=25^o$ and $E_d=5.6$ MeV. The data are from Perkins & Simmons(PE61), Busse et al(BU67), Smith and Thornton(SM72) and Mutchler et al(MU71b).

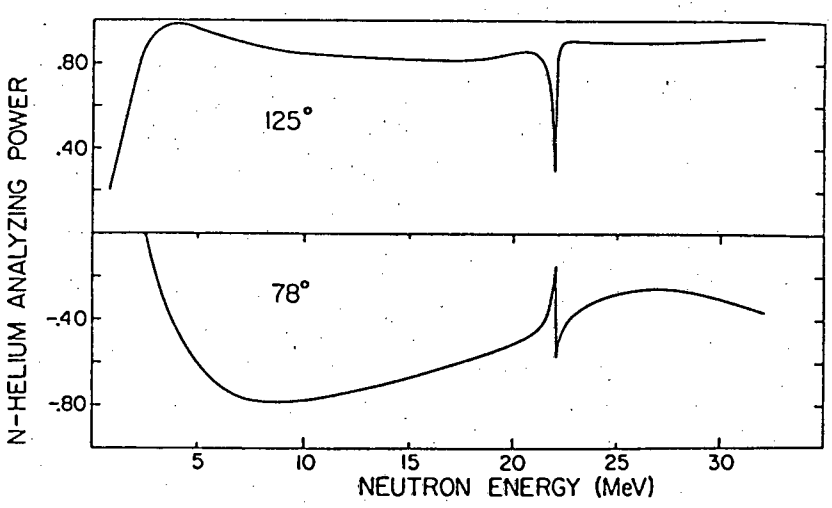

Fig. 6.5 Analyzing power for n-He elastic scattering at angles usually used in a helium neutron polarimeter. Figure from RA81.

near this energy were being affected by the resonance, bearing in mind that there may be an averaging effect due to finite energy resolution of the deuteron beam. Also, the measurements of the T(d,$\vec{n}$) polarization between E_d= 5 MeV and E_d= 6 MeV, where the neutron energy is close to 22 MeV, may not be too reliable. This is because the neutron polarization was measured using a helium neutron polarimeter and depends on n-α scattering phase shifts. As can be seen in fig. 6.5, the reliability of the n-He analyzing powers near 22 MeV, which are obtained from a knowledge of the phase shifts, is reduced owing to resonances in the ^{5}He system. This depolarization effect could be investigated in more detail by measuring the neutron polarization between E_d=5 MeV and E_d=6 MeV using small energy increments. It is interesting to note that measurements at neutron reaction angles ξ=90° and ξ=120° (see fig. 6.6) also indicate strong fluctuation in $P_n(\theta)$ in the vicinity of E_d=5.6 MeV.

iii) A further attractive extension would be to utilise a polarimeter consisting of a thin wafer-like anthracene crystal. Then mainly planar recoils will be recorded, since a large portion of out-of-plane recoils will escape fom the crystal and fall within the escape ridge of the LS spectrum. This should result in the left and right planar events in the LS plane being well separated from each other. The analysis procedure will thus be less sensitive to spectrum shifts, although this advantage will be off-set by a considerably reduced count rate during data collection. If the increased number of escape events poses a problem, they can be even more positively removed, for example, by coupling plastic scintillators to the anthracene crystal. This "phoswhich" system should effectively separate many of the escape

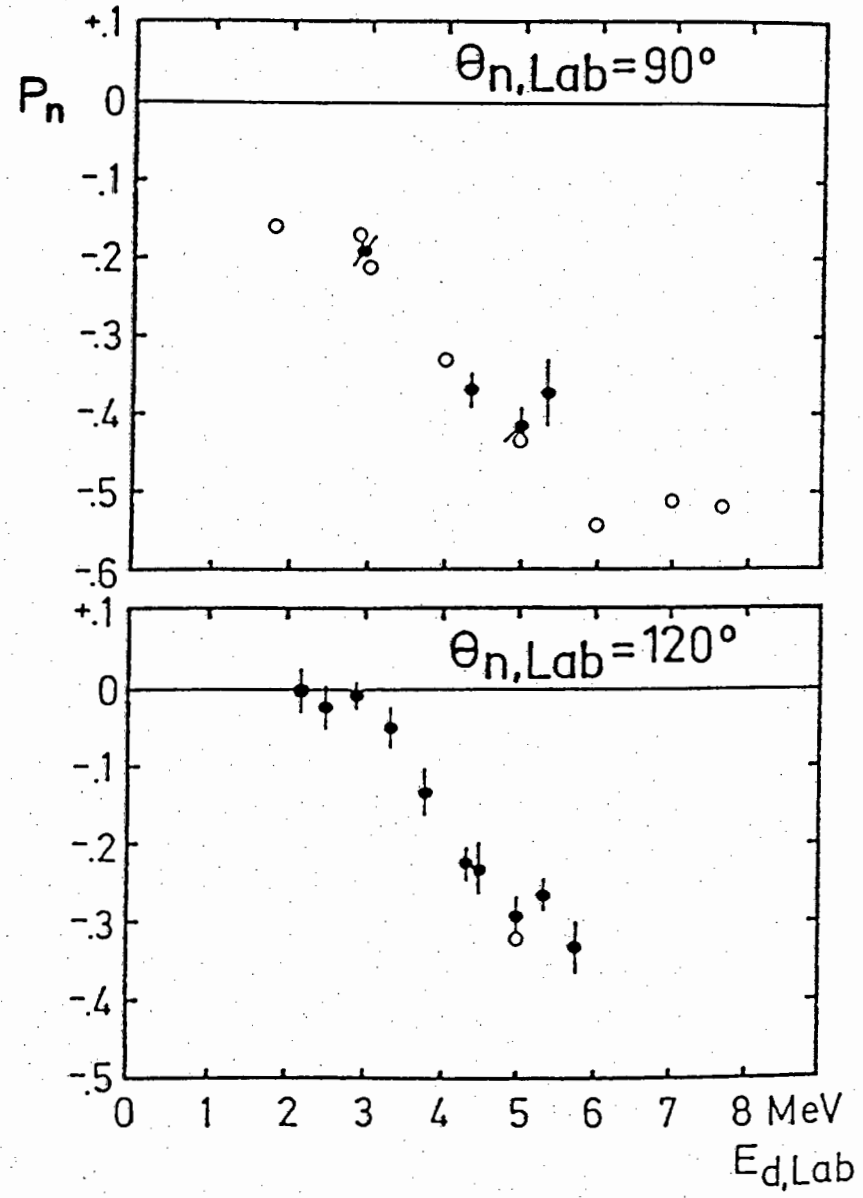

Fig. 6.6 Neutron polarization values for the $T(d,\vec{n})^4He$ reaction at reaction angles $\xi=90^\circ$ and $\xi=120^\circ$. Closed symbols are data from Busse et al (BU67). Open symbols are from earlier work. Figure from BU67.

events from the non-escaping proton recoils to an even greater extent because the plastic scintillator response is such that the S pulse from protons is much smaller than for the anthracene crystal. The escaping protons will therefore lie closer to the Compton electron ridge. The wafer-like crystal would be particularly useful at facilities where no beam spin-reversal is available.

6.6 Conclusions

The present data are in agreement with the most recently published n-p polarization data at 22 MeV (WI84) which were obtained with neutron production and detection techniques completely different from the present experiment. The present data also agree with the updated previous Cape Town (JO74) measurement. The corrected Morris data (MO74), though systematically higher, are consistent with the above measurements, especially at the larger angles.

The major conclusion drawn from comparing the present data (together with the other measurements) to available nucleon-nucleon scattering predictions is that none of the global analyses give the correct polarization for n-p scattering. The Bohannon single energy analysis at 25 MeV is probably in need of review following the present updating of the original MO74 and JO74 data on which it was partially based.

None of the n-p polarization measurements at 21.6 MeV show any indication of zero-crossing at large scattering angles, which implies that any F-wave contribution is very small. This is in agreement with the large-angle measurement (see fig. 6.3) made at 25 MeV at Wisconsin (SR86).

To summarise then, a fit to all of the n-p data at E_n= 21.6 MeV gives (for $^3S_1$ = 84.0°) Δ^P_{LS}=0.880° ± 0.023° and Δ^D_{LS}=0.12° ± 0.01° . A proper assessment of whether or not there is evidence for isotopic spin splitting of the triplet P-wave phase shifts (ie. Δ^P_{LS}[n-p] - Δ^P_{LS}[p-p]) in the vicinity of 25 MeV may now be possible by including the new data in an updated phase shift analysis.

The anthracene polarimeter has shown iself capable of precision n-p polarization measurements at 21.6 MeV. However, a limitation is a residual systematic asymmetry of ≤ 1% . This implies that further applications (either as a polarimeter or an analyzer) would require

(a) a null measurement at an equivalent energy so as to monitor and provide a correction for any residual asymmetry; or

(b) further investigation to try to account for the residual asymmetry.

If this systematic error is indeed being caused by a difference in the proton recoil escape component associated with the two crystal orientations, the use of the polarimeter at a facility with beam spin-reversal should resolve the problem since the crystal could be kept stationary.

APPENDIX 1.1

PHASE SHIFT ANALYSIS

Brief review of scattering theory (based on MA60)

Direct information about the force between two nucleons is principally obtained by scattering one nucleon off another. According to the generalized Pauli principle, a pair of nucleons can exist only in states whose total wave function is antisymmetric (ie. changes sign) under interchange of the two particles (see for example GI80). The total wave function may be written as $\psi=\phi\chi\tau$ where

$\phi(r_1,r_2)$ is dependent on the space coordinates of the two particles,

$\chi(s;m_1,m_2)$ is dependent on the z-components of their spins,and on the total spin s. The quantity $m_1 + m_2$ is the z-component of s .

$\tau(T;T_{31},T_{32})$ is dependent on the total isospin T and on the z-components of isospin for the two nucleons(T_{31} and T_{32}).

In spin-dependent scattering experiments, the measured properties depend upon the properties of the various interactions involved, and upon the geometric configuration (ie. energy and angle). If the states before and after a scattering process are related by $\psi_f = S\psi_i$, the density matrices (WO52,DA52) characterizing the system before and after scattering are related by $\rho_f = S\rho_i S^*$. For scattering experiments in which the final particles are counted outside the unscattered beam, the incident beam must be subtracted out. Then $\rho_{sc}= R\rho_i R^*$ where

R=S-1. The ρ_{sc} defined in this way describes the scattered wave. Because the momentum can usually be considered well defined in scattering experiments, a spin density matrix $\rho(\underline{k})$ can be defined where $\underline{k}$ is a state of relative momentum. On the dynamical side, the momentum-space matrix element $\langle \underline{k}|R|\underline{k}'\rangle$ is a matrix in spin-space whose elements, aside from a normalization factor, are the scattering amplitudes for initial and final spin states. In the description of polarization phenomena, it is convenient to incorporate this normalization factor and to deal also with the spin matrix $M(\underline{k},\underline{k}')$ whose matrix elements are exactly the scattering amplitudes in various final spin states for fixed initial spin states. Then $\rho_{sc}(\underline{k})=M(\underline{k},\underline{k}')\rho_i(\underline{k}')M^*(\underline{k},\underline{k}')$ where the freedom in the normalization of the $\rho(\underline{k})$ has been exploited. The operator $M(\underline{k},\underline{k}')$ is a matrix in the spin-space of the two particles and can be expanded in terms of a general function whose coefficients are complex functions of energy and angle. See (MA60) for the full expression. The coefficients are called the Wolfenstein parameters. A more convenient form of the M matrix was originally given by Wolfenstein (WO54) which restricts the terms of the expression to singlet (s=0) and triplet (s=1) states.

Nucleon-nucleon scattering occurs within the constraints imposed by invariance under time reversal and conservation of angular momentum and parity. For a given total angular momentum $\underline{J}$, the proton-proton system has five independent ways in which the intrinsic spins and the orbital angular momentum can couple together (MA69b). Hence the p-p system has five complex scattering amplitudes. The antisymmetry of the p-p wave function when combined with the conservation of angular momentum and parity prevents mixing of singlet and triplet spin states.

Under the assumption that the proton and neutron are isotopic states of the same particle that differ only in the z projections of their isospins, the neutron-proton wave function must be antisymmetric. Scattering occurs in the two isospin states (T=1 and T=0), and so there are ten independent n-p scattering amplitudes. The T=1 amplitudes as measured in p-p and n-p scattering should be identical in all but electromagnetic effects, if the charge independence hypothesis holds. This assumption is indispensible for analysis of existing n-p scattering data. The n-p data can then be analyzed to give the corresponding T=0 amplitudes.

Analyzing nucleon-nucleon data (based on MA69b,SI69)

In practice attempting to analyze the data directly in terms of the scattering matrix is difficult and has not been done. As an alternative a general formalism is required to express in a simple way the dependence of the observed quantities on the characteristic parameters describing the interaction. This formalism should lead to a common meeting ground for experiments and theory, in which the experiments can be summarized with some ease and theory can be expressed quite directly. The formalism used so far has been the partial wave analysis. This separation of the scattering amplitude $a(\theta)$ into the partial waves of different angular momentum is general, relativistically covariant and independent of any potential model. The scattering amplitudes are essentially unknown functions of energy E and scattering angle θ and can be expanded in terms of angular momentum states $a(E,\theta) = f(E)g(\theta)$. The $g(\theta)$ are known functions that depend on spin, orbital angular momentum and total angular momentum (s,l,J)

of the system. The f(E) are unknown functions of energy and are expressed in the following unitary form $f(E) \propto e^{i\delta(E)}$ where the $\delta(E)$ are phase shifts which carry labels s,l,J. The spectroscopic form for the phase shifts has traditionally been $\delta(E) \equiv {}^{2s+1}l_J(E)$, although the new notation is $\delta \equiv (2s+1)lJ$ as indicated by, for example, Bugg (BU85). The kind of phase shifts almost universally used are those designated nuclear bar. The Pauli principle places restrictions on the possible states of a nucleon-nucleon pair. The permitted states are given by l+s+T=odd. The mixing of states of pure L occurs because only the total angular momentum J, not L, is conserved when the colliding particles have spin. Because of unitarity, only three parameters are needed to describe the behaviour of each pair of states with S=1 and $L=J\pm1$, two phase shifts $\delta_{J\pm1}$ and a mixing parameter ε_J.

The phase shift decomposition of scattering amplitudes has several advantages : because a few low-l phases dominate the scattering, the number of free (phenomenological) phases can be kept reasonably small; physical information can be inserted by using effective-range low-energy limits for S-waves; theory can be inserted by calculating the small, high-l phases from the one-pion-exchange Feynman diagram; and the observed energy dependence of the phase shifts can be used to test theoretical models. The big disadvantage of phase-shift formalism is that the equations are nonlinear.

It is important to realise that phase shifts are not the aim and end of the study of the nucleon-nucleon interaction. They are stepping stones —— they provide a compact summary of the experimental data, and even then not as well as we would like.

Formalism relating phase shifts and observables (based on MA60)

Experimental observables such as differential cross sections, analyzing powers etc. can be expressed in terms of the Wolfenstein parameters. Results can be found in the literature eg. (MA60,PH60). The requirement is therefore that the Wolfenstein parameters be expressed in terms of the phase shift parameters. The Wolfenstein parameters can be expressed in terms of the M-matrix elements, and may be obtained by taking traces of the expression for M. The M-matrix elements in turn can be expressed in terms of the R-matrix elements via the relationship $M(\underline{k},\underline{k}') = 4\pi/2ik \langle\theta,\phi|R|\theta',\phi'\rangle$. R is then decomposed into partial waves , and is represented by a series of two-by-two unitary matrices whose elements are functions of the phase shifts and mixing parameter. In effect then, the physical observables can be obtained from the phase shift parameters.

Phase shift analyses of the data (based on MA60)

As shown above, once one has phase shifts it is a fairly simple matter to calculate the observables. However, the reverse procedure is not at all trivial. Given the experimental quantities, there is in general no analytical procedure to obtain from them the phase shifts. A set of phase shifts can only be properly determined by making least-squares fits to the data. (Similarly, calculation of potentials directly from the phase shifts has proved to be impossible. Parameters of a nuclear-force model can be determined only by making least-squares fits to the phase shifts or to the data directly).

In general, a set of phase shifts is selected, the corresponding observables are calculated, and the least-square sum for a fit to the data is determined and then improved by stepwise alteration of the phase shifts. The goodness of fit criterion is given by

$$\chi^2 = \Sigma \frac{(E_i - O_i)^2}{\sigma_i^2}$$ where E_i is the experimental measurement, O_i is the value of the observable as calculated from the set of phase shifts in question, and σ_i is the standard deviation pertaining to the experimental measurement. The index i is carried over all the pieces of data included in the analysis. χ^2 is to be minimised. The procedures used in searching for the χ^2 minimum are discussed in ref. (M072).

It is important, when performing a phase shift analysis,to have an objective criterion for choosing how many phase shifts to include. The number of phase shifts to be included in an analysis depends on the energy at which the measurements were carried out as well as on the precision of the data. In practice, the number of phase shifts considered in an analysis is limited by the maximum number of parameters that can be obtained from the data in question.

Data can also be analysed at all energies simultaneously (see also M072), in which case coefficients describing the energy dependence of phase shifts are determined from the experiments. Two approaches are possible. The one method involves carrying out phase shift analyses at each energy at which sufficient data exists and fitting smooth curves through plots of the phase shifts vs. energy. Considerations of causality give a maximum rate of

change of phase shifts with energy. The other method assumes a plausible functional dependence for the phase shifts, given perhaps by meson theory, which has a suitable number of arbitrary constants. Data at all energies are then used to find the constants. The problem here is to select the functional form without putting unreasonable constraints on the data.

APPENDIX 1.2

Adjustments to previously published n-p data

The values of the incident neutron beam polarization as used in the following publications have required adjustments as outlined below.

i) The 21.1 MeV data of Morris et al. (MO74)

Analyzing power measurements were made using the $T(d,\vec{n})^4He$ reaction with E_d = 5.35 MeV. Measurements were made at two reaction angles, $\xi = 30^\circ$ to give 21.1 Mev neutrons and $\xi = 80^\circ$ to give 16.9 MeV neutrons. The polarization of the neutron beams as measured by Smith and Thornton (SM72) is as follows:

for E_n = 21.1 MeV , P_{inc} = 0.35 and

for E_n = 16.9 MeV , P_{inc} = -0.50 .

These values were also mentioned by Morris et al. (MO74), hereafter MO74. However, when the asymmetry measurements for the 21.1 MeV data were converted to analyzing powers, the incident polarization value used clearly appears to have been 0.50 instead of 0.35. Assuming this to be so, the published analyzing powers and the corresponding uncertainties are too small by a factor of 0.7.

The following table which is based on table I of MO74 gives their analyzing power values before and after correction :

θ_{cm}	ε_m	f_b	quoted P_1	corrected P_1
40°	0.0166±0.0017	1.12	0.0373±0.0038	0.0531±0.0054
60°	0.0213±0.0012	1.08	0.0460±0.0027	0.0657±0.0037
80°	0.0227±0.0018	1.04	0.0472±0.0037	0.0675±0.0053
100°	0.0177±0.0037	1.07	0.0380±0.0080	0.0541±0.0113
120°	0.0086±0.0050	1.10	0.0190±0.0110	0.0270±0.0157
140°	0.0029±0.0012	1.10	0.0065±0.0027	0.0091±0.0038

Here ε_m is the measured asymmetry, f_b is a correction factor such that $\varepsilon_c = \varepsilon_m f_b$, and $P_1 = \varepsilon_c / P_{inc}$.

ii) The 21.6 MeV data of Jones and Brooks (JO74)

These analyzing power values have been updated to take into account the more recent $T(d,\vec{n})^4He$ polarization values of Smith and Thornton (SM72). Correction factors which are needed are based on the original data sets given in the Ph.D thesis of Jones (JO72). These sets are reproduced below:

Set	E_d	ξ	E_n	P_{inc} used	P_{inc} updated
D	5.0 MeV	20^o	21.6 MeV	0.21	0.25
E	5.0 MeV	20^o	21.6 MeV	0.21	0.25
F	5.0 MeV	20^o	21.6 MeV	0.21	0.25
G	5.35MeV	30^o	21.4 MeV	0.30	0.35

The published average analyzing power for each scattering angle θ_{cm} comprised some or all of the above sets in various combinations. The correction factor for each θ_{cm} was obtained by recalculating the weighted average analyzing power value using the updated polarization values. The ratio of the new average to the old gives the correction facter shown in the table below.

θ_{cm}	P_{np} quoted	correction factor	P_{np} corrected
50^o	0.060	0.84	0.050
70^o	0.063	0.84	0.053
90^o	0.056	0.80	0.045
110^o	0.038	0.82	0.031
130^o	0.024	0.81	0.019
150^o	0.018	0.80	0.014
170^o	0.000	0.84	0.000

In a paper by Brock et al. (BR81), where the necessity for the correction was first pointed out, the correction factor was calculated as 0.84 for all scattering angles.

APPENDIX 2.1

Reproduction of the paper of Brooks and Jones detailing the original anthracene scintillation polarimeter

NUCLEAR INSTRUMENTS AND METHODS 121 (1974) 77–85; © NORTH-HOLLAND PUBLISHING CO.

A SCINTILLATION POLARIMETER FOR n–p SCATTERING STUDIES

F. D. BROOKS and D. T. L. JONES*

Physics Department, University of Cape Town, Rondebosch, C.P., South Africa

Received 29 October 1973

A neutron polarization analyser is described in which the direction dependence of the scintillation pulse shape discrimination (PSD) properties of an anthracene crystal provide the basis for observing the left–right asymmetry of recoil protons associated with the n–p scattering of monoenergetic neutrons within the crystal. The polarimeter consists of a single anthracene crystal mounted on a magnetically shielded photomultiplier tube which is fitted with a PSD circuit. The pulse height and PSD outputs from the photomultiplier are analysed in two parameter mode and a set of observations consisting of a pair of two-parameter spectra leads to a measurement of the recoil proton asymmetry as a function of recoil angle. The polarization in n–p scattering is then deduced as a function of centre-of-mass scattering angle θ_{cm} for values of θ_{cm} in the range 50°–180°.

1. Introduction

In a companion paper[1]) we described an investigation of the scintillation pulse height responses and scintillation pulse shape discrimination (PSD) properties of some organic crystals. The direction dependence of these properties was studied for recoil protons from incident neutrons with energies in the range 1–22 MeV. In anthracene crystals in particular the scintillation pulse shape was found to be markedly direction dependent over most of this energy range. It was apparent that the PSD properties of anthracene, besides providing the familiar means for discriminating against gamma-ray backgrounds, could also provide a means for sensing the directions of recoil protons released within the crystal. An obvious application occurred in the study of the neutron polarization in n–p scattering[2]). A scintillation polarimeter was developed in which the direction dependence of the PSD output provided the means for determining the left–right asymmetry of the proton recoils from n–p scattering. The design and operation of this polarimeter are described in this paper and its suitability for the study of the polarization in n–p scattering is discussed.

2. Outline of the method

The equipment used is identical to that described in ref. 1 and consists of a single anthracene crystal mounted on a magnetically shielded photomultiplier tube fitted with a PSD circuit[3]). The photomultiplier provides three output pulses, namely: a fast output signal for time-of-flight spectroscopy; a linear output L which is proportional to the total light in the scintillation; and a PSD output S which depends non-linearly on the proportion of slow component in the scintillation decay. The L and S outputs are processed by the same electronic system and two-parameter analyser as in ref. 1 to give two-parameter spectra of counts versus L versus S. We refer to these spectra as LS spectra.

The laboratory arrangement for polarization measurements is shown schematically in fig. 1a. A monoenergetic neutron beam is taken at angle ζ from for example, the T(d,n) reaction. The monoenergetic beam is selected by time-of-flight gating unless the choice of beam and target makes this unnecessary. The neutron and deuteron beams define a horizontal plane and the anthracene crystal is oriented at (α,β) to

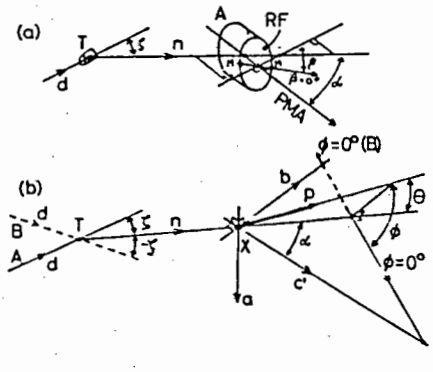

Fig. 1. Schematic diagrams of experimental geometry showing deuteron beam d, neutron beam n and tritium target T. (a) Diagram showing reference face RF of anthracene crystal A, photomultiplier axis PMA, and $\beta = 0°$ axis, defined by marks M. (b) Diagram showing centre X of crystal, mutually perpendicular crystal axes, a, b and c', and recoil proton p. The azimuthal axis $\phi = 0°$ is defined by projecting the deuteron beam onto a plane normal to the neutron beam. The dashed lines illustrate changes implied by a switch from position A to position B.

* Present address: Physics Department, University of Wisconsin, Madison, Wisc. 53706, U.S.A.

the neutron beam where α and β correspond to the angles referred to as θ and ϕ in ref. 1. The angle α is the angle between the photomultiplier axis and the neutron beam. The angle β is the angle between the projection of the neutron beam on the reference face of the crystal and the azimuthal axis of the crystal. The reference face is that face of the crystal which is optically coupled to the photomultiplier cathode and the azimuthal axis, $\beta = 0$ in fig. 1a, is a line which is arbitrarily defined in this face. To simplify the present discussion we shall restrict ourselves to the anthracene crystal A of ref. 1, for which the reference plane was an *ab*-plane and for which the photomultiplier axis therefore coincided with artificial *c'*-axis of the crystal[1]). For this crystal or for any other anthracene crystal therefore, the angle α could equally well be defined as the angle between the neutron beam and the *c'*-axis of the crystal.

The pulse height anisotropy properties of anthracene for protons are such that, for a given proton energy, *L* is a minimum for protons moving parallel to the *b*-axis of the crystal and a maximum for protons moving parallel to the artificial c'-axis[4]). The PSD anisotropy characteristics[1]) are such that *S* is maximum when *L* is minimum and vice versa, as can be seen in fig. 2 of ref. 1. An optimum orientation for asymmetry measurements is one in which there is maximum variation of *S* for proton recoils to left and right of the neutron beam direction.

This is achieved if the *a*-axis of the crystal is aligned vertical (so that the *bc'*-plane is horizontal) and the neutron beam direction is intermediate between the *b*- and *c'*-axis so as to make the angle $\alpha = 60°$, as shown in fig. 1b. We define two positions A and B (fig. 1b) at this orientation, depending whether a proton recoil from the neutron beam towards the *c'*-axis is in the same sense (A) or the opposite sense (B) as the deflection from the deuteron beam to the neutron beam. We can change from position A to position B by changing ζ to $-\zeta$, as shown in fig. 1b or by rotating the crystal through 180° about the neutron beam or by rotating the crystal about the *a*-axis until the *c'*-axis makes an angle $(2\pi - \alpha)$ with the neutron beam. The photomultiplier is mounted in such a way that any one of these angles may be adjusted without affecting the other two.

An *LS* spectrum obtained at the orientation $(\alpha,\beta) = (60°, 40°)$ and with other conditions identical to those used for fig. 2 of ref. 1 is shown in isometric projection in fig. 2. A contour plot of the same spectrum is shown in fig. 3. The structure in this spectrum is similar to that in the spectra shown in ref. 1 except that the proton ridge P now splits into two ridges P_1 and P_2 (see fig. 3) over most of its length. We can show that these ridges correspond to protons recoiling into the forward quadrants on either side of a vertical plane through the neutron beam. The ridge P_1 corresponds to recoils into the quadrant containing the *c'*-axis and P_2 to recoils into the quadrant containing the *b*-axis. By comparing the numbers of counts under each ridge

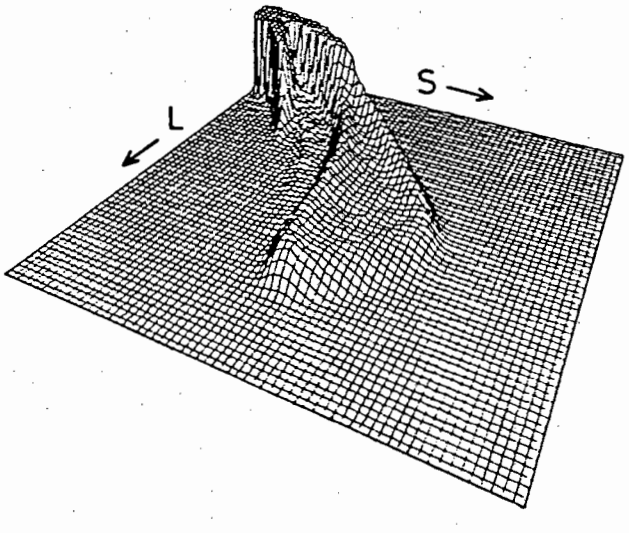

Fig. 2. Isometric plot of an *LS* spectrum obtained for 21.6 MeV neutrons incident on the anthracene crystal A. The spectrum shows counts (vertical) vs pulse height *L* vs PSD output *S*. The upper limit of the count scale is 500.

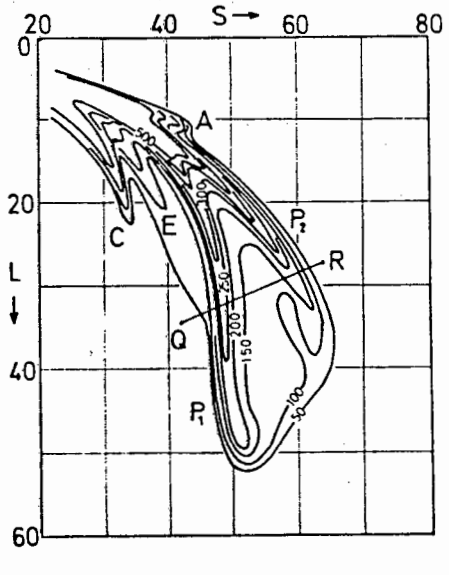

Fig. 3. Contour plot of the *LS* spectrum shown in fig. 2. The ridges in the spectrum are identified as follows: Compton electrons, C; recoil protons P_1 and P_2; escaping recoil protons E; and alpha particles, A. The line QR represents the locus of a constant recoil angle θ.

we can determine the left–right asymmetry of the proton recoils within the crystal.

The proton component of the LS spectrum includes recoils at laboratory angles ranging from 0° to almost 90° relative to the neutron beam. The pulse height L depends on the energy E_p and on the direction of the recoil proton. The proton direction is specified by the angle of recoil θ relative to the neutron beam and the azimuthal angle of recoil ϕ. The azimuthal axis is defined by projecting the deuteron beam onto a plane perpendicular to the neutron beam, as illustrated in fig. 1b. The energy E_p is related to the angle θ and the incident neutron energy E_n by

$$E_p = E_n \cos^2 \theta. \qquad (1)$$

From measurements[1]) of the L and S anisotropies we know that the loci of constant E_p and hence of constant recoil angle θ approximate to straight lines across the LS-plane, such as the line QR in fig. 3. By defining a series of such lines we can therefore divide the proton region of the LS spectrum into angle bins corresponding to different recoil angles. In principle therefore a single LS spectrum contains sufficient information to determine the left–right asymmetry as a function of recoil angle over a wide range of recoil angles.

3. Operation for a particular proton recoil angle

The operation of the asymmetry analyser is best described by first showing how the left–right asymmetry would be calculated if the LS spectrum contained only proton recoils at a particular recoil angle and then showing how the LS spectrum is sub-divided into a set of recoil angle bins for a series of such calculations. We therefore confine the initial discussion to a specific proton recoil angle $\theta = 30°$ and to a specific neutron energy $E_n = 11$ MeV for which the recoil proton energy at $\theta = 30°$ is $E_p = 8.3$ MeV, from eq. (1). The direction dependence of S at this energy may be deduced from the data given in fig. 5 of ref. 1 for the nearby neutron energy of 8 MeV. These data are referred to the crystal coordinate frame defined in ref. 1, so we must transform them to the present laboratory frame in which the crystal is oriented at $(\alpha, \beta) = (60°, 40°)$. The transformed data for position A of this orientation in the laboratory frame are shown in fig. 4. The laboratory recoil directions corresponding to minimum and maximum PSD output, S_{min} and S_{max} are $(\theta, \phi) = (60°, 0°)$ and $(30°, 180°)$ respectively. From fig. 4 we can read the variation of $S(\theta, \phi)$ with ϕ for the recoil angle $\theta = 30°$ and we obtain a curve of the form shown in fig. 5a, in which S ranges between the values S_- (at $\phi = 0°$) and S_+ (at $\phi = 180°$). We define the fractional dispersion $F(\theta)$ of S with ϕ for recoil angle θ by

$$F(\theta) = (S_+ - S_-)/(S_{max} - S_{min}). \qquad (2)$$

Thus from the data shown in fig. 4, $F(\theta) = 0.9$ at $\theta = 30°$. These data also indicate that for any value of θ within the range $\theta \lesssim 70°$ the PSD outputs at $\phi = 90°$ and 270° are very nearly equal. Assuming that in the ideal case these outputs for $\phi = 90°$ and 270° are the

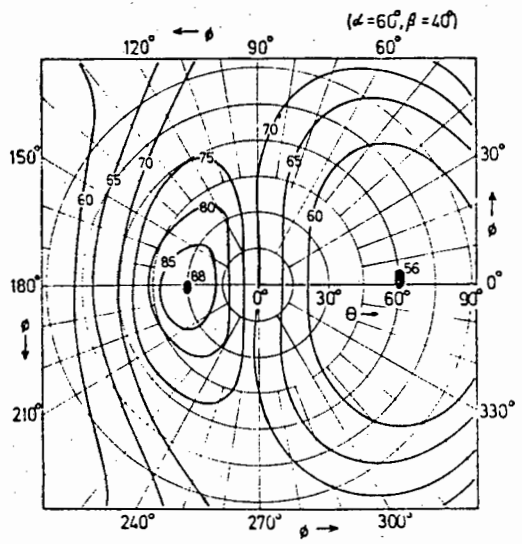

Fig. 4. Contours of equal PSD output S for 8 MeV protons as a function of proton direction (θ, ϕ). The plot is for the crystal orientation $(\alpha, \beta) = (60°, 40°)$ and was obtained by transforming the data shown in fig. 5 of ref. 1 to this orientation. The latter figure is equivalent to a contour plot of $S(\theta, \phi)$ for the crystal orientation $(\alpha, \beta) = (0°, 40°)$.

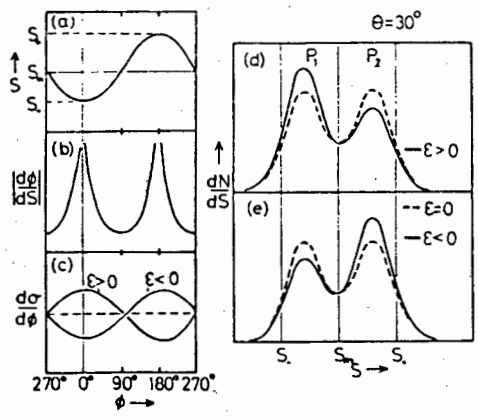

Fig. 5. PSD responses and spectra (schematic) for 8 MeV proton recoils at $\theta = 30°$: (a) PSD output S vs recoil azimuth ϕ; (b) $|d\phi/dS|$ vs ϕ; (c) $d\sigma/d\phi$ vs ϕ from eq. (3); (d) projected and resolution-broadened spectra dN/dS vs S for $\varepsilon > 0$ (solid curve) and $\varepsilon = 0$ (dashed curve); and (e), as (d) but for $\varepsilon < 0$ (solid curve).

same and equal to $S_m(\theta)$ for recoils at angle θ, we note further that $S<S_m(\theta)$ for ϕ in the range $0°\pm90°$ and $S>S_m(\theta)$ for ϕ in the range $180°\pm90°$. Thus the PSD output S indicates whether the associated proton recoil direction is to the "left" or the "right" of the neutron beam. For equal numbers of left and right recoils $S_m(\theta)$ should correspond to the median of the number distribution with respect to S.

The left–right asymmetry $\varepsilon(\theta)$ of proton recoils from n–p scattering may therefore be deduced from the amplitude distribution of the S output as follows. The partial differential cross section $(d\sigma/d\phi)_{\theta\phi}$ for elastic proton recoil in direction (θ, ϕ) in the laboratory frame is given by

$$(d\sigma/d\phi)_{\theta\phi} = [\sigma(\theta)/2\pi]\,[1+P_0\,P(\theta)\cos\phi] = [\sigma(\theta)/2\pi]\,[1+\varepsilon(\theta)\cos\phi], \quad (3)$$

where $\sigma(\theta)$ is the total differential cross section for elastic recoil at angle θ, P_0 denotes the polarization of the incident neutron beam, and $P(\theta)$ denotes the analysing power for proton recoils at angle θ in n–p scattering.

The number of proton recoils per unit S at angle θ and leading to a PSD output S may now be written

$$(dN/dS)_{\theta S} = k\sum_{\phi}(d\sigma/d\phi)_{\theta\phi}\,|d\phi/dS|_{\theta\phi}, \quad (4)$$

where k depends on the incident neutron intensity and the crystal thickness and the sum is taken over all values of ϕ which correspond to the value S (see fig. 5a). The modulus $|d\phi/dS|_{\theta\phi}$ is derived as a function of ϕ from fig. 5a and has the form shown in fig. 5b while $(d\sigma/d\phi)_{\theta\phi}$ is given by eq. (3) and has one of the three forms shown in fig. 5c, depending whether $\varepsilon(\theta)$ is zero, positive or negative.

The S amplitude distribution for a constant recoil angle θ is thus obtained by taking the product, as in eq. (4), of the functions shown in figs. 5b and 5c and convoluting with the resolution function of the PSD output measurement. Figs. 5d and 5e illustrate schematically the types of distribution that will result for either zero, positive or negative values of $\varepsilon(\theta)$.

Projecting the LS spectrum associated with proton recoils at a particular angle θ, e.g. $\theta = 30°$, onto the S axis therefore leads to a distribution of the form shown in fig. 5d or 5e. The peaks P_1 and P_2 in this distribution correspond to the ridges P_1 and P_2 in the LS spectrum. If the proton asymmetry $\varepsilon(\theta)$ increases the peak P_1 increases in height and the peak P_2 decreases. The opposite happens if $\varepsilon(\theta)$ decreases.

In changing from position A to position B (fig. 1b) we either change ζ to $-\zeta$, or we change α to $(2\pi-\alpha)$ or we rotate the crystal through 180° about the neutron beam. The first method reverses the sign of the incident polarization P_0 and hence also that of $\varepsilon(\theta)$. The second and third methods produce an equivalent effect since they shift the phase of figs. 5a and 5b by 180° relative to that of fig. 5c. The effect on the projected S spectrum is therefore the same whatever the method used to change from position A to position B. If the S spectrum for position A resembles the solid curve in fig. 5d then that for position B will resemble the solid curve in fig. 5e and vice-versa.

In principle the asymmetry $\varepsilon(\theta)$ can be determined by comparing the integrals under the peaks P_1 and P_2 observed in either position A or position B. For position A the integral under the lower part $[S<S_m(\theta)]$ corresponds to recoils with ϕ in the range $0°\pm90°$. Thus the integral $N_<$ under this part is given by

$$N_< = [k\sigma(\theta)/2\pi]\int_{-\frac{1}{2}\pi}^{+\frac{1}{2}\pi}[1+\varepsilon(\theta)\cos\phi]\,d\phi = [k\sigma(\theta)/2\pi]\,[\pi+2\varepsilon(\theta)]. \quad (5)$$

Similarly the integral $N_>$ under the upper part of the A spectrum corresponding to recoils with ϕ in the range $180°\pm90°$, is given by

$$N_> = [k\sigma(\theta)/2\pi]\,[\pi-2\varepsilon(\theta)]. \quad (6)$$

The asymmetry $\varepsilon(\theta)$ is therefore obtained from eqs. (5) and (6):

$$\varepsilon(\theta) = \tfrac{1}{2}\pi(N_<-N_>)/(N_<+N_>) = \tfrac{1}{2}\pi\,\Delta N_A/N_A, \quad (7)$$

where ΔN_A therefore represents the difference between the integrals under the lower and upper parts of the spectrum obtained at position A and N_A represents the integral of the full spectrum.

The corresponding result obtained using the position B spectrum instead of the position A spectrum is

$$\varepsilon(\theta) = -\tfrac{1}{2}\pi\,\Delta N_B/N_B, \quad (8)$$

where ΔN_B and N_B are defined in the same way as ΔN_A and N_A. The minus sign arises in this case because the lower and upper regions of the spectrum correspond to recoils with ϕ in the ranges $180°\pm90°$ and $0°\pm90°$ respectively, which is the reverse of the situation applying for the position A spectrum.

Asymmetries determined directly from either eq. (7) or eq. (8) will clearly depend sensitively on the value of $S_m(\theta)$ used, through the effect this has on the difference ΔN_A or ΔN_B. However, for small errors in $S_m(\theta)$ the effect on ΔN_A is nearly exactly equal to that

the mean recoil angle θ corresponding to the pulse height L. The angle θ is determined by using the known[4]) relative pulse height versus energy response of anthracene to protons to determine the mean recoil proton energy E_p corresponding to L and using eq. (1) to determine θ from E_p.

The redispersion process is schematically illustrated in fig. 6. Figs. 6a and 6b illustrate the transformation of a single row of the LS spectrum. The transformation may be pictured if we imagine firstly, the distribution shown in fig. 6a shifted along the S axis until its centre corresponds to $S = 2n$ in fig. 6b and secondly, the S scale of fig. 6b multiplied by a factor $(S_+ - S_-)/[2n\,F(\theta)]$. The forms of the two distributions will then be identical and the distributions will only differ in their count scales and in the number of points or histogram steps along their S axes, as illustrated for a small portion of the two distributions in figs. 6c and 6d. The number of counts N_j in channel j of the redispersed distribution is given by

$$N_j = \sum_{i=1}^{4n} f_i N_i , \qquad (10)$$

where N_i represents the number of counts in channel i of the original distribution and f_i is the fraction of this channel which is overlapped by channel j of the redispersed distribution, as illustrated in figs. 6c and 6d.

Since the interval $(S_+ - S_-)$ in the original distribution corresponds to an interval $2nF(\theta)$ in the redispersed distribution we see from eq. (2) that the interval $(S_{max} - S_{min})$ in the former will correspond to an interval $2n$ in the latter. From the data of fig. 4 we can also show that the values $S = n$ and $3n$ in the redispersed distribution will correspond to the limits S_{min} and S_{max} in the original distribution. In the redispersed LS spectrum, therefore, we assume that the S values n and $3n$ correspond to S_{min} and S_{max} for every row or L value as illustrated in fig. 6e. The limits S_- and S_+ which vary with L are illustrated by the lines S_- and S_+ in fig. 6e. These limits vary smoothly from row to row, but always lie symmetrically about $S = 2n$ and within the region $S = n$ to $3n$.

The proton region is now subdivided into angle bins by defining boundaries as illustrated by the lines $V_m W_m$ in fig. 6e. Each such line corresponds to a specific recoil angle and hence to a specific proton energy E_p, given by eq. (1). The pulse height anisotropy[1]) at proton energy E_p is a measure of the amount that L varies as S varies from S_{min} to S_{max}. The angle boundaries are therefore defined with reference to the ordinates $S = n$ and $S = 3n$ as follows. From a calibration run such as fig. 2a of ref. 1, for which the crystal c'-axis was aligned with the neutron beam, we determine the maximum pulse height that could be observed for a proton energy $E_p = E_n$ and mark this point V_0 on the ordinate $S = n$ as shown in fig. 6e. From a similar calibration run such as fig. 2b of ref. 1, for which the crystal b-axis was aligned with the neutron beam, or from the pulse height anisotropy data for anthracene[1]) we obtain the minimum pulse height that could be observed at this proton energy and mark this pulse height W_0 on the ordinate $S = 3n$ as shown in fig. 6e. These points define the bin boundary line $V_0 W_0$ corresponding to the bin limit $\theta = 0°$. The boundaries $V_1 W_1$, $V_2 W_2$ etc. corresponding to successively increasing boundary recoil angles θ are determined by calculating the recoil proton energy from eq. (1), using the relative pulse height versus energy data[4]) for anthracene to determine V_1, V_2 etc. and using the pulse height anisotropy data shown in fig. 6 of ref. 1 to determine W_1 from V_1, W_2 from V_2 and so on.

The first angle bin is thus defined by the lines $V_0 W_0$ and $V_1 W_1$ in fig. 6e, the second by the lines $V_1 W_1$ and $V_2 W_2$ and so on. The boundary lines are extrapolated across the LS plane as shown in fig. 6c and the counts between each pair of boundaries are projected onto the S axis to give the projected spectrum (A or B) for the corresponding angle bin. The counts in those channels which are cut by the boundary lines are distributed proportionally between the bins on either side of the boundary. The asymmetry $\varepsilon(\theta)$ is determined by comparing the projected A and B spectra as outlined in section 3. The median limit $S_m(\theta)$ is specified as outlined in that section. The other limits used in calculating the integrals N_A and N_B and the differences ΔN_A and ΔN_B are specified far away from the proton ridges provided these ridges are well resolved from other significant structure in the projected spectrum. If significant other structure lies close by the ridge, for example that due to alpha particles or escape protons at the low L values (figs. 2 and 3), then limits lying between this structure and the proton ridges are used.

The analysing power $P(\theta)$ for proton recoils at recoil angle θ is equal to $\varepsilon(\theta)/P_0$. Thus, with negligible error we obtain the polarization in n–p scattering $P_{np}(\theta_{cm})$ at the associated centre-of-mass neutron scattering angle $\theta_{cm} = \pi - 2\theta$ from

$$P_{np}(\theta_{cm}) = -P(\theta) = -\varepsilon(\theta)/P_0 . \qquad (11)$$

The calculation of n–p polarization values from pairs (A and B) of LS spectra is accomplished with the aid of a Fortran IV programme POLYANA. The LS spectra from the multiparameter analyzer are provided

either on magnetic tape or punched cards. These are read in together with other data required for the calculation and the complete data reduction is carried out leading directly to a table and plot of $P_{np}(\theta_{cm})$, with errors, as a function of θ_{cm}. The time required for calculation is typically 1 s of c.p.u. time per angle bin on a Univac-1106 computer.

An example of a measurement of $P_{np}(\theta_{cm})$ for 21.6 MeV incident neutrons is shown in fig. 7a. The data shown in this figure are discussed in another publication[5]).

5. Limitations and uncertainties

Although *LS* spectra (figs. 2 and 3) may be obtained which include proton recoils at angles extending over most of the kinematically allowed recoil angle range, $\theta<90°$, only the data at laboratory recoil angles less than about 70° are suitable for analysis. Recoils at larger angles lead to events in the lower pulse height region of the spectrum and cannot be resolved from other components in this region, notably the protons and alpha particles from neutron-induced reactions on carbon. Furthermore, the fractional dispersion $F(0)$ given by eq. (2) drops off at $\theta>70°$, as can be appreciated from fig. 4, and the resolution of the left–right asymmetry determination is consequently impaired. This latter difficulty could be partially overcome by using a different crystal orientation e.g. $(\alpha, \beta) = (45°, 40°)$ instead of $(60°, 40°)$, but then $F(0)$ would be smaller at small recoil angles ($0 \lesssim 40°$) and the sensitivity for asymmetry measurements at these angles would be reduced.

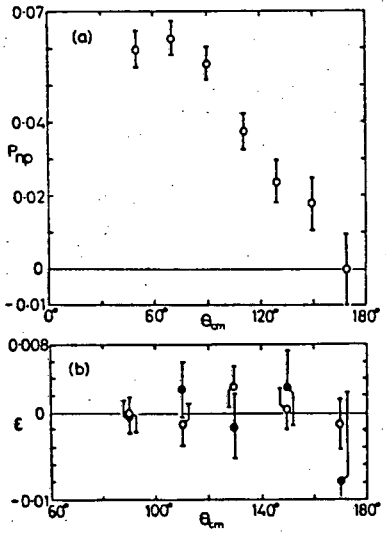

Fig. 7. Polarization P_{np} and asymmetry ε vs neutron cm scattering angle θ_{cm} for incident neutrons of energy 21.6 MeV: (a) polarization measurements; and (b) null asymmetries determined either by using an unpolarized incident neutron beam (solid circles) or from analysis of a pair of A spectra (open circles). The error bars in (a) were calculated from eq. (13). The error bars in (b) are statistical only and were calculated from eq. (12).

Multiple neutron scattering in the anthracene crystal could lead to errors in the polarization measurement, especially if the primary scattering was on carbon, for which the energy loss is small and the analysing power can be high. This problem could be serious with larger crystals, but it appears to be unimportant at the neutron energies ($E_n>10$ MeV) and for the small crystals used to date. The linear dimensions of these crystals are about 2 cm or less and therefore correspond to less than one-tenth of the incident neutron mean free path at these energies.

On the other hand, for small crystals and for neutrons of energy greater than 10 MeV, the fraction of recoil protons escaping from the crystal is appreciable. However, problems that could arise from this effect are largely avoided by the fact that the escaped protons form a separate ridge in the *LS* spectrum (E in fig. 3) and can therefore be excluded to a large extent by proper choice of the integration limits for the asymmetry calculations. The effect of any residual escape component is to dilute the observed asymmetry without introducing spurious asymmetries. This dilution can be estimated and corrected for by using the data obtained in calibration runs, such as that shown in fig. 2a of ref. 1, in which the escape ridge is clearly resolved from the main proton structure.

The fact that virtually every recoil proton is detected has an important consequence when we estimate the statistical uncertainty on an asymmetry measurement within a particular angle bin. The experimental method assigns *every* recoil within a given bin as either "low", if $S<S_m(0)$, or "high" if $S>S_m(0)$, where 0 is the mean recoil angle for the bin. Each recoil either adds one count to, or subtracts one count from, the difference ΔN between the number of low-S and high-S recoils in the bin 0. Therefore, since the difference ΔN is in principle determined directly, ΔN_A and ΔN_B may be regarded as primary observations in the experiment and we can in consequence show that the statistical error $\Delta\varepsilon(0)$ may be estimated from

$$\Delta\varepsilon(0) = (\pi/4N)\left[|\Delta N_A| + |\Delta N_B| + N^{-1}(\Delta N_A^2 + \Delta N_B^2)\right]^{\frac{1}{2}}. \quad (12)$$

From eqs. (9) and (12) it can be seen that for a given N and a given $\varepsilon(0)$ the statistical error $\Delta\varepsilon(0)$ will be a minimum if $\Delta N_A = -\Delta N_B$. The definition of $S_m(0)$

as the median value of the summed A and B spectra in fact ensures this equality and thereby helps to minimize the statistical error.

The systematic errors to which the polarization measurements are also subject include firstly those caused by imprecise knowledge of the incident neutron polarization P_0 and secondly those which may arise from experimental asymmetries or errors which pass undetected and therefore uncorrected in the measurement. Making allowance for these we can express the error $P_{np}(\theta_{cm})$ on the neutron polarization measurement by

$$\Delta P_{np}(\theta_{cm}) = |P_0^{-1}| \{[\Delta\varepsilon(\theta)]^2 + (\Delta\varepsilon_{sys})^2 + [P_{np}(\theta_{cm})\,\Delta P_0]^2\}^{\frac{1}{2}}, \quad (13)$$

where $\Delta\varepsilon_{sys}$ represents the undetected false asymmetry and ΔP_0 the uncertainty on the polarization of the incident neutron beam.

We may estimate an upper limit for the systematic error $\Delta\varepsilon_{sys}$ by measuring a known null asymmetry under conditions simulating those of the actual asymmetry measurement. One way of carrying out a null test is to measure recoil proton asymmetries in the scattering of an unpolarized incident neutron beam, such as that obtained at the angle $\zeta = 0°$ from the T(d,n) reaction. The results of such a test are shown in fig. 7b. Alternatively a null asymmetry should be obtained if like runs are paired (i.e. A and A, or B and B, instead of A and B) and this can be checked using runs obtained at different angle settings. For example suppose that we have a set of four runs consisting of two A runs at (ζ, α) and $(-\zeta, 2\pi-\alpha)$ respectively and two B runs at $(-\zeta, \alpha)$ and $(\zeta, 2\pi-\alpha)$ respectively. From this set we can obtain two independent null checks, based on the A pair and B pair respectively, as well as two independent asymmetry measurements based on AB pairings. The results of a null check of this type are shown in fig. 7b. The error bars shown in fig. 7b represent the statistical errors only. Both null checks are seen to give asymmetries which are consistent with zero. From such checks an upper limit of $\Delta\varepsilon_{sys} = 0.0011$ was deduced and was then used in eq. (13) to calculate the total polarization errors shown in fig. 7a.

6. Discussion

A comparison of the statistical precisions of polarization values obtained by the present method with those obtained in experiments based on conventional double-scattering geometry is of interest. The two methods are similar up to the point that a polarized incident neutron beam is sampled by n–p scattering in an hydrogenous scatterer. In the present method the recoil proton associated with each scattering is observed and analysed as to recoil angle and direction (left or right) without further statistical sampling. In the double scattering method, however, further statistical sampling occurs in the detection of scattered neutrons by two identical detectors which are disposed at equal angles θ on either side of the incident neutron beam. The primary observations in the double scattering geometry are therefore the counts N_1 and N_2 recorded by these detectors for a given number of scatterings in the scatterer. The asymmetry is given by

$$\varepsilon(\theta) = (N_1 - N_2)/(N_1 + N_2), \quad (14)$$

and the standard deviation $\Delta\varepsilon(\theta)$ is estimated from

$$\Delta\varepsilon(\theta) = [4N_1N_2/(N_1+N_2)^2]. \quad (15)$$ *

A comparison of eqs. (12) and (15) for small asymmetries, $|\varepsilon| < 0.1$, and for the same total number of neutrons detected, namely $N_1 + N_2 = N_A + N_B = 10^4$, is shown in fig. 8. Curve (a) shows the standard deviation given by eq. (12) and curve (b) shows the standard deviation given by eq. (15). The comparison in fig. 8 shows that even for asymmetries as large as 10% the statistical errors obtained using the present method should be lower by at least a factor of two than those obtained using the double scattering method. For very small asymmetries in particular the statistical precision of the present method exceeds that of the double scattering method by a much larger factor, more than an order of magnitude for example for $\varepsilon < 0.01$.

The present method is therefore well suited to the

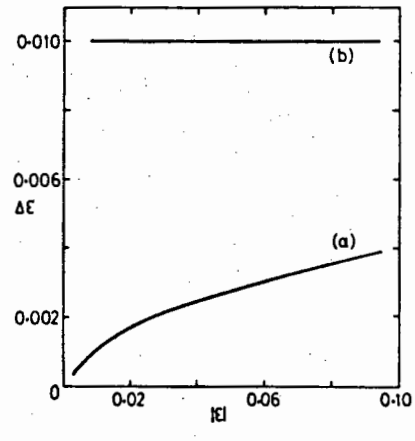

Fig. 8. The statistical error $\Delta\varepsilon$ on the asymmetry ε as a function of $|\varepsilon|$ for a total of 10^4 neutrons detected: (a) by the present method [from eq. (12)]; and (b) if the scattered neutrons are detected [from eq. (15)].

measurement of small asymmetries and should offer advantages in studies of the small polarizations in n–p scattering at neutron energies less than 30 MeV. It is a single-scattering method and is therefore less demanding of neutron beam intensity than double-scattering experiments. Background levels should, in consequence, also be lower than in the double scattering method. The ability to make simultaneous polarization measurements over a range of neutron scattering angles ($\theta_{cm} \approx 50°$–$170°$) is also an advantage. A limitation on the other hand is the resolution on the centre-of-mass scattering angle, which is about 10° for 16 MeV neutrons and is expected to be larger (i.e. worse) at lower energies. This resolution is tolerable in the case of n–p scattering, however, because the polarization P_{np} is expected to be a slowly varying function of θ_{cm}.

The method also has advantages of experimental simplicity. In particular the electronic system required (fig. 1b of ref. 1) is simple and the capacity to tolerate small mechanical misalignments, the effects of which are eliminated in the redispersion stage of the data reduction, is also an advantage. The data reduction process itself, although complex in principle, is simple and straightforward in practice.

The anthracene polarimeter has been used to date with two different crystals, A and B of ref. 1, to study the polarizations in n–p scattering at 16 and 22 MeV. The results will be published elsewhere[5]). Further studies are now being made at other neutron energies in the range 8–30 MeV. It appears that the method will become less effective at neutron energies lower than 8 MeV because the directional resolution of anthracene as indicated by the parameter R in table 3 of ref. 1, drops off with recoil proton energy. On the other hand the polarimeter should be suitable for work at higher neutron energies than 30 MeV and may well prove more effective at these energies than at lower energies, provided crystals large enough to avoid excessive proton escape are used.

We thank Mr P.A. Back for construction of much of the equipment used, the staff of the Southern Universities Nuclear Institute for their cooperation and our colleague Mr G. Pauletta for his assistance in these experiments. We also thank the South African Council for Scientific and Industrial Research for financial support and for a bursary to one of us (D.T.L.J.).

References

1) F. D. Brooks and D. T. L. Jones, Nucl. Instr. and Meth. 121 (1974) 69.

2) F. D. Brooks and D. T. L. Jones, Proc. 3rd Intern. Symp. on *Polarization phenomena in nuclear reactions* (eds. H. H. Barschall and W. Haeberli; Univ. of Wisconsin Press, Madison, 1971) p. 430.

3) F. D. Brooks, Nucl. Instr. and Meth. 4 (1959) 151; F. D. Brooks, R. W. Pringle and B. L. Funt, IEEE Trans. Nucl. Sci. NS-7 (1960) 35.

4) J. B. Birks, *The theory and practice of scintillation counting* (Pergamon Press Ltd., London, 1967).

5) D. T. L. Jones and F. D. Brooks, Nucl. Phys. A222 (1974) 79.

* Correction: Eq. (15) should read $\Delta\epsilon(\theta)=[4N_1N_2/(N_1+N_2)^3]^{1/2}$

APPENDIX 2.2

Pulse-height matching using the two photomultiplier system.

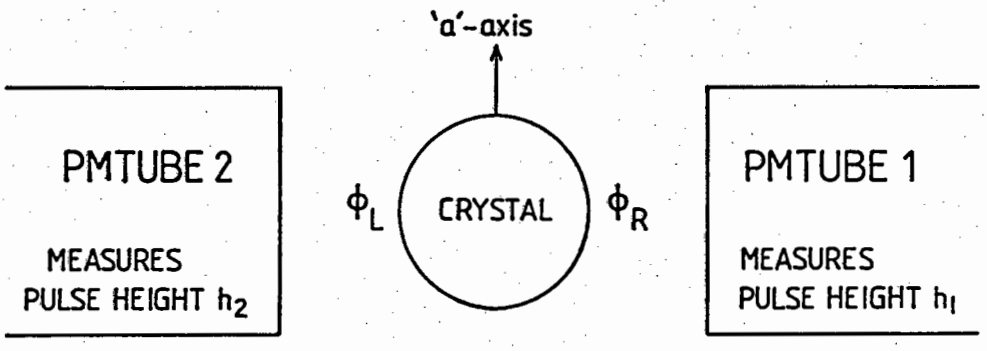

Assume that this is the crystal orientation which measures the A spectrum. The inverted crystal orientation (with the arrow pointing down) then measures the B spectrum.

ϕ_L and ϕ_R are the photon efficiencies with respect to each of the crystal faces, i.e. if a scintillation produces N photons, then $\phi_R N$ photons will reach the P.M.1 cathode face and $\phi_L N$ photons will reach the P.M.2 cathode face.

Hence $h_1^A = k_1 \phi_R N$ and $h_2^A = k_2 \phi_L N$.

Similarly $h_1^B = k_1 \phi_L N$ and $h_2^B = k_2 \phi_R N$.

These signals are summed so as to produce the required usable pulse heights, i.e.

$$h_A = h_1^A + h_2^A = (k_1 \phi_R + k_2 \phi_L)N$$

and

$$h_B = h_1^B + h_2^B = (k_1 \phi_L + k_2 \phi_R)N .$$

The A and B orientation pulse heights are matched by adjusting the high voltage supply to each photomultiplier such that $h_1^A = h_2^B$ (by using the spectra from gamma ray sources, for example).

Then $k_1 \phi_R N = k_2 \phi_R N$

i.e $k_1 = k_2 = k$ say ,

so that $h_A = k(\phi_R + \phi_L)N = h_B$.

If not correctly set up, say $k_1 = k_2 + \Delta k$.

Then $h_A - h_B = \{ k_1(\phi_R - \phi_L) + k_2(\phi_L - \phi_R) \}N$

$= (k_1 - k_2)(\phi_R - \phi_L)N$

$= \Delta k (\phi_R - \phi_L)N$.

Hence $\Delta h/h = (h_A - h_B)/h_A \cong \{ \Delta k(\phi_R - \phi_L)\}/\{k(\phi_R + \phi_L)\}$.

So, the fractional error in the pulse height h is smaller than the fractional error in k by a factor $(\phi_R - \phi_L)/(\phi_R + \phi_L)$.

Alternatively, say $k_1 = gk_2$ and $\phi_R = f\phi_L$.

Then $h_A - h_B = k_2 (g - 1)(\phi_R - \phi_L)N$

$= k_2 (g - 1) \phi_L (f - 1)N$.

Therefore $(h_A - h_B)/h_A = \{(g - 1)(f - 1)\}/(gf + 1)$

i.e $h_B = h_A \{ 1 - [(g - i)(f - 1)/(gf + 1)] \}$.

Example Say $f = \phi_R/\phi_L = 0.95$. Then for various values of g, the corresponding values for the pulse height ratios h_B/h_A are obtained:

g	0.8	0.9	1.0	1.1	1.2
h_B/h_A	0.9943	0.9973	1.0	1.0024	1.0047

Again it can be seen that matching the photomultiplier outputs is not critical in producing similar A and B pulse heights.

APPENDIX 4.1

Non-criticality of the median determination using spectra which coincide.

Suppose the A and B spectra coincide, and have also been normalised. Assume the median used does not correspond to the true median, as shown in the diagram below.

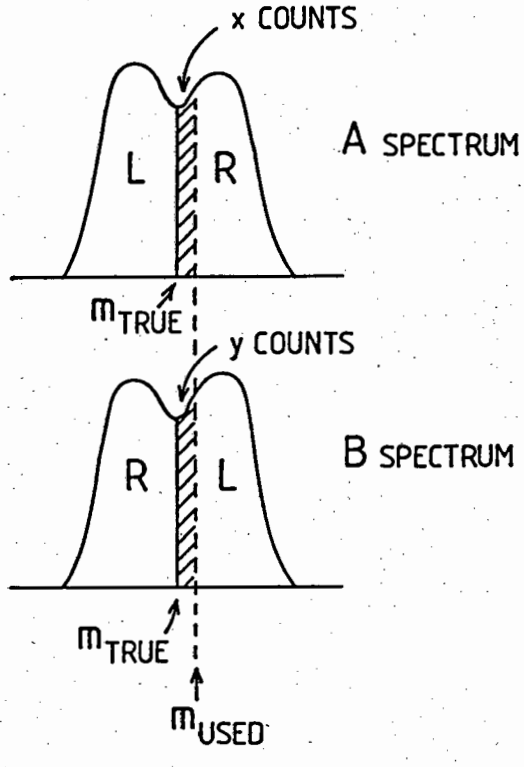

L,R,x and y are the integrated counts in the sections shown. The calculated asymmetries for the A and B spectra are thus

$\varepsilon_A = \{ (L + x) - (R - x) \}/total$ and

$\varepsilon_B = \{ (L - y) - (R + y) \}/total$ respectively.

Hence $\varepsilon_{calc} = (\varepsilon_A + \varepsilon_B)/2$

$= (L-R+2x+L-R-2y)/2(total)$

$= (2L-2R+2x-2y)/2(total)$

$= (L-R)/total + (x-y)/total$

$= \varepsilon_{true} + (x-y)/total$

Since $x \cong y$ (because these counts are in the region where asymmetry is minimal), $\varepsilon_{calc} = \varepsilon_{true}$.

APPENDIX 4.2

<u>False asymmetry caused by one spectrum being shifted relative to the other.</u>

The two crystal orientations which are used when making asymmetry measurements give rise to an A and B spectra pair.

For the sake of simplicity it is assumed that the B spectrum is normalised to A, and that the asymmetry is exactly the same for each spectrum.

If the B spectrum is shifted with respect to A, the calculated median m_{calc} (calculated from the sum spectrum A+B) does not coincide with the true median m_{true}.

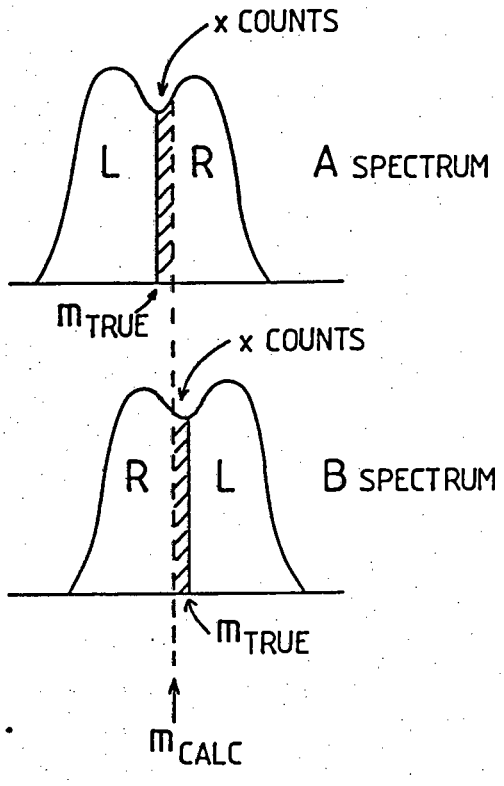

The true asymmetry is $\varepsilon_T = (L - R)/\text{total}$.

Using m_{calc}, the A spectrum gives $\varepsilon_{calc} = \{L + x - (R-x)\}/\text{total}$ as does the B spectrum.

Hence $\varepsilon_{calc} = \varepsilon_T + (2x/\text{total})$, and since the quantity x contains the non-planar events, ε_{calc} can be significantly different from the true asymmetry unless it is ensured that the spectra coincide with each other as closely as possible.

APPENDIX 4.3

Application of the Basel convention to obtain the correct sign of the polarization.

When neutrons are scattered from a target as indicated in the diagram, the left-right asymmetry as defined by the Basel convention is given by $\varepsilon = (R - L)/(R + L)$.

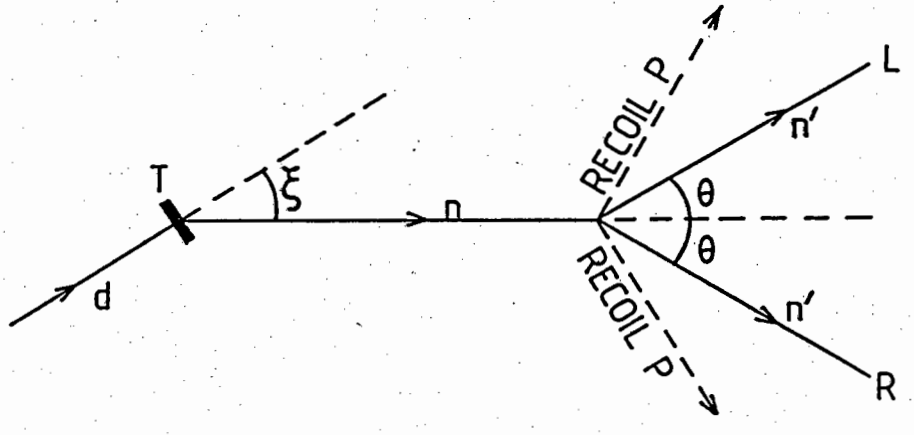

Hence, in terms of the proton recoils, the asymmetry is given by

$$\varepsilon = \frac{\text{no. protons to left - no. protons to right}}{\text{total counts}} \quad .$$

When the orientation of the anthracene crystal was as indicated, the events were stored in matrix A. Here the protons scattered to the left are closer to the c′-axis (low S) and hence to be consistent with the Basel convention, the asymmetry is given by

$$\varepsilon = (\ S_{low} \text{ counts} - S_{high} \text{ counts}\ )/\text{total counts} \quad .$$

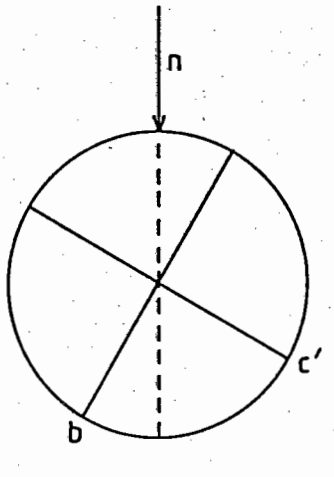

A orientation

When the crystal orientation was inverted as shown below, the events were stored in matrix B. Here the protons scattered to the left are closer to the b-axis (high S) and hence

ε = (S_{high} counts - S_{low} counts)/total counts .

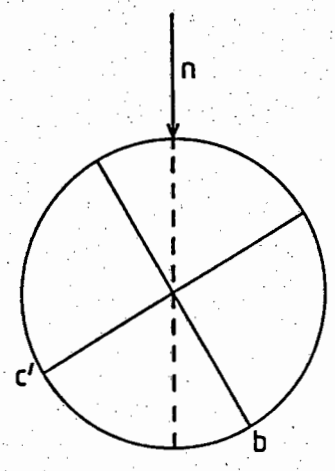

B orientation

APPENDIX 4.4

Edge normalisation factor

Assume the total counts in each of an A and B spectrum is N. The number of counts in the left edge and right edge windows is as indicated below.

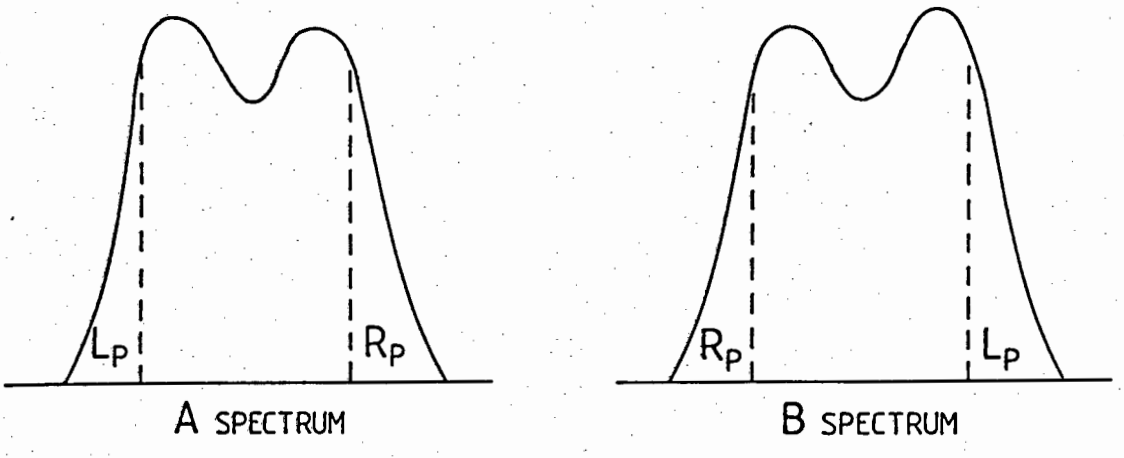

Now select corresponding channel numbers within the windows.

A spectrum: left channel count value = fL_P (i.e. a fraction of L_P)

right channel count value = gR_P (to account for a possible window width difference)

B spectrum: left channel count value = fR_P

right channel count value = gL_P

An edge normalisation factor K is determined for the left edge of the B spectrum such that

$K.fR_P = fL_P$ i.e. $K = L_P/R_P$ (ie. the ratio of the left and right planar counts.)

Then, using 1/K as the normalisation factor for the right edge gives

$(1/K)gL_P = (R_P/L_P)gL_P = gR_P$ as required.

It also follows that

$$\varepsilon_{planar} = (L_P-R_P)/(L_P+R_P) = (KR_P-R_P)/(KR_P+R_P) = (K-1)/(K+1).$$

Hence the determination of K should give an indication of what asymmetry value can be expected.

The effect of the escape peak

Assume an escape peak sits under the spectrum as shown

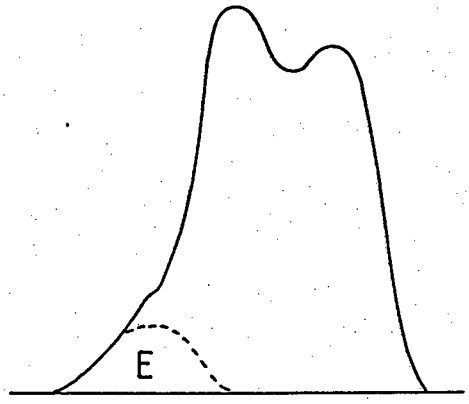

Then,

A spectrum: left channel count value = $fL_P + hE$

right channel count value = gR_P

B spectrum: left channel count value = $fR_P + hE$

right channel count value = gL_P

If K is determined as before,

$$K(fR_P + hE) = fL_P + hE \qquad \text{ie.} \qquad K = \frac{fL_P + hE}{fR_P + hE}$$

Hence, compensating for the right edge asymmetry gives

$$\frac{1}{K}.gL_P = \frac{fR_P + hE}{fL_P + hE}.gL_P \neq gR_P \quad \text{unless } E = 0 .$$

This shows that if the escape contribution is not properly accounted for, assuming 1/K as the factor for the right edge leads to an incorrect K value being determined. This in turn results in an inaccurate estimation of the corresponding shift correction.

APPENDIX 4.5

Asymmetry uncertainty estimate

To assess the statistical uncertainty of the asymmetry extracted from a single spectrum, it is necessary to use a formula based on the number of events acquired. The derivation is described below:

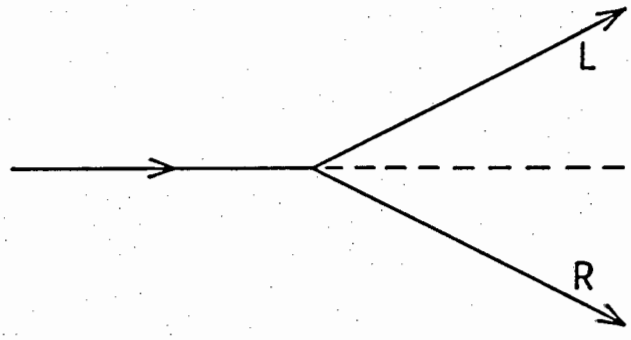

Each scattering event has only two possible outcomes, a proton scatter to the left or right of the incident beam direction. Each event is a Bernoulli trial in which each scatter to the right, say, can be defined as a success. From statistical theory, if X is the total number of successes in n repeated independent Bernoulli trials with probability p of success on a given trial, then X is called the binomial random variable.

Here $p = R / (L + R)$ and $q = 1 - p = L / (L + R)$.

For the binomial random variable, the mean μ and variance σ^2 are as follows:

$$\mu = np = (L + R).R / (L + R) = R$$

and $\sigma^2 = npq = (L + R).R/(L + R).L/(L + R) = RL / (L + R)$.

Therefore $\sigma = [RL/(L + R)]^{1/2}$ is the standard deviation at the 68% confidence level.

A typical left-right angle bin spectrum looks as follows:-

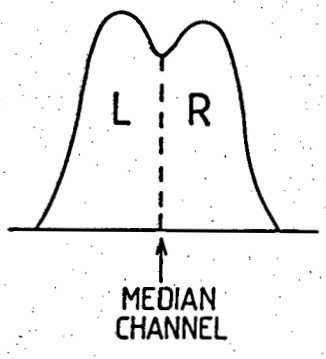

The measured asymmetry is given by $\varepsilon = (L - R) / N$ where $N=L+R$

Therefore $\varepsilon = 1/N \{L - (N - L)\} = 1/N (2L - N)$

Hence $\Delta\varepsilon = 2 \Delta L / N$ where $\Delta L = (LR/N)^{1/2}$

ie. $$\Delta\varepsilon = \frac{2(LR)^{1/2}}{(L + R)^{3/2}}$$

(ie. the same as for the conventional double scattering geometry).

APPENDIX 6.1

Results of the run using the polarimeter as an analyzer.

The crystal scintillation polarimeter can also be used in reverse as an analyzer to determine the polarization of a neutron beam. In this application n-p phase-shifts can be used to calculate the n-p polarization values at the beam energy being used. The polarization of the neutron beam is then given by $P=\varepsilon/P_{np}$, where ε is the measured asymmetry. To demonstrate the analyzer in operation, a run was carried out under slightly different conditions to that of the n-p polarization experiments. The $T(d,\vec{n})^4He$ reaction was again used and a deuteron energy of 5.6 MeV was selected. The target was anthracene 2. Again null ($\xi=0^o$ and E_d=5.0 MeV, giving 22.0 MeV neutrons) and polarization (for E_d=5.6 MeV, a reaction angle of $\xi=25^o$ was chosen, giving 22.0 MeV neutrons) data were collected. The results of the asymmetry measurements are given in table A6.1. The asymmetry values used in the following calculation are those to which a shift correction was applied.

Since $P_{inc} = \varepsilon(\theta)/P_{np}(\theta)$, the best least squares estimate for P_{inc} is given by $P_{inc} = (\Sigma_i\ w_i\varepsilon_i P_i)/(\Sigma_i\ w_i P_i^{\,2})$ where

ε_i represents each $\varepsilon_{corr}(\theta)$ value ,

P_i represents each $P_{np}(\theta)$ value, and

$w_i \propto 1/(\Delta e_i)^2$. $\Delta\varepsilon_i$ corresponds to the uncertainty in ε_i.

The $P_{np}(\theta)$ values used were given by the Paris potential predictions for n-p polarization at E_n=22.0 MeV. The values of P_i, ε_i and w_i are given in table A6.2.

The calculation gives $P_{inc} = 0.110 \pm 0.015$. A test of the goodness-of-fit gives a chi-square per degree of freedom of 1.0.

Table A6.1. Polarimeter used as an analyzer : asymmetry measurements.

θ_n		no shift correction	with shift correction
90°	ε_{null}	0.0134 ± 0.0011	0.0002 ± 0.0011
	ε_{pol}	0.0142 ± 0.0010	0.0051 ± 0.0010
	ε_{corr}	0.0008 ± 0.0010	0.0051 ± 0.0010
105°	ε_{null}	0.0117 ± 0.0013	0.0121 ± 0.0013
	ε_{pol}	0.0165 ± 0.0012	0.0161 ± 0.0012
	ε_{corr}	0.0048 ± 0.0012	0.0040 ± 0.0012
115°	ε_{null}	0.0099 ± 0.0014	0.0131 ± 0.0014
	ε_{pol}	0.0131 ± 0.0012	0.0165 ± 0.0012
	ε_{corr}	0.0032 ± 0.0012	0.0034 ± 0.0012
130°	ε_{null}	0.0098 ± 0.0012	0.0071 ± 0.0012
	ε_{pol}	0.0095 ± 0.0010	0.0110 ± 0.0010
	ε_{corr}	-0.0003 ± 0.0010	0.0039 ± 0.0010

Table A6.2. Values used in determining the polarization of the neutrons from $T(d,\vec{n})^4He$ at E_d=5.6 MeV and ξ=25°.

θ_n	P_i	ε_i	w_i
90°	0.0504	0.0051	1.00
105°	0.0392	0.0040	0.69
115°	0.0313	0.0034	0.69
130°	0.0204	0.0039	1.00

REFERENCES

AD78 J.M.Adams and G.White, Nucl. Instr. and Meth. 156 (1978) 459.

AL61 T.K.Alexander and F.S.Goulding, Nucl. Instr. and Meth. 13 (1961) 244.

AR77 R.A.Arndt,R.H.Hackman and L.D.Roper, Phys. Rev. C15 (1977) 1002.

AR83 R.A.Arndt,L.D.Roper,R.A.Bryan,R.B.Clark,B.J.VerWest and P.Signell, Phys. Rev. D28 (1983) 97.

BA83 M.D.Barker,D.Holslin,P.A.Quin and W.Haeberli, Proceedings of the Tenth International IUPAP Conference on Few Body Problems in Physics, Karlsruhe, 1983, vol. II, p.31.

BO76 G.E.Bohannon,Thomas Burt,and Peter Signell, Phys. Rev. C13 (1976) 1816.

BR74 F.D.Brooks and D.T.L.Jones, Nucl. Instr. and Meth. 121 (1974) 77 ; F.D.Brooks and D.T.L.Jones, Nucl. Instr. and Meth. 121 (1974) 69.

BR78 J.E. Brock,A.Chisholm,J.C.Duder and R.Garrett, Proc. 8th Int. Conf. on few body systems and nuclear forces, Graz 1978,Lecture Notes in Physics,vol. 82 p.252.

BR79 G.E. Brown and M.Rho, Phys. Lett. 82B (1979) 177; G.E. Brown,M.Rho and V.Vente, Phys. Letts. 84B (1979) 383 ; Phys. Rev. D22 (1980) 2838 ; Phys. Rev. D24 (1981) 216.

BR81 J.E.Brock,A.Chisholm,J.C.Duder,R.Garrett and J.L.Poletti, Nucl. Phys. A361 (1981) 368.

BR83 Gerald E.Brown and Mannque Rho, Physics Today,Feb. 1983, p.24.

BR86 Gerald E.Brown and Mannque Rho, Comments Nucl. Part. Phys. 15, no. 6 (1986) 245.

BU67 W.Busse,J.Christiansen,D.Hilscher,U.Morfeld,J.A.Scheer and W.U.Schroder, Nucl. Phys. A100 (1967) 490.

BU81 D.V.Bugg, Progress in particle and nuclear physics (ed. D.Wilkinson) 7 (1981) 47.

BU85 D.V.Bugg, Ann. Rev. Nucl. Part. Sci. 35 (1985) 295.

CH80 A.Chisholm,J.C.Duder,R.Garret and J.L.Poletti, Phys. Rev. C21 (1980) 1653.

CO73 W.N.Cottingham,M.Lacombe,B.Loiseau,J.M.Richard and R.Vinh Mau, Phys. Rev. D8 (1973) 800.

CO80 J.Cote,M.Lacombe,B.Loiseau,P.Pires,R.de Tourreil and R. Vinh Mau, 5th Int. Symp. on Polarization Phenomena in Nuclear Physics, Santa Fe 1980, p.114.

DA52 R.H.Dalitz, Proc. Phys. Soc. (London), A65 (1952) 175.

DR66 N.R.Draper and H.Smith, Applied Regression Analysis, John Wiley & Sons, Inc., 1966.

ER83 T.E.O. Ericson and G.A.Miller, Phys. Letts. 132B (1983) 32.

FR73 H.Fritzsch,M.Gell-Mann and H.Leutwyler, Phys. Lett. B47 (1973) 365.

GA63 J.L.Gammel, Fast neutron physics, part 2, ed. J.B.Marion and J.L.Fowler (Interscience, New York, 1963) p.2185.

GE64 M.Gell-Mann, Phys. Lett. 8 (1964) 214.

GI80 W.M.Gibson, The Physics of Nuclear Reactions, 2nd. edition, Pergamon Press Ltd., 1980.

GL74 D.W.Glasgow,D.E.Velkley,J.D.Brandenberger and M.T.McEllistrem, Nucl. Instr. and Meth. 114 (1974) 535.

HA62 T.Hamada and I.D.Johnston, Nucl. Phys., 34 (1962) 382.

HA77 W.Haeberli, AIP Conference Proceedings on Nucleon- Nucleon Interactions,Vancouver,41 (1977) 1.

IS83 Nathan Isgur and Gabriel Karl, Physics Today, Nov. 1983, p.36.

JO72 D.T.L.Jones, Ph.D. Thesis, University of Cape Town (1972) unpublished.

JO74 D.T.L.Jones and F.D.Brooks, Nucl. Phys. A222 (1974) 79.

JO75 For a review of bag models see, for example, K.Johnson, Acta Physica Polonica B6 (1975) 865.

LA66 T.Lauritsen and F.Ajzenberg-Selove, Nucl. Phys. 78 (1966) 1.

LA75 M.Lacombe,B.Loiseau,J.M.Richard,R.Vinh Mau,P.Pires and R. de Tourreil, Phys. Rev. D12 (1975) 1495.

LA80 M.Lacombe,B.Loiseau,J.M.Richard,R.Vinh Mau,J.Cote, P.Pires and R.de Tourreil, Phys. Rev. C21 (1980) 861.

LINK LINK Model 5010 Pulse Shape Discriminator from LINK SYSTEMS Halifax Rd.,High Wycombe,Bucks,England,HP123SE.

MA60 M.H.MacGregor,M.J.Moravcsik and H.P.Stapp, Ann. Rev. Nucl. Sci. 10 (1960) 291.

MA69 M.H.MacGregor,R.A.Arndt and R.M.Wright, Phys. Rev. 182 (1969) 1714.

MA69b M.H.MacGregor, Physics Today, Dec. 1969, p.21.

MI81 G.A.Miller,S.Theberge and A.W.Thomas, Comments Nucl. Part. Phys. A10 (1981) 101 ; Phys Rev. D22 (1980)2838; Phys. Rev. D24 (1981) 216.

MI86 H.G.Miller, private communication.

MO72 M.J.Moravcsik, Rep. Prog. Phys. 35 (1972) 587.

MO74 C.L.Morris,T.K.O'Malley,J.W.May,Jr.,and S.T.Thornton, Phys. Rev. C9 (1974) 924.

MU71 G.S.Mutchler and J.E.Simmons, Phys. Rev. C4 (1971) 67.

MU71b G.S.Mutchler,W.B.Broste and J.E.Simmons, Phys. Rev. C3 (1971) 1031.

NA66 Y.Nambu, Preludes in Theoretical Physics, A.de Sahlit, H.Feschbach,L.van Hove,eds.,North-Holland,Amsterdam (1966) 133.

NO77 H.Pierre Noyes, AIP Conference Proceedings on Nucleon-Nucleon Interactions,Vancouver, 41 (1977) 558.

PE61 R.B.Perkins and J.E.Simmons, Phys. Rev. 124 (1961) 1153.

PH60 R.J.N.Phjilips, Harwell Research Rept., AERE-R3141 (1960).

RA81 F.N.Rad,R.G.Graves,D.P.Saylor,M.L.Evans,E.P.Chamberlin, J.W.Watson and L.C.NorthCliffe, Nucl. Instr. and Meth. 190 (1981) 459.

RE68 R.V.Reid,Jr., Ann. Phys., 50 (1968) 411.

RO64 M.L.Roush,M.A.Wilson and W.F.Hornyak, Nucl. Instr. and Meth. 31 (1964) 112.

SA64 A.Savitzky and M.J.E.Goloy, Analytical Chemistry vol. 36, no. 8 (July 1964) 1627.

SE68 R.E.Seamon,K.A.Friedman,G.Breit,R.D.Haracz,J.M.Holt and A.Prakash, Phys. Rev. 165 (1968) 1579.

SI69 P.Signell, Advances in Nuclear Physics (ed. M.Baranger and E.Vogt) 2 (1969) 223.

SM72 J.R.Smith and S.T.Thornton, Nucl. Phys. A187 (1972) 433.

SP73 D.W.L.Sprung and R.de Tourreil, Nucl. Phys. A201 (1973) 193.

SR86 J.Sromicki,D.Holslin and W.Haeberli, Proc. Sixth Int. Symp. Polar. Phenom. in Nucl. Phys., Osaka, 1985 J.Phys. Soc. Jpn. 55 (1986) Suppl. p. 812-813.

ST75 M.Steinbock,F.D.Brooks and I.J.van Heerden, Proc. Fourth Int. Symp. on polarization phenomena in nuclear reactions,

Zurich 1975, p.475.

TO80 W.Tornow,P.W.Lisowski,R.C.Byrd and R.L.Walter, Nucl. Phys. A340 (1980) 34.

TS62 K.Tsukada and S.Kikuchi, Nucl. Instr. and Meth. 17 (1962) 280.

VI72 R.Vinh Mau,J.M.Richard,B.Loiseau,M.Lacombe and W.N. Cottingham, Phys. Lett. 44B (1972) 1.

VI77 R.Vinh Mau, AIP Conference Proceedings on Nucleon- Nucleon Interactions, Vancouver, 41 (1977) 140.

WA84 M.Wakamatsu,R.Yamamoto and Y.Yamauchi, Phys. Lett. 146B (1984) 148.

WI74 K.G.Wilson, Phys. Rev. D10 (1974) 2445.

WI84 J.Wilczynski,J.Hansmeyer,F.P.Brady,P.Doll,W.Heeringa, J.C.Hiebert,H.O.Klages and P.Plischke, Nucl. Phys. A425 (1984) 458.

WO52 L.Wolfenstein and J.Ashkin, Phys. Rev. 85 (1952) 947.

WO54 L.Wolfenstein, Ann. Rev. Nucl. Sci. 6 (1956) 43.

YA35 H.Yukawa, Proc. Phys. Math. Soc., Japan, 17 (1935) 48.

YA62 Yale 1962 : K.E.Lassila,M.H.Hull,M.Ruppel,F.A.McDonald and G.Breit, Phys. Rev. 126 (1962) 881.

ZA80 For a review see V.Zacharov in High Energy Physics - 1980,L.Durand,L.G.Pondrom,eds.,AIP Conf. Proc. 68, Am. Inst. Phys., New York, p.1234.

ZW64 G.Zweig, CERN preprint TH412 (1964) unpublished.